Numerical Modeling of Narrow-linewidth Quantum Dot Lasers

Marko Bjelica

kassel university press

Marko Bjelica

Numerical Modeling of Narrow-linewidth Quantum Dot Lasers

kassel
university
press

This work has been accepted by the Faculty of Electrical Engineering / Computer Science of the University of Kassel as a thesis for acquiring the academic degree of Doktor der Ingenieurwissenschaften (Dr.-Ing.).

Supervisors: Prof. Bernd Witzigmann
Prof. Johann Peter Reithmaier
Prof. Axel Bangert
Prof. Peter Lehmann

Defense day: 16th January 2017

Bibliographic information published by Deutsche Nationalbibliothek
The Deutsche Nationalbibliothek lists this publication in the Deutsche Nationalbibliografie; detailed bibliographic data is available in the Internet at http://dnb.dnb.de.

Zugl.: Kassel, Univ., Diss. 2017
ISBN 978-3-7376-0284-6 (print)
ISBN 978-3-7376-0285-3 (e-book)
DOI: http://dx.medra.org/10.19211/KUP9783737602853
URN: http://nbn-resolving.de/urn:nbn:de:0002-402859

www.upress.uni-kassel.de

Printed in Germany

Numerical Modeling of Narrow-linewidth Quantum Dot Lasers

Marko V. Bjelica

Computational Electronics and Photonics Group
Fachbereich 16 Elektrotechnik/Informatik, Universität Kassel
Wilhelmshöher Allee 71 - 73, D-34121 Kassel

Doctoral thesis

Abstract

In modern fiber-optic communications a narrow spectral linewidth represents an important laser specification as it leads to the reduction of signal dispersion and allows for high bit rate and long haul optical communications. Being a statistical value, reliable measurement or calculation of spectral linewidth is not a straightforward problem. The thesis presented here deals with dynamic modeling of edge-emitting semiconductor laser diodes, while investigating the physics governing the spectral linewidth behavior.

To investigate this problem a laser simulation software, that will be referred to as *QD-wave*, was developed as a part of the thesis work. The software is designed mainly to address this problem for the case of quantum dot edge-emitting semiconductor lasers. The lasers based on quantum dot active material are known for many desirable properties, e.g. temperature insensitive threshold, high modulation bandwidth or low linewidth enhancement factor. This makes them a potential solution for the future high bit rate fiber-optic communications.

The laser modeling relies on time domain multi-section traveling wave method, while the noise sources are implemented in the scope of Langevin dynamics. The laser model was developed with an aim to include all the relevant Gaussian and colored noise sources, as well as the physical effects that govern the spectral linewidth behavior. To get a better insight into the importance of different effects and validity of simulation models, the simulation results are compared with spectral linewidth measurements of the designed quantum dot based photonic integrated circuits.

Numerical Modeling of Narrow-linewidth Quantum Dot Lasers

Marko V. Bjelica

Computational Electronics and Photonics Group
Fachbereich 16 Elektrotechnik/Informatik, Universität Kassel
Wilhelmshöher Allee 71 - 73, D-34121 Kassel

Doktorarbeit

Zusammenfassung

In heutigen photonischen Netzen ist die Linienbreite ein wichtiger Spezifikationsfaktor für Laserdioden, weil die schmale Linienbreite direkt zu geringerer Dispersion führt und dadurch höhere Bitraten und langstreckige Kommunikation ermöglicht. Da die Linienbreite ein statistischer Wert ist, ist die zuverlässige Messung oder Ausrechnung nicht immer leicht realisierbar. Die hier vorgelegte Dissertation befasst sich mit der dynamischen Modellierung des kantenemittierenden Halbleiterlasers unter Berücksichtigung der Effekte, die die Linienbreite beeinflussen.

Um das beschriebene Problem zu untersuchen, wurde ein Simulator für Laserdioden entwickelt, den wir weiter im Text als *QD-wave* bezeichnen werden. Die Software ist hauptsächlich geplant um dieses Problem für den Fall von kantenemittierenden Quantenpunktlaser anzugehen. Quantenpunktlaser sind bekannt für mehrere wünschenswerten Spezifikationsfaktoren, wie z.B. temperaturstabile Schwelle, gute Modulationsbandbreite oder niedriger Henry-Faktor, der die Ausdehnung der Linienbreite bestimmt. Aus diesem Grund sind Quantenpunktlaser potenziell eine optimale Lösung für zukünftige photonische Netze mit hohen Bitraten.

Die Modellierung des Lasers beruht auf der Methode der laufenden Welle, die im Zeitbereich implementiert ist, wobei die Rauschquellen im Rahmen der Langevin-Dynamik beschrieben sind. Das Laser-Modell wurde mit dem Ziel entwickelt alle relevante Rauschquellen zu berücksichtigen, wie auch die physischen Effekte die die Linienbreite beeinflussen. Um einen besseren Einblick in die Bedeutung

verschiedener Effekte und in die Gültigkeit des entwickelten Simulationsmodells zu gewinnen, wurden die Simulationsergebnisse auch mit Messungen der Linienbreite von realisierten quantenpunktbasierenden photonischen Komponenten verglichen.

Acknowledgments

I would like to thank Prof. Witzigmann for giving me the opportunity to work on this interesting topic and for his support throughout my stay with the Computational Electronics and Photonics Group at the University of Kassel. I am also especially thankful to the members of the department for valuable discussions and companionship: F. Römer, K. Mayer, A. Shedbalkar, K. Frank, Z. Andreev, S. Yu, U. Akcakoca, I. Dahhan, G. Ballier and M. Deppner. During the work on my thesis I had the opportunity to work together with undergraduate students, R. Tsega and Y. Shang, to whom I am grateful for their cooperation while working together on interesting and inspiring scientific problems.

Special thanks goes to Prof. Reithmeier and his whole Technological Physics group at the Institute of Nanostructure Technologies and Analytics for providing the necessary measurements for benchmarking of the developed numerical laser model. Without the help of our technical partners some milestones would simply not be possible to achieve. As a result of this close cooperation of theory and practice, we have managed to advance different aspects of photonic device design and modeling.

I am also grateful to kind administrative staff, A. Bernhardt and R. Brylla, that were always helpful with the administrative matters. The last but not least, I would like to thank for the financial support by the BMBF within the SASER program that has enabled the majority of the work presented here.

Contents

Chapter 1

Introduction

1.1 From Maser to Semiconductor Laser

Four decades after the theoretical study of stimulated emission by Albert Einstein [1], the principle of stimulated emission was first employed in a device emitting stimulated electromagnetic radiation at microwave frequencies [2]. The maser [1] device, developed at Columbia University in 1953 by Charles Townes, James Gordon and Herbert Zeiger, was based on stimulated emission by the excited ammonia molecules. The work was later extended by Charles Townes and Arthur Schawlow, this led to first design principles of what was then called an optical maser or in principle a laser [2] device that operated at optical frequencies.

At the same time Nikolay Basov and Aleksandr Prokhorov at Lebedev Institute of Physics, described the principles governing the operation of the maser. Later in 1964 they have shared the Nobel Prize in Physics together with Charles Townes for their research on stimulated emission. However, the technology still needed time to develop. The first semiconductor based laser have suffered from high threshold currents which greatly limited the room temperature operation. The major breakthrough came with the proposition of the heterostructure principle by Herbert Krömer in 1963 [3], which reduced the threshold current by the improved carrier confinement. Not long after, due

[1] MASER - Microwave Amplification by Stimulated Emission of Radiation

[2] LASER - Light Amplification by Stimulated Emission of Radiation

to the temporal and spatial coherence of the emitted light, the lasers have found many practical applications, ranging from laser surgery in medicine, measurement of distance and speed, coherent optical communications to material processing in industry.

The importance of lasers in fiber-optic communications is more than apparent today, and as they are the main concern of this thesis, few points related to their application in fiber-optics should be stressed here. Due to the problems of signal dispersion in optical fibers, for long-haul communications the temporal coherence and high intensity of laser light represent an important specification. Namely, the high spectral purity of the transmitter would minimize the need for signal reconstruction along the communication line, which would then minimize the costs by reducing the number of signal repeaters. There are however numerous techniques that indirectly address the dispersion problem, but with the trend of increasing bit rate in fiber-optic communications, the need for higher temporal coherence, i.e. narrow spectral linewidth of signal sources cannot be avoided.

1.2 Laser Linewidth in Fiber-Optic Communications

Since the development of crucial technologies for high bit rate fiber-optic communications, the internet has seen a great transformation, with fiber-optics breaking all the bit rate barriers of the standard copper cable based networks. However, with growing number of developing digital services the demand for ever higher internet bit rates does not seem to saturate with modern state of fiber-optics. To accommodate this trend the fiber-optic communications will have to continue to evolve.

One of the commonly used modulation techniques in fiber-optic communications is the on-off keying or OOK for short, the simplest amplitude modulation. Even though attractive for its simplicity and low-cost transceiver realization, it still greatly limits the bit rate to 10 Gb/s per carrier wavelength. To fully utilize the fiber-optic infrastructure with minimum costs of restructuring, higher-order signal modulations, Fig. (1.1), need to be integrated with existing dense wavelength-division multiplexing (DWDM) systems.

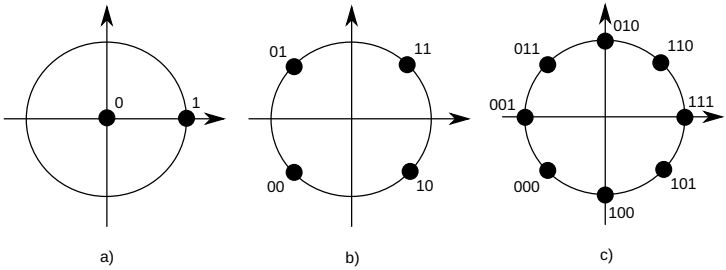

Figure 1.1: Constellation diagrams of typical digital modulation schemes: a) on-off keying(OOK), b) quadrature phase-shift keying(QPSK), c) 8-phase-shift keying(8-PSK)

However, the high-order modulation schemes that are typically employed in wireless and copper cable based networks impose extremely high spectral purity for the signal sources in case of the fiber-optic communications [4]. For this reason there is still ongoing research on reduction of spectral linewidth in semiconductor lasers. Some promising results of quantum well based laser designs can be found already [5,6], but due to complexity of operating conditions of the semiconductor laser, it is still an open question what would be the optimal design with respect to yield, quality or the complexity of the production processes involved.

1.3 Problem of Spectral Linewidth

The laser diodes are well known for their high spectral purity, i.e. high temporal coherence of emitted light. However, the linewidth of a laser diode depends strongly on the noise sources affecting the device properties, by modifying the phase and intensity of the lasing light. The two basic noise sources are spontaneous emission noise and carrier noise. The first equation applied for the linewidth estimation of lasers sources was an adapted version of the spectral linewidth equation used in experiments with masers, known as Schawlow-Townes linewidth equation. Where the equation for spontaneous emission below lasing threshold reads

$$\Delta\nu_{spon} = \frac{\Gamma R_{sp}^{'}}{2\pi N_p}, \tag{1.1}$$

and above threshold for stimulated emission (modified Schawlow-Townes formula):

$$\Delta\nu_{stim} = \frac{\Gamma R_{sp}^{'}}{4\pi N_p}, \tag{1.2}$$

here the additional 1/2 factor for the equation above threshold comes from the nonlinear coupling of the carrier and field rate equations, suppressing one of the two quadrature components of the noise [7]. Where Γ is the confinement factor of the active region, $R_{sp}^{'}$, the spontaneous emission coupled to the lasing mode and N_p, the photon density. Even though accurate enough for the spectral linewidth below threshold, Schawlow-Townes linewidth equation considers only the effect of spontaneous emission on the spectral linewidth of semiconductor lasers and often underestimates the linewidth above threshold.

Major improvement of the spectral linewidth theory of semiconductor lasers above threshold came with the seminal work of Charles Henry in 1982, where he introduced the linewidth enhancement factor [8], often denoted as α-factor. The α-factor relates the change in real part of the refractive index, $\Delta n^{'}$, to change in imaginary part of the refractive index $\Delta n^{''}$.

$$\alpha = \frac{\Delta n^{'}}{\Delta n^{''}} \tag{1.3}$$

The real and imaginary part of the refractive index are linked by Kramers-Kronig relation, meaning that the change in imaginary part will also cause the change in the real part of the refractive index and vice versa. The change in carrier density changes the imaginary part, $n^{''}$, which changes via Kramers-Kronig relation the real part of the refractive index. As this is happening on short time intervals the phase of the field is also altered which results in additional linewidth broadening that cannot be neglected. The spectral linewidth of semiconductor lasers above threshold was found by Charles Henry to depend quadratically on the linewidth enhancement factor:

$$\Delta\nu_{stim} = \frac{\Gamma R_{sp}^{'}}{4\pi N_p}(1+\alpha^2). \tag{1.4}$$

The Eq. (1.4) gives fairly accurate estimation for most of the applications. However, at higher injection currents and higher output powers where spectral linewidth reaches its minimum that is highly needed in fiber-optic communications the situation further complicates with numerous other phenomena emerging. The effect of carrier noise on spectral linewidth becomes more relevant at high output powers, its white noise component but also colored noise component that is still not fully understood. Linewidth enhancement factor cannot be considered constant but is rather both intensity and carrier density dependent, or formation of the carrier grating pattern with high field intensity are some of the problems arising in these extreme cases.

1.4 TCAD in Semiconductor Industry

Looking historically, before the broader adoption of the computers and computer aided design (CAD) tools, the companies in the semiconductor industry were commonly running the whole production line within the company. The reason for this lies mainly in the design procedure of the semiconductor devices. Prior to 1980, the estimation of the device performance was mainly limited to analytical models, meaning that the availability of experimental data of the early prototypes was crucial for optimization of the design for the current needs of the market. Such an approach generally requires substantial initial investments on the side of the companies, due to the costly equipment which was often underutilized as it was used only for own needs.

With the increase of computational power and the development of comprehensive multi-physics technology aided design (TCAD) software, the approach to device design has changed drastically. More accurate two- and three-dimensional models are today able to replace much of the tedious experimental work while driving down the production costs, by reducing the number of iteration steps necessary to reach the performance requirements. Aside from the accurate modeling of the semiconductor devices the TCAD models, like the one presented in this thesis, offer deeper insight into the interplay of numerous effects

which can be particularly advantageous in understanding the operation of novel designs. Finally, the benefits of implementing the TCAD tools in production process did not only benefit the already established companies but also promoted a healthy competition in the semiconductor industry, by enabling the emergence of many fabless companies that had novel ideas but limited resources to finance the fabrication process.

1.5 Overview of the Thesis

Chapter 1: Introduction. Historical background of semiconductor lasers is summarized here, and the importance of narrow spectral linewidth in fiber-optic communications is explained. Finally, the motivation for using the numerical modeling is discussed, together with its general effect on semiconductor industry.

Chapter 2: Elementary Laser Theory. The theory of lasers is discussed by following its historical evolution. First, the two seminal papers are reviewed in order to summarize the classical and semi-classical theory framework, with the classical theory relating to free-electron lasers and semi-classical to a more broader class of lasers driven by the polarization of the active medium. The material gain as one of the crucial characterization parameters of semiconductor lasers is then discussed in relation to quantization of the laser's active material, while showing how the quantum effects can contribute to the overall performance of the laser.

Chapter 3: Modeling of Quantum Dot Active Material. The quantum dot gain model is fully described, with examples of extracted parameters as they are implemented in the dynamic laser simulator *QD-wave*, e.g. modal gain, refractive index change, linewidth enhancement factor etc. The adequate input parameters are also given, with regard to reported quantum dot gain measurements.

Chapter 4: Dynamic Modeling of Semiconductor Lasers. The core of the developed time-domain laser simulator *QD-wave*, based on the traveling wave method, is presented together with all the included

effects related to the noise and laser linewidth. The model is essentially 1+1 dimensional, i.e. considers only longitudinal and temporal variation of the model variables. The transversal problem is treated separately, where the inclusion of transversal confinement factors and the coupling coefficient of the Bragg grating is described. Finally, following the limitations of the traveling wave method in terms of the spectral resolution, the necessary postprocessing module for linewidth extraction is described with discussion of possible applications.

Chapter 5: Simulation Examples and Benchmarks. In this chapter we deal with the practical applications of the *QD-wave* simulator, for the purpose of validating the laser model and investigating the potential of considered designs. We start with a basic distributed feedback (DFB) quantum dot laser, where we study the importance of different effects related to the linewidth while seeking to optimize the design for narrow spectral linewidth. The performance of the DFB lasers is then examined in an integrated device, a tunable laser array based on the Y-couplers. Finally, a further reduction of the spectral linewidth is investigated by optimization of the cavity design.

Chapter 6: Conclusions and Outlook. Following the summary of major results, we give final conclusions and consider possible future model improvements that could lead to an increased accuracy and better understanding of the experimental results.

Chapter 2

Elementary Laser Theory

Since the introduction of the first maser and laser devices [2,9], the laser theory has evolved in parallel with the progress of the technology and design aspects. Due to the wave-particle duality the interpretation of laser operation can be somewhat confusing. Historically both quantum and classical theory have been employed in the study of stimulated emission. In this chapter we briefly summarize the elementary laser theory by reviewing two seminal papers [10, 11], showing first how the classical theory is sufficient for the explanation of amplification within a free-electron laser. The classical theory we then extend to the more modern semi-classical laser model, that is widely accepted today in the study of semiconductor lasers, thus including the quantum aspects of the active medium.

2.1 Classical Free-electron Laser Theory

In the 1960s, during the earlier history of laser theory the wave-particle duality of photons was already well established [1]. The early Einstein's work on stimulated emission in the framework of quantum mechanics may have acted as a stimulus for the similar treatment of the laser operation. The early publications studying the principles of free-electron laser operation [12, 13], rely heavily on the quantum mechanical ap-

proach. This is not particularly surprising as we are dealing with electrons and photons, which are indeed quantum mechanical particles. Nevertheless, the principle of amplification in a free-electron laser is not intrinsically quantum mechanical. To show this we can follow the work in [10], and see how the nonlinear interaction of the electromagnetic field and the active medium can lead to gain in a laser.

To this end, we will use purely classical theory, i.e. Maxwell's equations for the field and Newton's equations of motion for the active medium, defined in the space-time continuum. More precisely the dynamics of the electron distribution, $f(\boldsymbol{x}, \boldsymbol{P}, t)$, is described by the collisionless relativistic Boltzmann equation:

$$\frac{df}{dt} = \frac{\partial f}{\partial t} + \dot{x}_i \frac{\partial f}{\partial x_i} + \dot{\boldsymbol{P}}_i \frac{\partial f}{\partial \boldsymbol{P}_i} = 0, \tag{2.1}$$

while the field is coupled with electron distribution via the wave equation through the transverse current $\boldsymbol{J}_t$:

$$\nabla^2 \boldsymbol{A} - \frac{1}{c^2} \frac{\partial^2 \boldsymbol{A}}{\partial t^2} = -\mu_0 \boldsymbol{J}_t, \tag{2.2}$$

where $\boldsymbol{P}$ is the canonical momentum, $\boldsymbol{x}$ the position vector, and $\boldsymbol{A}$ the vector potential. The time dependent number of electrons $N(t)$, and transverse current $\boldsymbol{J}_t(\boldsymbol{x}, t)$, are defined as:

$$N(t) = \int d^3x \int d^3\boldsymbol{P} \cdot f(\boldsymbol{x}, \boldsymbol{P}, t), \tag{2.3}$$

$$\boldsymbol{J}_t(\boldsymbol{x}, t) = q \int d^3\boldsymbol{P} \cdot \boldsymbol{v}_t f(\boldsymbol{x}, \boldsymbol{P}, t). \tag{2.4}$$

To make the problem defined by the Eqs. (2.1,2.2) more analytically useful, one can greatly simplify it by adopting some reasonable approximations. The electromagnetic field can be assumed as transverse $\boldsymbol{A}(z, t)$, varying only longitudinally along z-axis, and with time t. Similarly, considering that the electrons are injected along the z-axis at a relativistic speed, the transverse velocity being much smaller can be also neglected, and thus $p_t = 0$. The approximations ultimately allow us to reduce the problem to a one-dimensional. First, we can consider how the relativistic electron Hamiltonian:

$$\mathcal{H} = \gamma mc^2 = c\sqrt{(\boldsymbol{P}_t - q\boldsymbol{A_t})^2 + {p_z}^2 + m^2c^2}, \tag{2.5}$$

can be simplified. By neglecting the transverse momentum, the Hamiltonian reduces to:

$$\mathcal{H} = \gamma mc^2 \approx mc^2\sqrt{1 + (q\boldsymbol{A}_t/mc)^2 + (p_z/mc)^2}, \tag{2.6}$$

where p_z is a kinetic momentum along z-axis, $p_z = \gamma m v_z$. For the electric fields smaller than 10^{12} V/m [10], the Hamiltonian further simplifies to:

$$\mathcal{H} = \gamma mc^2 \approx mc^2\sqrt{1 + (p_z/mc)^2}. \tag{2.7}$$

Assuming a perfect cylindrical geometry of radius a, for the injected electron beam, the electron distribution can be written as:

$$f(\boldsymbol{x}, \boldsymbol{P}, t) = [u(r) - u(r-a)]\delta_{2D}(\boldsymbol{P}_t)h(z, p_z, t), \tag{2.8}$$

where $u(\boldsymbol{x})$ is a Heaviside function. The Eqs. (2.1,2.2) can finally be reduced to one-dimensional by substituting the results from Eqs. (2.8,2.7):

$$\frac{\partial h}{\partial t} + \frac{p_z}{m\gamma}\frac{\partial h}{\partial z} = \frac{q^2}{m\gamma}\frac{\partial(\frac{1}{2}{\boldsymbol{A}_t}^2)}{\partial z}\frac{\partial h}{\partial p_z}, \tag{2.9}$$

$$\left(\frac{\partial^2}{\partial z^2} - \frac{1}{c^2}\frac{\partial^2}{\partial t^2}\right)\boldsymbol{A}_t = \frac{q^2\mathcal{F}}{mc\epsilon_0}\boldsymbol{A}_t\int_{-\infty}^{\infty} dp_z \cdot \frac{h(z, p_z, t)}{\gamma}, \tag{2.10}$$

where $\mathcal{F} = a^2/b^2$, and b is the radius of the cavity. The component $h(z, p_z, t)$ in Eq. (2.8), can be expanded in a perturbation series [10,11]:

$$h = h^{(0)} + h^{(1)} + h^{(2)} + ..., \tag{2.11}$$

and by keeping only the first two terms, $h^{(0)}$ and $h^{(1)}$, we get a small-signal model. By assuming the circularly polarized field $\boldsymbol{A}_t$:

$$\boldsymbol{A}_t = \frac{\hat{\boldsymbol{e}}_x - \hat{\boldsymbol{e}}_y}{\sqrt{2}}\{A_i \exp[-i(\omega_i t + k_i z)] + A_s \exp[-i(\omega_s t + k_s z)]\} + c.c., \tag{2.12}$$

consisting of incident and back-scattered field components of amplitudes, A_i and A_s, respectively. The first two terms, $h^{(0)}$ and $h^{(1)}(z, p_z, t)$, in Eq. (2.11), of the small-signal model can be then expressed as:

$$h^{(0)} = n_e F(p_z), \tag{2.13}$$

where n_e is the electron density and $F(p_z)$, the initial electron momentum distribution, and

$$h^{(1)}(z, p_z, t) = \frac{-q^2 K n_e {A_i}^* A_s}{p_z} \frac{q^{-i\mu z} - 1}{\mu} \exp\left[-i\Delta\omega(t - \frac{z}{v_z})\right] + c.c., \tag{2.14}$$

where $K = k_s + k_i$ and $\Delta\omega = \omega_s - \omega_i$. It can be noticed that the $h^{(1)}(z, p_z, t)$ component describes the carrier density fluctuations along the electron beam which are responsible for the scattering. Finally, by substituting the $h^{(0)}$ and $h^{(1)}(z, p_z, t)$, in the Maxwell's equation and integrating along the cavity of length L, one can obtain the small-signal gain:

$$\alpha(s^{-1}) = \frac{-4\pi {r_0}^2 \mathcal{F} n_e m K L}{{k_i}^2 k_s} I_i \int dp_z \cdot F(p_z) \frac{d}{dp_z} \left[\frac{1}{\gamma p_z}\left(\frac{sin(\frac{1}{2}\mu L)}{\frac{1}{2}\mu L}\right)^2\right] \tag{2.15}$$

The classical theory as presented here is in most cases sufficient to describe the operation of a free-electron laser. In contrast to semiconductor lasers, the free-electron lasers are driven by the incoherent synchrotron radiation produced by the transverse acceleration of the electrons in the relativistic electron beam. Only when the radiation is strong enough the transverse electric field of the radiation can modulate the electron beam, creating the electron microbunches along the laser axis where electrons are able to radiate photons that are in phase.

The design of a free-electron laser is often larger in scale, but due to its wide range of operating frequency it is still present in many fields. The tuning range covers the spectra ranging from microwave to X-ray radiation, while applications can be found in medical and military industries.

2.2 Semi-classical Laser Theory

To get a more general theoretical framework describing a broader set of laser devices one still needs to complement the classical electromagnetics with quantum mechanical theory. The first version of such a self-consistent semi-classical theory came with the work W. E. Lamb [11], which relies on classical electromagnetic theory to describe the resonating field and the quantum theory to model the polarization of the active medium. The electromagnetic field acts on the active medium by polarizing it while the polarization acts as a source of the field within the context of Maxwell's equations.

$$\nabla \times \boldsymbol{E} = -\frac{\partial \boldsymbol{B}}{\partial t} \tag{2.16}$$

$$\nabla \times \boldsymbol{B} = \mu_0 \left(\boldsymbol{J}_f + \frac{\partial \boldsymbol{D}}{\partial t} \right) \tag{2.17}$$

$$\nabla \cdot \boldsymbol{D} = \rho_f \tag{2.18}$$

$$\nabla \cdot \boldsymbol{B} = 0 \tag{2.19}$$

The optical field is defined by the four Maxwell's equations, Eqs. (2.16 - 2.19), i.e. Faraday's law Eq. (2.16), Ampere's law Eq. (2.17), and Gauss' laws for electric and magnetic field, Eq. (2.18) and Eq. (2.19), respectively.

$$\boldsymbol{D} = \epsilon_0 \boldsymbol{E} + \boldsymbol{P}, \quad \boldsymbol{B} = \mu_0 \boldsymbol{H}, \quad \boldsymbol{J}_f = \sigma \boldsymbol{E} \tag{2.20}$$

Using the relations for the vector fields Eq. (2.20), one can derive the general wave equation, which governs the resonating field:

$$\nabla \times (\nabla \times \boldsymbol{E}) + \mu_0 \sigma \frac{\partial \boldsymbol{E}}{\partial t} + \mu_0 \epsilon_0 \frac{\partial^2 \boldsymbol{E}}{\partial^2 t} = -\mu_0 \frac{\partial^2 \boldsymbol{P}}{\partial^2 t}. \tag{2.21}$$

The early theory in [11], assumes that an array of excited atoms can be well approximated by describing the electric state of an active medium by a macroscopic polarization $\boldsymbol{P}(\boldsymbol{r}, t)$. As a consequence as shown in [11], by knowing the polarization of the active medium one can

derive the amplitudes, frequencies and phases of the emitted radiation. The theory treats the active medium as a simple system with two excited levels, which partially enables the analytical extraction of the aforementioned radiation properties. Nevertheless, by using more modern numerical models the semi-classical theory can be also adapted to semiconductor lasers and a wider range of active media [14], including the quantization effects, by proper modeling of the polarization term, $\boldsymbol{P}(\boldsymbol{r},t)$:

$$\boldsymbol{P}(\boldsymbol{r},t) = \epsilon_0 \int_{-\infty}^{+\infty} d\tau \cdot \chi_e(\boldsymbol{r},t,\tau)\boldsymbol{E}(\boldsymbol{r},t-\tau). \tag{2.22}$$

The material polarization is defined in general as a convolution of the electric field and a time dependent susceptibility $\chi_e(\boldsymbol{r},t)$, Eq. (2.22). As the material does not react instantaneously to an applied electric field $\boldsymbol{E}(\boldsymbol{r},t)$.

$$\boldsymbol{P}(\boldsymbol{r},\omega) = \epsilon_0 \chi_e(\boldsymbol{r},\omega)\boldsymbol{E}(\boldsymbol{r},\omega) \tag{2.23}$$

In practice it is often more informative to express the polarization in the frequency domain, Eq. (2.23), due to the convolution the expression in time domain, Eq. (2.22), translates to a simple product. In frequency domain one can often easily recognize the quantization level of the laser's active material, e.g. quantum well, quantum dot, as well as valuable dispersion properties for the frequency of interest.

$$g(\boldsymbol{r},N,\omega) = -\frac{\omega}{cn_{eff}}\mathbb{I}\left[\chi_e(\boldsymbol{r},N,\omega)\right] \tag{2.24}$$

$$n_e(\boldsymbol{r},N,\omega) = \frac{1}{2n_{eff}}\mathbb{R}\left[\chi_e(\boldsymbol{r},N,\omega)\right] \tag{2.25}$$

For more design oriented readers it can be also interesting to relate the electric susceptibility to more practical physical properties, such as carrier induced material gain, $g(\boldsymbol{r},N,\omega)$, and refractive index change, $n_e(\boldsymbol{r},N,\omega)$. These can be easily expressed as scaled real and imaginary parts of the susceptibility, Eqs. (2.24,2.25). Thus it is also possible to elegantly express the linewidth enhancement factor [8], as the simple ratio of differential real and imaginary parts of the electric susceptibility:

$$\alpha = \frac{\mathbb{R}\left[\partial\chi_e(\boldsymbol{r}, N, \omega)/\partial N\right]}{\mathbb{I}\left[\partial\chi_e(\boldsymbol{r}, N, \omega)/\partial N\right]}. \tag{2.26}$$

The three factors resulting from the electric susceptibility: material gain, refractive index change and linewidth enhancement factor, determine almost all of the characteristics of the semiconductor lasers. The material gain plays a major role in threshold and efficiency of the laser. The refractive index change governs the detuning of the lasing spectra, while the linewidth enhancement factor plays a major role in the spectral linewidth of the output spectra. For all the aforementioned reasons a special attention should be paid to modeling of the material polarization.

It is worth noting that the original semi-classical theory as presented by W. E. Lamb [11], does not incorporate the noise modeling that is present in both carrier and photon populations of the semiconductor lasers. This on the other hand can be considered as a further extension of the semi-classical laser theory. In that case the electric displacement field would have to be expressed in a more general form:

$$\boldsymbol{D}(\boldsymbol{r}, t) = \epsilon_0 \boldsymbol{E}(\boldsymbol{r}, t) + \boldsymbol{P}(\boldsymbol{r}, t) + \boldsymbol{K}(\boldsymbol{r}, t), \tag{2.27}$$

where $\boldsymbol{K}(\boldsymbol{r}, t)$, is the contribution to polarization by the spontaneous emission events.

Due to the nature of the problems considered in this thesis, the realistic modeling of noise sources represents one of the key aspects of the work. The contributing noise sources are included in the framework of statistical physics, i.e. using the Langevin dynamics approach. More details on how this is implemented in the laser simulator developed for the purpose of this thesis, can be found in Ch. 4.

2.3 Material Gain and Quantization Effects

From the classical theory of semiconductor lasers a simple expression for the material gain per unit length can be written as [7]:

$$g = \frac{1}{N_p}\frac{dN_p}{dz} = \frac{R_{st}}{v_g N_p}, \tag{2.28}$$

where N_p is the photon density, and by expanding the stimulated emission rate, R_{st}, using the Fermi's golden rule, one can obtain the gain at a transition energy $\hbar\omega = E_{21} = E_2 - E_1$, defined by the difference between the two discrete energies, E_2 and E_1, located in the conduction and valence band, respectively:

$$g_{21}(\hbar\omega) = \frac{2\pi}{\hbar}\frac{|H_{21}{}'|^2}{v_g N_p}\rho_r(E_{21}) \cdot (f_2 - f_1), \tag{2.29}$$

which relates the material gain to a reduced density of states ρ_r, at a transition energy E_{21}, and to a matrix element $|H_{21}{}'|$, which defines the strength of carrier transition. The variables f_2 and f_1, representing the occupation probabilities of the higher and lower energy states, further express the dependence of material gain on the level of carrier inversion induced by the pumping mechanism of the laser.

Dimension	$\rho(k)$	$\rho(E)$
3	$\frac{k^2}{\pi^2}$	$\frac{\sqrt{E_{21}}}{2\pi^2}\left[\frac{2m_r}{\hbar^2}\right]^{3/2}$
2	$\frac{k}{\pi d_z}$	$\frac{m_r}{\pi\hbar^2 d_z}$
1	$\frac{2}{\pi d_x d_y}$	$\frac{\rho(k)}{\sqrt{E_{21}}}\left[\frac{2m_r}{\hbar^2}\right]^{1/2}$
0	—	$2\delta(E_{21} - E_0)$

Table 2.1: Density of states for Bulk(3D), Quantum well(2D), Quantum wire(1D), Quantum dot(0D) in k-space, and versus energy for parabolic band approximation.

The reduced density of states in Eq. (2.35), describes the density of transition pairs per unit transition energy and assuming that only carrier states with the same k-vectors form the transition pair, the

reduced density of states can be simply related to density of states in the conduction and valence bands, ρ_c and ρ_v, as:

$$\frac{1}{\rho_r} = \frac{1}{\rho_c} + \frac{1}{\rho_v}, \tag{2.30}$$

where ρ_c and ρ_v are in general finite values. For the simplified case where the conduction and valence bands are approximated as parabolic, it is possible to derive a closed-form expression for the density of states [7]. However, in the case of more accurate band structure models, e.g. the $\mathbf{k}\cdot\mathbf{p}$ theory variations considering the effects of coupling between the heavy hole (HH) and light hole (LH) subbands in the valence band or the formation of material strain in the active region can often lead to nonparabolic band structures [15]. In this case it is more practical to express the reduced density of states at the transition energy, $\rho_r(E_{21})$, through density of states in k-space, $\rho(k)$:

$$\frac{1}{\rho_r(E_{21})} = \frac{1}{\rho(k)}\frac{dE_{21}(k)}{dk} = \frac{1}{\rho(k)}\left[\frac{dE_2(k)}{dk} - \frac{dE_1(k)}{dk}\right]. \tag{2.31}$$

Thus by knowing the gradients of the conduction and valence band structures, $dE_2(k)/dk$ and $dE_1(k)/dk$, it is possible to determine the reduced density of states, $\rho_r(E_{21})$, for any corresponding k-vector. The density of states in k-space for different levels of material quantization is given in Table (2.1), and for the approximate case of parabolic conduction and valence bands, their counterparts expressed in terms of energy, $\rho(E)$. For the case of parabolic bands, the reduced mass, m_r, characterizes the parabolic shape of the transition energy E_{21}, and can be expressed in terms of the effective mass of electron and hole, m_c and m_v, respectively:

$$\frac{1}{m_r} = \frac{1}{m_c} + \frac{1}{m_v}. \tag{2.32}$$

In order to write down a more practical form of the material gain, we can use the relation between the matrix element $|{H_{21}}'|$, and the transition matrix element $|M_T|$,

$$\frac{|{H_{21}}'|^2}{N_p} = \frac{q^2\hbar}{2nn_g\epsilon_0 {m_0}^2\omega}|M_T|^2, \tag{2.33}$$

and the definition of the transition matrix element,

$$|M_T|^2 \equiv |\langle u_c|\hat{\mathbf{e}} \cdot \mathbf{p}|u_v\rangle|^2 \cdot |\langle \psi_2|\psi_1\rangle|^2, \tag{2.34}$$

where $u_c(\boldsymbol{r})$ and $u_c(\boldsymbol{r})$, are the conduction and valence band Bloch functions, and $\psi_2(\boldsymbol{r})$ and $\psi_1(\boldsymbol{r})$, the solutions of Schrödinger equation in conduction and valence band, respectively, for a macroscopic potential in case of the quantized structures, e.g. quantum wells, quantum dots. This ultimately allows us to write a more general expression for the material gain per unit length:

$$g_{21}(\hbar\omega) = \frac{\pi\hbar q^2}{n\epsilon_0 c {m_0}^2 \hbar\omega} |\langle u_c|\hat{\mathbf{e}} \cdot \mathbf{p}|u_v\rangle|^2 \cdot |\langle \psi_2|\psi_1\rangle|^2 \cdot \rho_r(E_{21}) \cdot (f_2 - f_1), \tag{2.35}$$

which features most of the relevant properties of the active material. A careful reader might notice at this point that the Eq. (2.35), still considers only a simple two-level band structure. To get a full dispersion of the material gain in case of quantized structures, we would need to take into account the carrier transitions over all the possible combinations of eigenenergies.

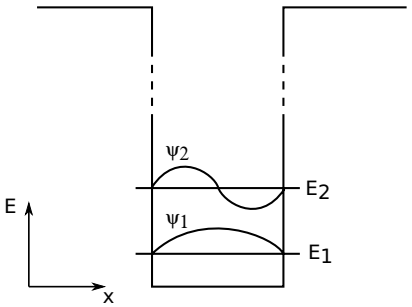

Figure 2.1: Illustration of Schrödinger equation solutions to a quantum well problem in the conduction band.

Aside from the additional transitions energies arising from the quantization of the active material, the uncertainty of the energy levels involved additionally broadens the gain spectrum. The broadening of

the energy states is a result of finite carrier lifetimes at the allowed energy levels. As the broadening of this kind is the same for all the atoms involved in generating the gain dispersion curve, the resulting characteristic of this homogeneous broadening is Lorentzian.

By including the additional transition combinations over the eigenenergies of conduction and valence band Fig. (2.1), and the intrinsic Lorentzian broadening of the energy levels, we can give an example of a more practical expression for the material gain in quantum wells:

$$g(\hbar\omega) = \frac{\pi\hbar q^2}{nc\epsilon_0 {m_0}^2 \hbar\omega} \sum_{m,n} \int_{-\infty}^{\infty} dE' |\langle u_c|\hat{\mathbf{e}}\cdot\mathbf{p}|u_v\rangle|^2 \cdot |\langle\psi_n|\psi_m\rangle|^2 \cdot {\rho_r}^{2D}(E') \times \frac{\gamma/\pi}{\gamma^2 + (E' - \hbar\omega)^2} \cdot [f_c(E', F_c) - f_v(E', F_v)], \tag{2.36}$$

where F_c and F_v, are quasi-Fermi levels of the conduction and valence band. The parameter γ, characterizes the homogeneous broadening and relates directly to the width of the Lorentzian spectral line as FWHM $= 2\gamma$. When it comes to quantum dot and quantum wire arrays we could write out the equations for material gain using a similar procedure as for the quantum well, Eq. (2.36). The major difference would be the presence of the inhomogeneous broadening of the transition energy. The nature of inhomogeneous broadening is not an intrinsic property of the material as for the homogeneous broadening but stems from the particular technologies used for the epitaxial growth of these nanostructures. Namely, as the technology used entails a finite variation in size of the nanostructures in an observed array, the solutions of the Schrödinger equation are consequently affected. The variation in size of quantum dots or quantum wires is often accompanied by varying strain distribution for each element in the array, which adds a further variation to eigenstates. The processes governing the inhomogeneous broadening leads to an additional Gaussian broadening of the gain dispersion which needs to be considered in a comprehensive material gain model.

Chapter 3

Modeling of Quantum Dot Active Material

The quantum dot gain model implemented in the *QD-wave* software is largely based on the models described in [16, 17], which were already shown to be in relatively good agreement with measurements. The model assumes approximate quantum disk geometry for quantum dots which makes it possible to solve the eigenstate problem of the quantum dot semi-analytically. Within the active layers, carriers are assumed to obey the Fermi-Dirac statistics, with static carrier density described by a simple ABC recombination model. In this chapter the model is fully described with discussion of appropriate input parameters for the simulation of realistic quantum dot systems.

3.1 Quantum Dots as Active Material

Since the successful experimental demonstrations of quantum mechanical effects many potential practical applications were hypothesized for devices exploiting such phenomena. Reduction of geometric features of semiconductor materials to de Broglie wavelength can excite new material properties that are not related to material composition and as such can indeed be considered as a new class of materials. Some of the recent research efforts in the area of semiconductor devices based on quantum effects include efficient nanowire light emitting diodes (LEDs) and solar cells [18, 19], high performance quantum well and quantum

dot lasers in fiber-optics [6] or nanowire batteries, where high surface to volume ratio and increased confinement of carrier wavefunctions are exploited.

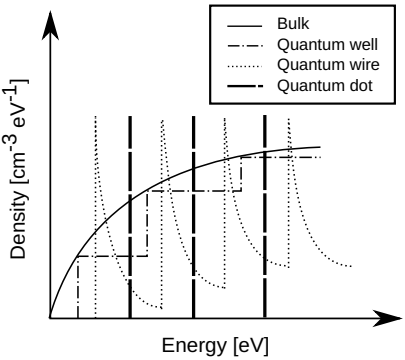

Figure 3.1: Density of states for: bulk semiconductor, quantum well and quantum wire

The main difference that quantized semiconductor materials bring is the modified density of states that stems from the unique atom-like distribution of available energy levels in conduction and valence band. The density of states function, formed through quantization can generate higher density of states than for the same bulk semiconductor material, and most of the desired properties of active semiconductor materials in injection lasers stem either directly or indirectly from such a modified density of states. Quantization of the material geometry, first transforms the density of states function to a step-like function in quantum wells and with further quantization to a delta-like function for quantum wires and quantum dots, Fig. (3.1). In quantum dot based injection lasers this leads to an increased material gain, increased differential gain and reduced frequency chirp under direct current modulation [20].

Today, the quantum dots are grown mainly by Stranski-Krastanov epitaxial growth where the three-dimensional islands are formed spontaneously after the critical layer of lattice-mismatched material is deposited on the substrate. Within these islands the electrons should be ideally confined in all three dimensions, allowing carriers to occupy

only the energy levels permitted by Schrödinger equation. In theory, this should lead to Dirac-like density of states function and ideally symmetric material gain function. However, the variation in size of the quantum dots formed by Stranski-Krastanov growth directly affects the eigenvalue solutions for each dot, leading to inhomogeneous broadening of the spectral lines of the quantum dot array. By including also the energy uncertainty of electrons that leads to homogeneous broadening of the spectral lines within the dots, the density of states function of the real quantum dot systems inevitably strays from the often cited ideal Dirac-like density of states function.

Despite the aforementioned statistical nature of the quantum dot systems, when used as active material in injection lasers, the quantum dots still set the record values when it comes to maximum material gain, low threshold current or reduced frequency chirp. Material gain as high as 150000 cm^{-1}, threshold current densities below 100 $\mathrm{A/cm}^2$ and linewidth enhancement factor below 2, under lasing conditions have been recently reported [20, 21]. For these reasons it is believed that the quantum dot based injection lasers have a high potential in future fiber-optic communications as uncooled, low linewidth and high bit rate signal emitters.

3.2 Approximation of Quantum Dot Geometry

The eigenstate problem of quantum dots is greatly simplified by approximating the dots as quantum disks of radius a and height h. The Schrödinger equation is solved in 3D real space, in a cylindrical coordinate system. The wavefunction solutions in z direction correspond to a finite quantum well problem, whereas the solutions in the $\rho - \phi$ plane correspond to a problem of particle in a circular box. To fully define the extent of carrier confinement under material strain, some basic band structure calculation is also necessary. This is addressed by biaxial strain approximation, that assumes the spatially uniform shift of the quantum dot bands. For a more accurate description of geometry and strain, one could alternatively consider the quantum dot models as in [22, 23].

3.2.1 Strained Band Edges

The material strain occurring at the interfaces between semiconductor materials with mismatched lattice constants, which allows for self-organized growth of quantum dots under Stranski-Krastanov epitaxy, also entails certain side effects. By successively growing two mismatched materials, the atoms forming the semiconductor lattice will inevitably stretch and deform the intrinsic lattice structure of both materials. By altering the lattice structure, as a result the conduction and valence band of the quantum dots are shifted as well, which together with size of the quantum dots ultimately defines the band gap, and consequently determines the resonant wavelength of the quantum dot ground state.

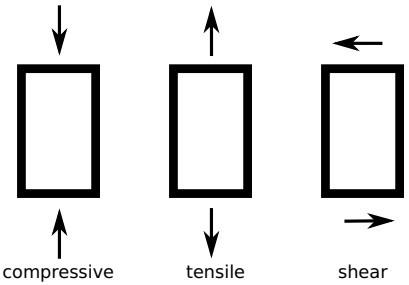

Figure 3.2: Three components of biaxial material stress considered in the quantum dot gain model.

To calculate the modified energies of the band edges a simple strain model is employed, considering only biaxial strain. This simplified approach to material strain allows for straightforward estimation of the band edges which can be then easily tuned to match experimental results or desired lasing frequency of the ground state transition. Biaxial strain calculation is carried out as in [15], with the neglected split-off bands. To match this simple representation to the experiment, adjustments to the band edges in the order of 100 meV are necessary. Having calculated the band edges of the InAs quantum-dots, we have the reference energy values for the quantum disk problem that is solved for both conduction and valence band. However, what is also necessary as the input for the quantum disk calculation are the band offsets at het-

erojuctions surrounding the quantum dot, that determine the potential depth of the respective quantum confinement problems. For this purpose, the results published in [24] were used as a reference point, where the band offsets based on the measurements of the self-aligned InAs quantum dot structure are reported.

3.2.2 Quantum Disk Problem

By assuming the separation of variables, an approximate wavefunction can be derived, that is a product of the solutions in $\rho - \phi$ plane and solutions in z direction:

$$\psi = \psi(z) \cdot \psi(\rho, \phi), \tag{3.1}$$

where the solutions in $\rho - \phi$ plane, are of the form

$$\psi(\rho, \phi) = \frac{1}{\sqrt{2\pi}} \begin{cases} C_1 J_0(p\rho), & \rho \leq a \\ C_2 K_0(q\rho), & \rho > a, \end{cases} \tag{3.2}$$

the values of p and q in Eq. (3.2) are determined from the Cauchy boundary condition with assumed continuity of the wavefunction and its derivative, and the relation

$$(pa)^2 + \frac{{m_d}^*}{{m_b}^*}(qa)^2 = \frac{2{m_d}^*(V_b - V_d)a^2}{\hbar^2}. \tag{3.3}$$

In the equation (3.2), C_1 and C_2 are the constants to be determined from normalization of the wavefunction (3.1), while J and K are Bessel function of the first kind and modified Bessel function of the second kind, respectively. In the equation (3.3), the difference in effective masses of the disk and the barrier material is accounted for as well, by introducing the factor ${m_d}^*/{m_b}^*$. V_b and V_d are the potentials of the quantum disk and the barrier.

For the case of z direction problem, the wavefunctions take the familiar form as in the classical problem of finite quantum well. Therefore, the wavefunctions can be grouped into even and odd solutions:

$$\psi_{even}(z) = \begin{cases} C_3 e^{-\alpha(|z| - h/2)}, & |z| \geq h/2 \\ C_4 \cos(k_z z), & |z| < h/2 \end{cases} \tag{3.4}$$

$$\psi_{odd}(z) = \begin{cases} C_3 e^{-\alpha(|z|-h/2)}, & z > h/2 \\ C_4 \sin(k_z z), & |z| \leq h/2 \\ -C_3 e^{-\alpha(|z|-h/2)}, & z < h/2. \end{cases} \tag{3.5}$$

where the constants C_3 and C_4 are again to be determined from the normalization of the function (3.1), i.e. $\int |\psi|^2 d\rho \; d\phi \; dz = 1$. The constants k_z and α satisfy the relation

$$\left(k_z \frac{h}{2}\right)^2 + \frac{m_d{}^*}{m_b{}^*}\left(\alpha \frac{h}{2}\right)^2 = \frac{2m_d{}^*(V_b - V_d)}{\hbar^2}\left(\frac{h}{2}\right)^2, \tag{3.6}$$

that together with Cauchy boundary conditions and assumed continuity of the wavefunction and its derivative, yields the solutions in the axial direction.

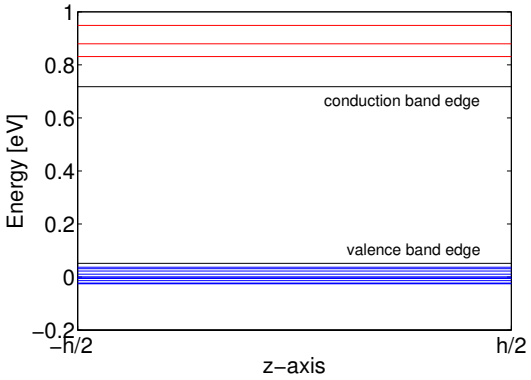

Figure 3.3: Calculated conduction and valence eigenenergies of a $1.55\mu m$ quantum dot epi-structure, along the quantum dot height, h.

Now having properly defined the quantum disk problem, the wave equations together with eigenenergies can be calculated, Fig. (3.3). Where the total eigenenergy in the disk is approximated as a sum of eigenenergies in transverse and longitudinal directions

$$E_d = E_\rho + E_z = \frac{\hbar^2}{2m_d{}^*}\frac{(pa)^2}{a^2} + \frac{\hbar^2}{2m_d{}^*}\frac{(k_z(h/2))^2}{(h/2)^2}. \tag{3.7}$$

The calculation of eigenfunctions and eigenenergies is coded as a single module that after execution returns not only the elementary solutions of quantum disk problem but also the calculated overlap integrals between all the wavefunctions

$$\begin{aligned} I_{WF} &= \langle\psi_1|\psi_2\rangle \equiv \int {\psi_1}^* \cdot \psi_2 \; d\rho \; d\phi \; dz \\ &= \int \psi_1(\rho,\phi)^* \cdot \psi_2(\rho,\phi) \; d\rho \; d\phi \cdot \int \psi_1(z)^* \cdot \psi_2(z) \; dz. \end{aligned} \tag{3.8}$$

The calculated eigenenergies Fig. (3.3), as well as the overlap integrals between the wavefunctions, Table (3.1), are calculated by assuming the flat bands around the individual quantum dots, i.e. with the neglected effect of the electric field bias.

	$\|\psi_{v1}\rangle$	$\|\psi_{v2}\rangle$	$\|\psi_{v3}\rangle$	$\|\psi_{v4}\rangle$
$\|\psi_{c1}\rangle$	**0.9730**	0.0313	0.0319	0.0328
$\|\psi_{c2}\rangle$	0.0320	**0.9718**	0.0331	0.0340
$\|\psi_{c3}\rangle$	0.0341	0.0346	**0.9678**	0.0364

Table 3.1: Calculated overlap integrals between first three wavefunctions of the conduction band and first four valence band wavefunctions

The calculated overlap integrals as weight functions, Eq. (3.8), and eigenstate solutions are then further passed, as a final result, to complement the calculation of optical gain and refractive index change. An example of calculated overlap integrals for first few wavefunction pairs, Table (3.1), for InAs/GaAs quantum dot system, with electron and hole effective masses of, $0.023 \cdot m_0$ and $0.3 \cdot m_0$, respectively, implies that the major contribution to radiative recombination is through orthogonal wavefunctions. These values are typically $5 - 10\%$ lower than ideal unity [7], while in the case of identical electron and hole effective masses in the conduction and valence band, they would be equal to unity.

3.3 Carrier Density and Quasi-Fermi Levels

In order to calculate the surface carrier densities of the active quantum dot layers, it is assumed that the surface current densities are known. From given surface current densities the carrier densities can be calculated for the given recombination parameters of the active region. If we assume that the stimulated emission does not affect the carrier density significantly, i.e. that the device is close to the threshold operating conditions, the effect of the stimulated emission on carrier density can be neglected. In case of the ABC recombination model, the simplified equation for the surface current density can be written in the following form

$$J = \frac{qZ_aN_l}{\eta_{inj}} \left[A\left(\frac{n_{2D}}{Z_{leff}}\right) + B\left(\frac{n_{2D}}{Z_{leff}}\right)^2 + C\left(\frac{n_{2D}}{Z_{leff}}\right)^3 \right], \tag{3.9}$$

where q is the elementary charge, η_{inj} the carrier injection efficiency, Z_a the thickness of the total active region, N_l number of quantum dot layers and Z_{leff} the effective thickness of a single quantum dot layer including the wetting layer. Using the Eq. (3.9), the surface carrier densities of quantum dot layers can be calculated, where carriers within the active layers are treated as free, which leads to uniform surface carrier densities across the active quantum dot layers. Moreover, as the thickness of the active layer, Z_{leff}, is considered as effective if chosen appropriately it can also account for the lateral carrier density variation across the active layers.

The stimulated emission component can be added as well, in which case the surface current density would read

$$J = \frac{qZ_aN_l}{\eta_{inj}} \left[A\left(\frac{n_{2D}}{Z_{leff}}\right) + B\left(\frac{n_{2D}}{Z_{leff}}\right)^2 + C\left(\frac{n_{2D}}{Z_{leff}}\right)^3 \right] + \frac{q}{\eta_{inj}} \frac{\Gamma g(n_{2D}) P_o}{\hbar\omega_s w}, \tag{3.10}$$

where Γ is the confinement factor, $g(n_{2D})$ the gain for a given surface carrier density, P_o the output signal power, ω_s frequency of the lasing

signal transition and w the width of the laser waveguide. However, to calculate the carrier densities from Eq. (3.10), the quasi-Fermi levels would have to be solved numerically at every iteration/increment of the carrier density in order to determine the material gain in the stimulated emission component. This was unfortunately shown to lead to slow calculation times. However, by using some of the simple approximations for the suppression of the material gain we can successfully address this problem in the subsequent time-domain simulation.

To determine the quasi-Fermi levels necessary for the calculation of material gain and refractive index change, the density of states and carrier statistics have to be known. Basic expressions relating the electron and hole carrier densities to quasi-Fermi levels can be written in the form

$$n = \int \rho_c(E) f(E) dE, \tag{3.11}$$

$$p = \int \rho_v(E)[1 - f(E)] dE, \tag{3.12}$$

where n and p are electron and hole carrier densities, respectively, $\rho_c(E)$ and $\rho_v(E)$, the corresponding density of states and $f(E)$, the Fermi-Dirac distribution containing the quasi-Fermi levels. To simplify the problem, in the case of parabolic conduction and valence bands, the electrons and holes can be treated as free charges where their effective masses, m_e and m_h, respectively, are used to account for the effect of the semiconductor crystal structure. For further simplification of the problem, the conduction and valence band edges within the quantum dot can be considered as uniform. This naturally strays from reality as the strain forming between the lattice-mismatched materials leads to distortion of intrinsic material properties. This can be addressed with more complex models [23, 25], which is however out of the scope of this work. The aforementioned approximations, apply not only to calculation of quasi-Fermi levels but also to solving of quantum dot eigenstate problem described earlier, and to the calculation of material gain and refractive index change presented in the following section.

The simplified, but still nonlinear equations for the electron and hole carrier density of the quantum dot array are adopted from [17], where in case of the 2D electron carrier density the equation reads

$$
\begin{aligned}
n_{2D} = N_D \sum_i \frac{s^i}{\sqrt{2\pi {\sigma_e}^2}} \int_a^b e^{-\left({E_c}' - {E_{ci}}^D\right)^2 / 2{\sigma_e}^2} \frac{1}{1 + e^{({E_c}' - F_c)/k_B T}} d{E_c}' \\
+ \sum_l \frac{{m_e}^W k_B T}{\pi \hbar^2} \ln(1 + e^{({F_c} - {E_{el}}^W)/k_B T}) \\
+ t_b \int \frac{1}{2\pi^2} \left(\frac{2{m_e}^B}{\hbar^2} \right)^{3/2} \sqrt{{E_c}' - {E_c}^B} \frac{1}{1 + e^{({E_c}' - F_c)/k_B T}} d{E_c}',
\end{aligned}
\tag{3.13}
$$

and hole carrier density,

$$
\begin{aligned}
p_{2D} = n_{2D} = N_D \sum_j \frac{s^j}{\sqrt{2\pi {\sigma_h}^2}} \int_a^b e^{-\left({E_h}' - {E_{hj}}^D\right)^2 / 2{\sigma_h}^2} \frac{1}{1 + e^{(F_v - {E_v}')/k_B T}} d{E_h}' \\
+ \sum_m \frac{{m_h}^W k_B T}{\pi \hbar^2} \ln(1 + e^{(F_v - {E_{hm}}^W)/k_B T}) \\
+ t_b \int \frac{1}{2\pi^2} \left(\frac{2{m_e}^B}{\hbar^2} \right)^{3/2} \sqrt{{E_h}' - {E_h}^B} \frac{1}{1 + e^{(F_v - {E_h}')/k_B T}} d{E_h}'.
\end{aligned}
\tag{3.14}
$$

The Eq. (3.13) and Eq. (3.14), describing the surface carrier densities, consist of three components contributing to total electron/hole carrier density. The three components in summation correspond to quantum dots, the wetting layer and the barrier layer, respectively. In the prefactor of the firs component, N_D is the surface density of the quantum dots, $\sigma_{e/h}$ the inhomogeneous broadening of the quantum dots due to intrinsic variation of dot size, and $s^{i/j}$ the degeneracy of eigenstates due to the spin and geometrical symmetry. The carrier distribution within the dots is included under the integral of the first component as familiar Fermi-Dirac distribution. The remaining two components describe the wetting layer and the t_b thick barrier layer between the active quantum dot layers. The wetting layer is described by the l/m

energy levels while for the description of the barrier layer a single energy level was used.

As both of the equations describing the electron and hole carrier density are nonlinear, the roots of the equations have to be found numerically. In short, the procedure consist of ramping of the carrier densities, n_{2D} and p_{2D}, in finite steps, while numerical root finding procedure is executed at each of the ramping steps [26], to solve the Eqs. (3.13,3.14). Moreover, the ramping is continued in this manner until the root condition is satisfied for varying quasi-Fermi levels of the conduction and valence band, F_c and F_v, covering ideally the cases from maximum absorption to full inversion. Having calculated the quasi-Fermi levels and solved the quantum dot eigenstate problem, the material gain and refractive index change, as important parameters determining the quality of the lasing material, can now be calculated at different steady states.

3.4 Gain and Refractive Index Dispersion

Under the lasing conditions, the photons traveling through semiconductor laser cavity experience exponential growth through the process of stimulated emission. The material gain that makes the lasing possible, depends on many factors, such as material composition, strain or material quantization. In all scenarios however, carrier inversion is a necessary precondition for transition from lossy to gain medium, fulfilled either through carrier injection or optical pumping of the active medium.

Considering the refractive index of the active medium as a general complex function, with its real and imaginary components, i.e. refractive index and material gain/loss related by the Kramers-Kronig relation, one can calculate the complete complex function by knowing either of its two components, see Appendix A. As a consequence of this fact, the linewidth enhancement factor [8], determining the strength of this coupling and the quality of lasing medium, can also be extracted with respect to the level of carrier inversion.

3.4.1 Quantum Dot Material Gain

By adapting the material gain equation Eq. (2.35), for the case of quantum dot active material one can get for a single quantum dot layer a somewhat simplified form of the material gain, that is used to determine the material gain dispersion at varying carrier densities:

$$g(\hbar\omega) = \frac{\pi\hbar q^2}{nc\epsilon_0 {m_0}^2\hbar\omega}\sum_i \int_{-\infty}^{\infty} dE' |\langle u_c|\hat{\mathbf{e}}\cdot\mathbf{p}|u_v\rangle|^2 \cdot |\langle\psi_2|\psi_1\rangle|^2 \times D(E')L_g(E',\hbar\omega)[f_c(E',F_c) - f_v(E',F_v)], \tag{3.15}$$

where q is the elementary charge, n the refractive index, ϵ_0 vacuum permittivity, and ω the angular frequency. The two major approximations leading to Eq. (3.15), are compressive strain and the orthogonality of confined carrier wavefunctions of the quantum dot. As the compressive strain within the InAs quantum dots, resulting from the lattice-mismatched material surrounding it, leads to separation of light-hole (LH) and heavy-hole (HH) bands, it is assumed that the radiative recombination occurs only over C-HH transitions. The orthogonality of quantum dot wavefunctions allows for further simplification, with overlap integrals $|\langle\psi_2|\psi_1\rangle|$, being ideally zero between the non-orthogonal wavefunction pairs, can be also neglected in these cases without loosing on generality. In the end, this explains the simple summation over single index i, that accounts only for the radiative transitions of the form C_i-HH_i, with i being the index of the orthogonal quantum dot wavefunctions.

The degeneracy of quantum dot states in Eq. (3.15), is included within the density of states, where $D(E')$ reflects the Gaussian or rather inhomogeneous broadening of the spectral lines, stemming from the intrinsic variation in dot size. The inhomogeneous broadening can be defined as

$$D(E') = \frac{s^i}{V_{dot}^{eff}}\frac{1}{\sqrt{2\pi\sigma^2}} exp\left(\frac{-(E' - E_{max}^i)}{2\sigma^2}\right), \tag{3.16}$$

and the Lorentzian component $L_g(E',\hbar\omega)$, reflecting the homogeneous broadening as

$$L_g(E', \hbar\omega) = \frac{1}{\pi\gamma\left[1 + \left(\frac{E'-\hbar\omega}{\gamma}\right)^2\right]}, \tag{3.17}$$

where s^i is the state degeneracy and $V_{dot}^{eff} = h/N_D$, the effective volume of quantum dots, with h being the dot height and N_D the surface density of quantum dots.

3.4.2 Refractive Index Change

The change in material gain/loss caused by filling of the carrier states in conduction and valence band, results in coupled change of the refractive index, see Appendix A. Having derived the equation for the material gain of quantum dots, it is not difficult to obtain the expression for the refractive index change, via Kramers-Kronig relation, that causes the phase distortion of the laser field, and thus the increase of spectral linewidth. To this end, it is sufficient to transform the ω dependent components in Eq. (3.15), i.e. the Lorentzian $L_g(E', \hbar\omega)$ and the prefactor before the sum. By performing the Kramers-Kronig transform of the Lorentzian

$$\frac{1}{1+\omega^2\tau^2} \xrightarrow{Kramers-Kronig} \frac{-\omega\tau}{1+\omega^2\tau^2}, \tag{3.18}$$

the resulting expression for the refractive index change can be written as

$$\begin{aligned} n_e(\hbar\omega) = {} & \frac{\pi\hbar^2 q^2}{2nc\epsilon_0 {m_0}^2 (\hbar\omega)^2} \sum_i \int_{-\infty}^{\infty} dE' |\langle u_c|\hat{\mathbf{e}}\cdot\mathbf{p}|u_v\rangle|^2 \cdot |\langle\psi_2|\psi_1\rangle|^2 \\ & \times D(E') L_r(E', \hbar\omega)[f_c(E', F_c) - f_v(E', F_v)], \end{aligned} \tag{3.19}$$

where $L_r(E', \hbar\omega)$ is the Kramers-Kronig transform of the Lorentzian $L_g(E', \hbar\omega)$. Having calculated both the material gain and the refractive index change, the linewidth enhancement factor (LEF), α-factor, can be computed easily as well:

$$\alpha = -\frac{4\pi}{\lambda}\frac{\partial n_e/\partial N}{\partial g/\partial N}, \tag{3.20}$$

with N being the injected carrier density in the active region. The LEF calculation is done numerically, where $\partial n_e/\partial N$ and $\partial g/\partial N$ gradients are approximated by performing the gain and refractive index calculations with finitely small increments of the injected carrier density N, around the considered steady state.

3.5 Calibrating the Gain Model Parameters

Under the approximations of quantum dot model described in this chapter, one can successfully extract all the relevant parameters necessary for laser simulation in frequency or time domain. However, to apply the model to fabricated lasing diodes some calibration of the input parameters is necessary. The calibration can be split into three major problems: the level of homogeneous and inhomogeneous spectral broadening, degeneracy of the quantum dot energy levels and the strength of interaction between the conduction and valence band states described by the transition matrix element. For this purpose the available experimental data in [27–29], was used to study the implications of different parameters and calibrate the gain model before the time-evolution of the laser problem with traveling wave model.

3.5.1 Spectral Broadening in Quantum Dots

The spectral broadening mechanisms within a three-dimensional quantum dot array can be categorized by their selectivity, i.e. whether they affect all quantum dots within the array uniformly or vary from quantum dot to quantum dot. The homogeneous broadening that can be considered to apply to all quantum dots the same, and stems mainly from the uncertainty principle, that is intrinsic to quantum mechanics, and the many-body effects that are present at high carrier densities, typical for the operating laser diodes. On the other hand, the inhomogeneous spectral broadening is not directly related quantum nature

of the charge carriers but is a result of the variation in quantum dot size, that results in the variation of eigenenergy solutions to quantum mechanical problem of the dots, Fig. (3.4).

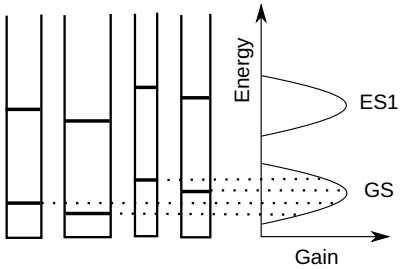

Figure 3.4: Illustration of quantum dot geometry variation and its effect on eigenenergies and material gain dispersion.

The homogeneous broadening being a property of nature itself, it always has to be present to certain extent. Whereas the inhomogeneous broadening is fixed to technology, i.e. to the Stranski-Krastanov epitaxial growth that is commonly used, under which the quantum dots are spontaneously self-organized and generated by the effects of material strain. However, the same process also leads to spontaneously defined quantum dot size that has a certain variance to it. Within the previously described quantum dot gain model, the homogeneous and inhomogeneous broadening are included by γ and σ factors, respectively, in Eqs. (3.13, 3.14, 3.17, 3.16). In practice however, the two broadening mechanisms are characterized by the full width at half maximum (FWHM) of the respective Lorentzian and Gaussian curves. The parameter γ, for homogeneous broadening is directly related to the FWHM as

$$\mathrm{FWHM}_{hom.} = 2 \cdot \gamma, \tag{3.21}$$

while the variance of inhomogeneous broadening relates to the FWHM of the Gaussian curve as

$$\mathrm{FWHM}_{inhom.} \approx 2.35482 \cdot \sigma, \tag{3.22}$$

where the spectral variance with contributions of both electrons and holes reads

$$\sigma^2 = {\sigma_e}^2 + {\sigma_h}^2. \tag{3.23}$$

For further results in the text, the FWHM of the homogeneous and inhomogeneous broadening are considered to be 10 and 50 meV [16], respectively, unless it is specified otherwise. Moreover, the energy levels to which the spectral broadening is added are a solution of approximate quantum disk problem, meaning that they would also have to be adjusted for accurate device simulation. For this purpose the experimental data in [27], was used to calibrate the calculated energy levels of the quantum dot, as the same epitaxial structure was used in Ch. 5 to study the spectral linewidth and related effects in 1.55 μm quantum dot injection lasers.

3.5.2 State Degeneracy in Quantum Dots

Considering that the symmetry group of quantum dot translates to the symmetry of the Hamiltonian, the accurate representation of dot geometry is essential in determining the spectrum of the energy levels of the quantum dot. The symmetries can be generally classified into discrete and continuous. An example of discrete symmetry is a mirror symmetry while rotation would be an example of continuous symmetry [30]. A set of unitary operators that preserve the scalar product of the eigenstates, form a symmetry group of the respective Hamiltonian. Mathematically, for a unitary operator in Hilbert space, $\hat{U}$, this implies

$$\langle\phi|\psi\rangle = \langle\hat{U}\phi|\hat{U}\psi\rangle = \langle\phi|\hat{U}^\dagger\hat{U}\psi\rangle = \langle\phi|\psi\rangle, \tag{3.24}$$

and in the case of Hamiltonian a commutation

$$\hat{U}^\dagger\hat{H}\hat{U} = \hat{H}, \quad \text{i.e. } [\hat{H}, \hat{U}] = 0. \tag{3.25}$$

As a corollary it can be shown that for a unitary operator $\hat{U}$, which commutes with a Hamiltonian $\hat{H}$, this leads to the concept of degenerate eigenstates. In other words, for an eigenstate $|\psi\rangle$, of a Hamiltonian $\hat{H}$, it follows that the eigenstate $\hat{U}|\psi\rangle$ will be an eigenstate with the same eigenvalue. This can be expressed as

$$\hat{H}(\hat{U}|\psi\rangle) = \hat{U}\hat{H}|\psi\rangle = E_n(\hat{U}|\psi\rangle). \tag{3.26}$$

Parameter	Value
Number of quantum dot layers, N_l	5
Quantum dot density, N_{dot}	$3.25 \cdot 10^{10}$ cm^{-2}
Quantum disk height, h	2 nm
Effective active layer thickness, Zl_{eff}	1 nm
Electron effective mass (InAs), m_e	$0.023 \cdot m_0$
Heavy-hole effective mass (InAs), m_{hh}	$0.3 \cdot m_0$
Homogeneous broadening (electrons and holes)	15 meV
Inhomogeneous broadening	10 meV
Confinement factor, Γ	0.0225
Effective refractive index, n_{eff}	3.23

Table 3.2: Gain model parameters of the 5QD-layer epi-structure

In the case of quantum dots, either for the sake of simplicity or merely to demonstrate some general properties of quantum dots as active laser material, their geometry is often approximated with a three-dimensional quantum box [7, 15], or the degeneracy of energy levels is heuristically determined [16, 31]. From the equations describing the material gain and refractive index change of the quantum dot system, Eqs. (3.15, 3.19), it can be seen that the degeneracy of the eigenstates enters both equations through density of states, affecting not only the gain and refractive index of the quantum dot material but also the linewidth enhancement factor that is a consequence of their coupling through Kramers-Kronig relation. To study the importance of eigenstate degeneracy we can compare a few calculations of material gain dispersion for 1.55 μm system with five quantum dot layers, using the gain model parameters given in Table (3.2). The confinement factor in Table (3.2), is given for a uniform 3 nm thick active layer, while the effective confinement factor is naturally lower as the irregular positioning of the quantum dots needs to be taken into account.

The calculated material gain dispersion, depicted in Figs. (3.5,3.6), for two different degeneracy sets of the first three carrier transitions suggest that higher degeneracy of elevated states, ES1 and ES2, also leads to higher material gain at corresponding frequencies. However, the experimental results reported in [27], with all three carrier transitions inverted, show reduced material gain at higher energy transi-

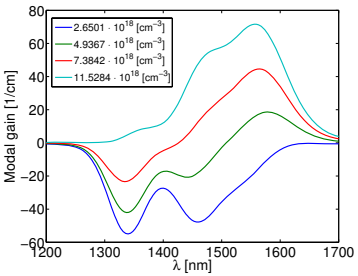

Figure 3.5: Modal gain of five QD-layers with level degeneracies of GS, ES1 and ES2, being 2, 2 and 2, respectively.

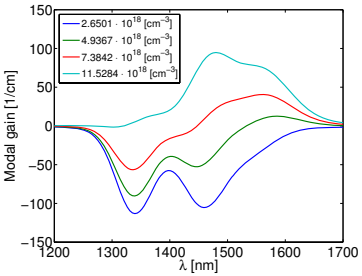

Figure 3.6: Modal gain of five QD-layers with level degeneracies of GS, ES1 and ES2, being 2, 4 and 4, respectively.

tions. Naturally, one could question now the higher number of degenerate states for elevated quantum dot energy levels. Considering that the higher degeneracy stems from the symmetry of the quantum dots, one explanation for this phenomenon would be an imperfect geometry of quantum dots deposited by Stranski-Krastanov growth. From the available SEM images of the self-organized quantum dots, one can notice that the real dot geometry strays from the ideal truncated pyramid or cubical quantum dot, which makes the standard double degenerate energy levels statistically more likely. Aside from reduced symmetry of quantum dots, other factors that perturb the solution of Schrödinger equation include the presence of material strain between lattice mismatched materials or under operating conditions, the electric field between the laser contacts.

To further elaborate the issue, we could also investigate the dispersion of the linewidth enhancement factor of the same quantum dot system, without the contribution of the wetting and barrier layers as it was described in 3.4.2. The contribution of elevated energy levels to linewidth enhancement factor can be significant nevertheless [29], however, for the study of importance of the state degeneracy we will limit the problem to quantum dot itself and its three main conduction-heavy hole (C-HH) carrier transitions. In Figs. (3.7,3.8), comparing again the same degeneracy sets as for the gain dispersion, one can also notice a distinct difference in the linewidth enhancement factor.

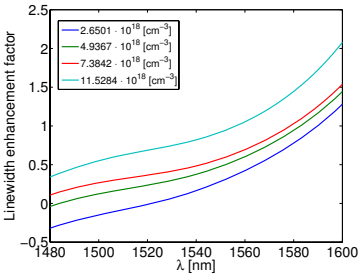

Figure 3.7: Linewidth enhancement factor of five QD-layers with level degeneracies of GS, ES1 and ES2, being 2, 2 and 2, respectively.

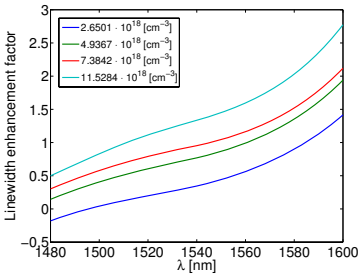

Figure 3.8: Linewidth enhancement factor of five QD-layers with level degeneracies of GS, ES1 and ES2, being 2, 4 and 4, respectively.

In case of the standard double degenerate eigenenergies, for the first three energy levels, linewidth enhancement factor amounts to roughly 0.6 at the ground state transition, whereas in case of the increased state degeneracy it doubles to 1.2 at the same wavelength. Both of these values can be considered lower than what is usually reported for bulk and quantum well materials. However, below threshold or rather when the contribution of the wetting layer due to the Pauli blocking effect is low, measurements tend to show better matching of the linewidth enhancement factor at the ground state wavelength for the case of standard double degenerate eigenstates [29], which is where the gain model described here can be considered to have better overlap with measurements, as it does not include the gain contribution of the wetting and barrier layers.

3.5.3 Transition Matrix Element

When it comes to the transition matrix element, some parameter tuning is also necessary as the transition matrix element that determines the carrier transition probability between the conduction and valence bands depends on the quantum dot geometry and strain that are statistically defined. By definition the transition matrix element, Eq. (3.27), is comprised of two components: $|\langle u_c|\hat{\mathbf{e}}\cdot\mathbf{p}|u_v\rangle|^2$, the transition

strength between conduction and valence band including the polarization dependence and the envelope function overlap integral, $|\langle\psi_2|\psi_1\rangle|^2$.

$$|M_T|^2 \equiv |\langle u_c|\hat{\mathbf{e}}\cdot\mathbf{p}|u_v\rangle|^2 \cdot |\langle\psi_2|\psi_1\rangle|^2 \tag{3.27}$$

We need to express the transition matrix element, Eq. (3.27), giving the transition probability between conduction band Bloch function and valence band Bloch functions (u_{hh}, u_{lh}, u_{so}), in terms of the momentum matrix element $|M|^2$, that gives the transition probabilities between conduction band Bloch function and three basis Bloch functions related to three p atomic orbitals, (p_x, p_y, p_z). In practice the momentum matrix element can be measured accurately using the electron spin resonance techniques [7], or from theory by using the $\mathbf{k}\cdot\mathbf{p}$ perturbation method. For simplicity we will assume the carrier transition near the band gap where the transversal component of the electron $\mathbf{k}$-vector equals zero while the parameters of the transition matrix element can be adjusted by relying on the experimental results, to compensate for the adopted approximations. By expanding the valence band Bloch function u_v, in terms of basis Bloch functions one can express the transition matrix element for three valence subbands (u_{hh}, u_{lh}, u_{so}), in terms of the momentum matrix element [7]:

$$|M_T|^2 \equiv \begin{cases} \frac{1}{2}(1-|\hat{\mathbf{k}}\cdot\hat{\mathbf{e}}|^2)\cdot|M|^2\cdot|\langle\psi_2|\psi_1\rangle|^2, & \text{for HH band} \\ \frac{1}{2}(\frac{1}{3}-|\hat{\mathbf{k}}\cdot\hat{\mathbf{e}}|^2)\cdot|M|^2\cdot|\langle\psi_2|\psi_1\rangle|^2, & \text{for LH band} \\ \frac{1}{3}\cdot|M|^2\cdot|\langle\psi_2|\psi_1\rangle|^2, & \text{for SO band} \end{cases} \tag{3.28}$$

The Eqs. (3.28) reveal the polarization dependence of the transition matrix element, where the interaction strength between the electron and photon depends on the angle between the electron $\mathbf{k}$-vector and the electric field polarization unit vector, $\hat{\mathbf{e}}$. However, other than this theoretical remark, these simple relations do not provide much help in terms of practical use with the quantum dot gain model. For this purpose it is necessary to consider the effects of the quantization and polarization.

In the simple case of free electrons, where the envelope function can be described by a simple plane wave, the polarization factor $|\hat{\mathbf{k}}\cdot\hat{\mathbf{e}}|^2$ can be easily determined with respect to the angle between the electron and electric field unit vectors. Following from this simple example one

can find that the transition matrix element gives the maximum for perpendicular unit vectors in the case of C-HH transition, while in the case of C-LH transition when the unit vectors are parallel. However, as it was shown in section 3.2.2, in the case of quantum dots the envelope function is comprised of multiple plane waves even for the approximate quantum disk model while in reality the exact geometry also varies from dot to dot. For this reason, we bypass the stochastic problem of varying dot geometry and the Hamiltonian by describing the factors preceding $|M|^2$, in Eq. (3.28), with a single factor, ξ, that can be used to fit the gain peak calculated with the quantum dot gain model to available experimental measurements.

$$|M_T|^2 = \xi \cdot |M|^2 \cdot |\langle \psi_2 | \psi_1 \rangle|^2 \tag{3.29}$$

By using the transition matrix in form of Eq. (3.29), with the quantum dot gain model we essentially compensate for the approximation of the dot geometry and fit the average polarization and quantization contributions to the transition matrix element by a single factor, ξ.

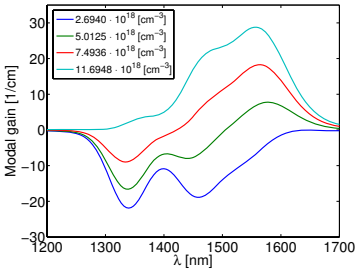

Figure 3.9: Modal gain of two QD-layers with all three energy levels, GS, ES1 and ES2, being double degenerate.

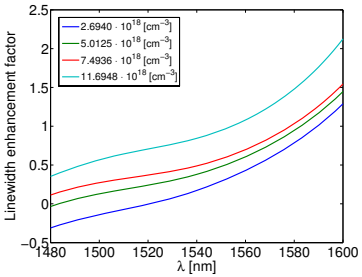

Figure 3.10: Linewidth enhancement factor of two QD-layers with all three energy levels, GS, ES1 and ES2, being double degenerate.

After a few iterations, using the developed quantum dot gain model, we estimate the ξ factor to 3.1, where a vectorial mode solver is applied to determine the confinement factor of the active layers. Using the parameters given in Table (3.3), the dispersion of gain and linewidth enhancement factor of a non-lasing quantum dot material show a

Parameter	Value
Number of quantum dot layers, N_l	2
Quantum dot density, N_{dot}	$3.25 \cdot 10^{10}$ cm^{-2}
Quantum disk height, h	2 nm
Effective active layer thickness, Zl_{eff}	1 nm
Electron effective mass (InAs), m_e	$0.023 \cdot m_0$
Heavy-hole effective mass (InAs), m_{hh}	$0.3 \cdot m_0$
Homogeneous broadening (electrons and holes)	15 meV
Inhomogeneous broadening	10 meV
Confinement factor, Γ	0.009
Effective refractive index, n_{eff}	3.23

Table 3.3: Gain model parameters of the 2QD-layer epi-structure

good overlap with available experimental results [28,29]. As the study of spectral linewidth presented in later chapters relies heavily on the high-gain InAs quantum dot system described in [28], the published experimental results are used to calibrate the gain model accordingly, Figs. (3.9,3.10). The results in [28], allow us mainly to calibrate the peak modal gain, the internal losses and the qualitative behavior of the gain dispersion, while the calibration of calculated quasi-Fermi levels and the recombination parameters is performed by relying on the measured LI-curves of the laser samples based on the same epitaxy, Ch. 5. To stay consistent with the gain model, described in section 3.4, for simplicity only the C-HH carrier transitions are considered for the transition matrix element.

3.5.4 Pauli Blocking Effect and Linewidth Enhancement

By introducing the quantization in semiconductor materials, Fig. (3.1), it is theoretically possible to achieve Dirac-like density of carrier states. Compared to bulk semiconductor material, this allows for confinement of the carriers to narrow energy-bands which results in higher differential and modal gain in semiconductor lasers. In directly modulated quantum dot lasers these features allow for high modulation-

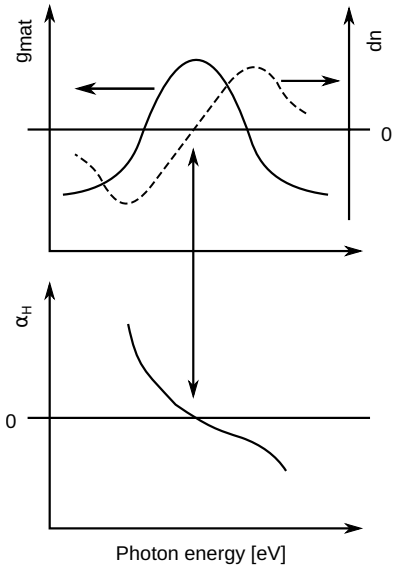

Figure 3.11: Illustration of ideally symmetric gain dispersion, leading to zero linewidth enhancement factor at gain peak through Kramers-Kronig relation.

bandwidths. As an accompanying feature, high symmetry of the quantum dot material gain is often present, which can lead to a very low linewidth enhancement factor compared to the quantum well and bulk lasers.

High material gain symmetry results mainly from the narrow density of states and a relatively high separation of quantum dot ground state and elevated energy states, while resulting low linewidth enhancement factor can be explained by the Kramers-Kronig relation, which links the material gain and refractive index change under carrier injection. Low linewidth enhancement factor is related to narrow spectral linewidth and low frequency chirp or rather better dynamic properties altogether, with both direct and external modulation of the laser light.

However, the highly idealistic case depicted in Fig. 3.11, often diverges from reality. Ideally symmetric material gain can be shown to lead to zero linewidth enhancement factor, as the refractive index

change in that case is also zero at the gain peak, causing no additional phase shift to the laser light. As it is demonstrated by measurements [21, 29], very low linewidth enhancement factor can be achieved near the lasing threshold in quantum dot semiconductor lasers. From the same results it can be also noticed however, that at higher injection currents, the non-resonant carriers in elevated energy states contribute significantly to the linewidth enhancement factor. As a direct consequence of the Pauli exclusion principle and a limited number of quantum dots in the active region of the laser, the injected carriers unable to occupy the quantum dot ground state, inevitably find their place in one of the elevated quantum dot states or in the wetting layer. This effect, better known as the Pauli blocking, leads to increasing asymmetry of the gain dispersion with increasing injection current, as the non-resonant carriers accumulate in the wetting layer and thus increase the material gain on the high-energy side of gain dispersion. As a result, if one seeks to minimize the laser linewidth through linewidth enhancement factor, the laser design should ensure the low saturation of quantum dot ground state to prevent the negative effect of Pauli blocking. In terms of gain threshold of the laser diode this translates to carrier clamping at lower gain values, which can be achieved either through higher material gain peak by increasing the number of active quantum dot layers or by increasing the quality factor of laser cavity.

Following from the Schawlow-Townes spectral linewidth equation, Eq. (1.4), a narrow linewidth that is of interest in optical communications unfortunately does not occur at lasing threshold but at higher output powers where Pauli blocking as well as the other negative effects become significant [32, 33]. For this reason, the quantum dot gain model described here, has to be complemented with an appropriate linewidth enhancement factor model that takes into account the distortion of the gain dispersion and linewidth enhancement factor at higher injection currents caused by the carriers accumulating at higher energies. For this purpose a rate equation based model, derived by S. Melnik et al. [34], is implemented together with the gain dispersion model in the *QD-wave* laser simulator, to describe the evolution of the spectral linewidth with increasing injection current more accurately.

$$\alpha_{FM/AM} \equiv F(\omega_{min}) = \alpha_d + \alpha_{nr} \frac{\gamma_d}{C(1-\rho_{th})^2} \frac{\rho_{th} - 1 + \rho_{th}\frac{J_{dc}}{J_{th}}}{2\rho_{th} - 1} \qquad (3.30)$$

The complementing linewidth enhancement factor model is based on the quantum dot representation, comprised of one nonresonant carrier population, representing the wetting layer and other elevated energy states, and the quantum dot ground state. Such a representation of the quantum dot system leads to an elegant analytic form for the modified linewidth enhancement factor, Eq. (3.30). The modified description includes both the intrinsic linewidth enhancement factor α_d, calculated by the quantum dot gain model and the linewidth enhancement component α_{nr}, due to the nonresonant carriers at higher energy levels. Other parameters include: quantum dot population at threshold ρ_{th}, carrier decay rate within the quantum dot γ_d, carrier capture rate from the wetting layer to quantum dot C, and the injection and threshold current densities, J_{dc} and J_{th} respectively. A more complex description could consider the variation of quantum dot size [32], however this would require a numerical estimation of the problem, which would thus degrade both the elegance of the solution and the simulation time of the time-domain laser simulation that is already critical in case of the narrow spectral linewidths [14], found in modern semiconductor lasers.

Chapter 4

Dynamic Modeling of Semiconductor Lasers

Aside from the quantum dot gain problem discussed in the previous chapter, here we describe in detail the remaining two modules of the laser simulator, dedicated to the traveling wave simulation and noise analysis. The developed multi-section simulator for edge-emitting laser diodes is based on the time-domain traveling wave (TDTW) model, popularized initially by Carroll et al. [35]. Instability of the transversal mode is neglected, and therefore only the fundamental TE_{10} mode is considered for the transversal problem. This allows for great simplification and economy of computational resources, by separating the edge emitting laser problem by spatial variables into transversal and axial problems. Transversal problem is solved by the already available finite element solver while the axial problem is addressed in greater detail by developing a custom edge-emitting laser simulator taking into account various effects relevant to the spectral linewidth of the laser diodes.

4.1 Organization of the *QD-wave* Laser Simulator

The dynamic laser simulator developed for the purpose of investigating the quantum dot based lasers can be split into three major logi-

cally separate modules: module for calculation of static quantum dot properties, module for actual time evolution of the laser problem and the module for small-signal noise analysis. To minimize the simulation time, computationally demanding module for the time evolution of the laser problem is parallelized for efficient execution using the OpenMP library [36].

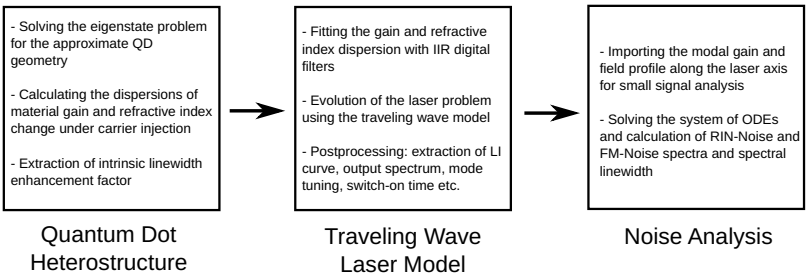

Figure 4.1: Three modules of the *QD-wave* laser simulator with corresponding operations performed within each of them.

- **Quantum Dot Heterostructure** problem consists of the solving of eigenstate problem of the approximate quantum dot geometry and the extraction of steady state parameters of the quantum dot array for varying carrier densities. The extracted parameters include: material gain, refractive index change, linewidth enhancement factor and the carrier inversion factor. After the calculation, extracted parameters are saved for a limited wavelength range in a matrix form, that are forwarded as an input to the traveling wave module performing the time evolution of the laser problem.

- **Traveling Wave Module** Multiple dispersion curves of the material gain and the refractive index change are first imported, together with other relevant parameters. The imported dispersion curves are continuously interpolated during the traveling wave simulation to account for the spatial hole burning effects. The major simulation results after the time evolution include: axial electric field and carrier density profiles, as well as the carrier

density and electric field time traces at both facets. The frequency spectrum, luminescence-current curve and mode tuning can be extracted within the postprocessing step after the DC sweep of the injection current. The time evolution module can also be used with other gain models, i.e. it is not limited to the quantum dot problem for which it was developed. The gain and the refractive index dispersions are approximated with a set of infinite impulse response (IIR) filters while an option for a single Lorentzian IIR gain model is also available in case that the gain dispersion curves of the heterojunction problem are not available.

- **Noise Analysis** is based on the small-signal laser model, and was developed due to the shortcomings of the traveling wave method. Namely, because the direct extraction of the narrow linewidth characteristic of the quantum dot lasers would require impractical simulation time. The module is developed after the work of B. Tromborg et al. [37,38], which was motivated by narrow linewidth observed in external cavity lasers. After the time evolution with the traveling wave model, the module imports the extracted axial carrier density and electric field profiles, from which the spectral linewidth, RIN and FM-noise spectra are calculated.

4.2 Transversal and Axial Problem Separation

The electromagnetic problem of the edge emitting laser is essentially a waveguide problem with resonance along the longitudinal axis, either as Fabry-Pérot resonant cavity or with distributed feedback mirrors. For a laser with the uniform geometry of cross section, the resonating field is generally a superposition of resonating eigenmodes, and can be expressed as a product of its transversal and longitudinal components:

$$\boldsymbol{E}(x,y,z,t) = \boldsymbol{E}_{\perp}(x,y) \cdot \boldsymbol{E}_{\parallel}(z,t), \tag{4.1}$$

which is a basic property of the Helmholtz wave equation that governs the problem:

$$\nabla^2 \boldsymbol{E} + \epsilon(x,y,z) {k_0}^2 \boldsymbol{E} = 0, \tag{4.2}$$

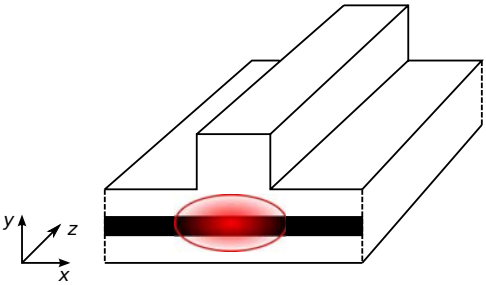

Figure 4.2: Illustration of a Fabry-Pérot edge emitting laser diode.

where ϵ is the permittivity, and k_0 the free space wave number. By relying on the separation of variables, Eq. (4.1), one can derive the wave equation for the transversal problem:

$$\left(\frac{\partial^2}{\partial_x{}^2} + \frac{\partial^2}{\partial_y{}^2}\right) \boldsymbol{E}_{\perp}(x,y) + [\epsilon(x,y){k_0}^2 - \beta^2]\boldsymbol{E}_{\perp}(x,y) = 0, \tag{4.3}$$

where β is the propagation constant. The transversal resonance problem, Eq. (4.3), can be effectively solved numerically. Even though there are analytical approximations available [7], for the problem of ridge waveguide comprising many different materials it is often most accurate approach to use the numerical electromagnetic mode solvers. Numerical electromagnetics as an extensively developed branch of numerical simulations offers many commercial tools for the problem of resonant eigenmodes. For the purpose of this thesis the semiconductor device simulator, *Synopsys Sentaurus Device*[1], was used to determine the properties of the transversal mode.

$$\boldsymbol{E}(x,y,z,t) = \boldsymbol{E}_{\perp}(x,y)\left[F(z,t)e^{i\beta_0 z} + R(z,t)e^{-i\beta_0 z}\right] e^{-i\omega_0 t} \tag{4.4}$$

The problem of axial field propagation is modeled by separating the resonant field into forward and backward propagating waves, $F(z,t)$

[1] www.synopsys.com

and $R(z,t)$, respectively. The problem is effectively adapted to numerical simulation by performing the slowly varying envelope approximation (SVEA), Eq. (4.4), around a reference frequency ω_0, which ultimately yields the traveling wave equations. This allows for great economy of computational resources as the field envelopes, $F(z,t)$ and $R(z,t)$, are slowly varying in both space and time, allowing for more coarse discretization in both space and time.

4.2.1 Transversal Mode Problem

The problem of transversal resonance in terms of cold-cavity approximation, where the refractive index profile describing the ridge waveguide problem is considered to be invariant under the operating conditions of the laser diode.

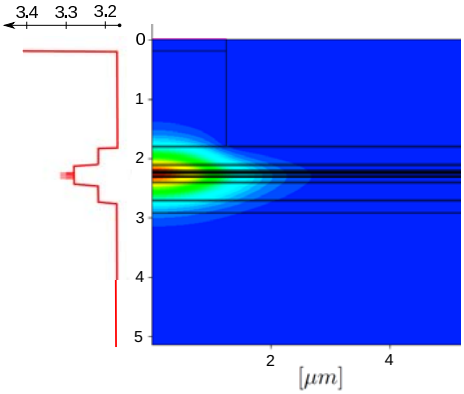

Figure 4.3: Fundamental TE mode intensity profile and refractive index profile of a five-layer quantum dot Fabry-Pérot laser.

Aside from the index variation due to the layered nature of the edge-emitting laser diodes, an appropriate description of refractive index should also consider the variations resulting from periodic grating design, operating conditions and nonuniform geometry along the laser axis:

$$n(x,y,z,\omega) = n_{\perp}(x,y,\omega) + \delta n(x,y,z,\omega). \tag{4.5}$$

By using the cold-cavity approximation however, we essentially neglect the effect of operating conditions on the material properties as well as the longitudinal variation of the refractive index profile, $\delta n(x, y, z, \omega)$, by solving for eigenmodes in a single transversal cross section of the device, thus making it suitable only for isolated sections of the photonic device. For this reason, in case of the multi-section devices the process of determining the mode properties and respective confinement factor should be iterated for each section of the device. By solving for transversal eigenmodes we determine the effective refractive index, n_{eff}, as an eigenvalue, and mode intensity profile as an eigenfunction of the problem. The typical ridge waveguide design is often designed to support only the fundamental mode Fig. (4.3), while generally it can support a multitude of eigenmodes with respective intensity profiles and refractive indices. The main advantage of the ridge design supporting only the fundamental TE_{10} mode, can be seen from the far field profile, Fig. (4.4), which enables superior coupling to concatenating photonic elements. For simplicity we neglect the heating effects that can alter the refractive index profile and cause the mode instability. This problem is unfortunately exacerbated at higher injection currents and output powers, and while not considered within this thesis, it can be potentially included in future work as one of the relevant effects.

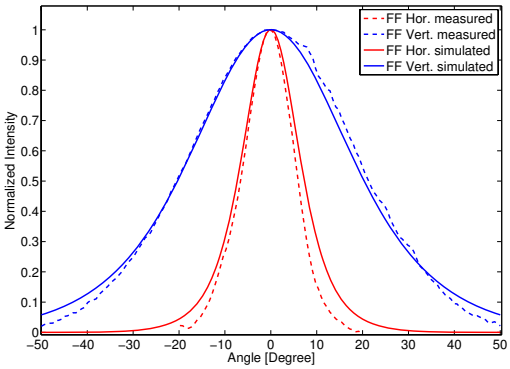

Figure 4.4: Comparison of simulated and measured far field of a 5QD-layer epistructure with 2 μm wide ridge and no grating layer included.

To verify the simulation parameters and accuracy of the numerical model, we rely on the measurements of effective refractive index and far field of the ridge waveguide laser. In essence one could also measure the refractive indices of all semiconductor alloys used during the epitaxial growth that can depend on the technology used as well as the laboratory conditions. However, during the optimization and testing of the laser design, the characterization of individual materials can be considered tedious and inefficient. Having the appropriate technology, the most straight forward approach to qualitatively validate the numerical model would be to measure the far field of the laser diode. The comparison of simulation and measurement results, Fig. (4.4), shows a good agreement with the measurements over a wide span of horizontal and vertical angles for a 5QD-layer epi-structure. The material parameters are instead gathered from different sources containing the analytical models as well as the experimental measurements of refractive indices for the relevant semiconductor compositions [39–42].

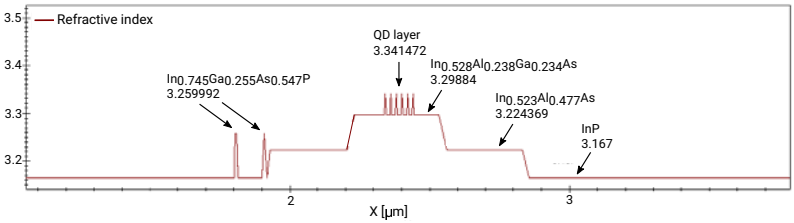

Figure 4.5: Vertical cut of the numerical model showing refractive indices used for the transversal mode problem, starting from ridge on the left down to InP substrate, with included InGaAsP etch-stop layers to define the lateral surface grating.

The full epitaxy structure is depicted in Fig. (4.5), with materials and refractive indices which were used to obtain the numerical results for the transversal problem of Fabry-Pérot ridge waveguide, Figs. (4.3,4.4). The InGaAsP layers can be omitted for the Fabry-Pérot case but we include them in Fig. (4.5), as the same epitaxy is used for the device samples in Ch. 5, to benchmark the *QD-wave* simulation model. In general case the InGaAsP layers can be used to define the lateral DFB grating in order to produce the single-mode emission.

Aside from determining the effective refractive index of the transversal mode, the solution of the transversal mode problem can be used

to extract other important properties useful for subsequent traveling wave simulation, these include the confinement factors of active region:

$$\Gamma_{AR} = \frac{\int_{AR} |\boldsymbol{E}_{\perp}(x,y,\omega)|^2}{\int_{-\infty}^{\infty} |\boldsymbol{E}_{\perp}(x,y,\omega)|^2}, \tag{4.6}$$

and optional distributed feedback grating Fig. (5.1),

$$\Gamma_{DFB} = \frac{\int_{DFB} |\boldsymbol{E}_{\perp}(x,y,\omega)|^2}{\int_{-\infty}^{\infty} |\boldsymbol{E}_{\perp}(x,y,\omega)|^2}. \tag{4.7}$$

The confinement factor of the active region is crucial for the proper modeling of the modal gain and also represents an optimization factor if we want to maximally utilize the active layers of the laser diode. The same can be said for the confinement factor of the grating, which is directly proportional to the coupling coefficient of the distributed feedback grating:

$$\kappa = \kappa(n_1, n_2, \Gamma_{DFB}), \tag{4.8}$$

and together with the refractive indices of alternating grating materials, n_1 and n_2, it determines the coupling strength of the distributed feedback grating, Eq. (4.8). The photonic devices used to benchmark the developed laser model for example, Ch. 5, are all based on lateral surface Bragg gratings that provide the necessary frequency selective feedback [43]. Typical laser diode design often relies on buried feedback gratings to provide the feedback. However, the processing often includes multiple epitaxial growth steps, thus making them costly and complicated to produce. The lateral Bragg grating requires a single epitaxial growth step which simplifies the processing not only by excluding the additional growth steps but also by excluding the intermediate preparation of the surface. The grating design and its properties are studied in greater detail in Ch. 5 with other numerical and experimental results.

4.2.2 Traveling Wave Equations

To make use of the wave equation for electric field, Eq. (2.21), it is necessary to adopt some approximations in order to obtain the traveling wave equations describing the forward and reverse propagating

field envelopes on the longitudinal axis, which are in the end solved numerically. We can start by writing the general wave equation in the frequency domain:

$$\frac{\partial^2 \boldsymbol{E}_{\parallel}}{\partial z^2} + \frac{\omega^2}{c^2}\left[\left(n(\omega) + ik(\omega)\right)^2 + \Delta n^2(\omega, z) + i\frac{\sigma(\omega)}{\epsilon_0 \omega}\right]\boldsymbol{E}_{\parallel} = -\frac{\omega^2}{\epsilon_0 c^2}\Gamma \boldsymbol{P}_{\parallel}, \tag{4.9}$$

where $n(\omega)$ and $k(\omega)$ are the background effective refractive index and extinction coefficient of the lasers waveguide. The major difference compared to the Eq. (2.21), is the inclusion of the confinement factor of the active material, Γ, as the active material in semiconductor lasers often occupies only a fraction of the waveguide, and the refractive index variation through Bragg grating, Δn, which is responsible for the coupling of the forward and reverse propagating wave components. As a consequence of the slowly varying envelope approximation the electric field in frequency domain can be decomposed as:

$$\boldsymbol{E}_{\parallel}(z, \omega) = F(z, \omega)e^{i\beta_0 z} + R(z, \omega)e^{-i\beta_0 z}. \tag{4.10}$$

In general it can be assumed that $k \ll n$, which additionally simplifies our problem and defines the wavenumber as $\beta = \omega n(\omega)/c$. After the substitution of Eq. (4.10) into Eq. (4.9), the problem can be separated for the forward and reverse propagating components as:

$$\frac{\partial F}{\partial z} - i\frac{\beta^2 - {\beta_0}^2}{2{\beta_0}^2}F + \frac{\alpha(\omega)}{2}F - i\kappa_{RF}R = i\frac{\omega^2}{2\beta_0 \epsilon_0 c^2}\Gamma P_F \tag{4.11}$$

$$-\frac{\partial R}{\partial z} - i\frac{\beta^2 - {\beta_0}^2}{2{\beta_0}^2}R + \frac{\alpha(\omega)}{2}R - i\kappa_{FR}F = i\frac{\omega^2}{2\beta_0 \epsilon_0 c^2}\Gamma P_R, \tag{4.12}$$

where the polarization and the coupling of the Bragg grating are averaged over the length Δz, which is longer than the optical wavelength but much smaller than the cavity length:

$$P_{F/R} = \frac{1}{\Delta z}\int_{z-\Delta z/2}^{z+\Delta z/2} P(z, \omega)e^{\mp i\beta_0 z}dz, \tag{4.13}$$

$$\kappa_{RF/FR} = \frac{\omega^2}{c^2}\frac{1}{\Delta z}\int_{z-\Delta z/2}^{z+\Delta z/2}\frac{\Delta n^2}{2\beta_0}e^{\mp i2\beta_0 z}dz. \tag{4.14}$$

Using the coupled-mode theory one can derive a simple expression for the coupling coefficient of the distributed feedback grating [7, 43]:

$$\kappa = \frac{k_0}{2n_{eff}}(n_2^2 - n_1^2)\cdot\Gamma_{DFB}\cdot\frac{\sin(\pi m\gamma)}{\pi m}, \tag{4.15}$$

The equation requires the knowledge of the grating confinement factor, Γ_{DFB}, the effective refractive index of the guided mode n_{eff}, the refractive indices of successive grating materials, n_1 and n_2, order of the grating m, and filling factor of the grating γ. With the buried laser gratings being more represented in commercial designs, it is also common to find in the literature the Eq. (4.15) in simplified form, adapted to buried grating design:

$$\kappa = k_0(n_2 - n_1)\cdot\Gamma_{DFB}\cdot\frac{\sin(\pi m\gamma)}{\pi m}. \tag{4.16}$$

The Eq. (4.16) relies on the fact that in the case of buried gratings the refractive indices of successive grating layers are comparable to the effective index of the transversal mode, i.e. $2\cdot n_{eff} \simeq (n_2 + n_1)$. This of course simplifies the estimation of the coupling coefficient by completely bypassing the need to solve the transversal mode problem numerically. Even though this approach can give satisfying results in the case of buried gratings, it can lead to significant overestimation of the coupling coefficient in case of the lateral grating design [43]. Concerning the internal losses $\alpha(\omega)$, by assuming that the semiconductor loss angle is small, i.e. $\delta_s \simeq \tan\delta_s$, the internal losses can be characterized as $\alpha = \delta_s\beta$, where in terms of the elementary parameters we have:

$$\alpha(\omega) = \frac{2\omega k}{c} + \frac{\sigma}{\epsilon_0 nc} \tag{4.17}$$

Finally, if we approximate the internal losses and coupling coefficient as frequency invariant, i.e. $\alpha = \alpha(\omega_0)$ and $\kappa = \kappa(\omega_0)$ and the wavenumber β with the first two terms of its Taylor expansion, we can

write out the well known traveling wave equations by transforming the Eqs. (4.11,4.12) back into time domain:

$$\left(\frac{1}{v_g}\frac{\partial}{\partial t}+\frac{\partial}{\partial z}\right)F(z,t)=i\frac{\omega_0}{2n\epsilon_0 c}\Gamma P_F(z,t)-\frac{\alpha}{2}F(z,t)+i\kappa_{RF}R(z,t), \tag{4.18}$$

$$\left(\frac{1}{v_g}\frac{\partial}{\partial t}-\frac{\partial}{\partial z}\right)R(z,t)=i\frac{\omega_0}{2n\epsilon_0 c}\Gamma P_R(z,t)-\frac{\alpha}{2}R(z,t)+i\kappa_{FR}F(z,t). \tag{4.19}$$

As we have derived the traveling wave equations from the semi-classical wave equation, Eq.(4.9), the contribution of the spontaneous emission noise is still not included in Eqs. (4.18,4.19). By adding the noise terms and expressing the material polarization in terms of net modal gain and detuning factor, $(g-i\delta)$, the traveling wave equations that we implement numerically can be expressed as:

$$\left(\frac{1}{v_g}\frac{\partial}{\partial t}+\frac{\partial}{\partial z}\right)F(z,t)=(g-i\delta)F(z,t)+i\kappa_{RF}R(z,t)+F_{sp}(z,t), \tag{4.20}$$

$$\left(\frac{1}{v_g}\frac{\partial}{\partial t}-\frac{\partial}{\partial z}\right)R(z,t)=(g-i\delta)R(z,t)+i\kappa_{FR}F(z,t)+F_{sp}(z,t). \tag{4.21}$$

The modeling of laser diodes in time domain via advection equations initially popularized by J.E. Carroll et al. [35], just like real semiconductor lasers is based on spatially and temporally varying spontaneous emission noise, $F_{sp}(z,t)$, as a driving force which enables the coherent lasing in active laser medium. The left hand side of both equations, Eq. (4.20) and Eq. (4.21), represents a standard hyperbolic advection equation while the right hand side contains all the sources and sinks in a finite volume of laser cavity. The amplified and detuned electrical field, $(g-i\delta)F(z,t)$, the field coupled via gain and/or refractive index grating, $i\kappa_{RF}R(z,t)$, and Langevin forcing term for spontaneous emission noise, $F_{sp}(z,t)$.

The dispersion of gain factor, $(g - i\delta)F(z,t)$, is not intrinsically included in the traveling wave model as the advection equations are described in time domain. Nevertheless, with the help of digital filter theory it is possible to form satisfactory digital filter models for dispersion of modal gain, g, and detuning factor, $i\delta$, which are often available in frequency domain. Successful realizations of this approach can be also found in some commercial laser diode simulators [2]. Following the solution of transversal mode problem, the coupling coefficients, κ_{RF} and κ_{FR}, can be easily estimated while the forcing term for the spontaneous emission noise, $F_{sp}(z,t)$, is included in the framework of the Langevin dynamics, to account for the microscopic degrees of freedom which are often neglected in traditional rate equation models.

Much like standard coupled photon and carrier rate equations, the advection equations are coupled with carrier rate equation, based on the ABC recombination model, which in its simplest form reads:

$$\frac{dN_0}{dt} = \frac{\eta_i\, I_{inj}}{q\, V_{act}} - (A \cdot N_0 + B \cdot {N_0}^2 + C \cdot {N_0}^3) - \frac{v_g\, g_{mat}\, P}{1 + \epsilon\, P} + F_N(z,t), \quad (4.22)$$

where g_{mat} is the material gain, ϵ the nonlinear gain saturation coefficient, P the photon density and $F_N(z,t)$, the Langevin noise term for carrier noise. In this way we are also able to extract the characteristic laser parameters, light-current dependence and time evolution of both photon and carrier density. However, unlike the standard rate equation approach, the traveling wave approach intrinsically includes the spatial hole burning effects as well the spatial variation of characteristic laser parameters. It should be noted that the carrier density $N_0(z,t)$, does not include the formation of carrier grating at this point.

$$\frac{dN_0}{dt} = \frac{\eta_i\, I_{inj}}{q\, V_{act}} - (A \cdot N_0 + B \cdot {N_0}^2 + C \cdot {N_0}^3) - \frac{1}{V_{act}} \frac{dP_{\#}}{dt}\bigg|_{stim} + F_N(z,t), \quad (4.23)$$

The Eq. (4.22), can be often found in literature and is quite good at describing the forces that drive the rate equations of a typical semiconductor laser, as well as for the estimation of basic device characteristics.

[2] www.photond.com

The problem here is that we do not know beforehand the value of the material gain at the lasing frequency, $g_{mat}(N, \lambda)$, as it is also not possible to determine the lasing wavelength, λ, before having an actual time sample of the output electric field. To this end we resort to tried solution, Eq. (4.23), which has been realized in a commercial traveling wave laser simulator [14]. The difference between the Eq. (4.22) and Eq. (4.23), which we actually implement numerically, is the description of the stimulated emission contribution to carrier population. In Eq. (4.23), the rate of stimulated emission $dP_{\#}/dt$, can be simply determined from the net photon flux through a discretization element during the simulation.

By using the free carrier rate equation, Eq. (4.22), to describe the evolution of carrier density along laser axis, we stay consistent with the quantum dot gain model Ch. 2. However, to describe the carrier dynamics within quantum dots a multi-population carrier rate equation model can be considered more appropriate [44, 45]:

$$\begin{aligned}
\frac{dN_{ES}}{dt} &= \frac{I_{inj}}{q} + N_{GS}\rho_{ES}\frac{1}{\tau_{GS}^{ES}} - N_{ES}\rho_{GS}\frac{1}{\tau_{ES}^{GS}} - N_{ES}(1-\rho_{ES})\frac{1}{\tau_{sp}^{ES}} \\
&\quad - N_{ES}\frac{1}{\tau_{esc}} - v_g\Gamma g_{ES}P \\
\frac{dN_{GS}}{dt} &= N_{ES}\rho_{GS}\frac{1}{\tau_{ES}^{GS}} - N_{GS}\rho_{ES}\frac{1}{\tau_{GS}^{ES}} - N_{GS}(1-\rho_{GS})\frac{1}{\tau_{sp}^{GS}} - v_g\Gamma g_{GS}P \\
\frac{dP}{dt} &= v_g\Gamma g_{GS}P + v_g\Gamma g_{ES}P - \frac{P}{\tau_{ph}} + \beta_{sp}\frac{N_{GS}}{\tau_{sp}^{GS}} - \beta_{sp}\frac{N_{ES}}{\tau_{sp}^{ES}}
\end{aligned} \tag{4.24}$$

The coupled multi-population Eqs. (4.24) describe the evolution of carrier and photon density in a two-level quantum dot system, although an additional carrier population can be added for quantum dot wetting layer, this approach already requires knowledge of numerous parameters that are often not easy to estimate accurately. The parameters characteristic of Eqs. (4.24) are: $\rho_{ES(GS)}$, probability of finding a free state at elevated (ground state) energy, $\tau_{ES(GS)}^{GS(ES)}$, transition times from elevated state to ground state and vice versa and $g_{ES(GS)}$, the material gain for carriers in elevated and ground states respectively. The advantage of multi-population equations in our case would be

the self-consistent inclusion of different energy levels, which can be advantageous for the application of implemented linewidth enhancement factor model at higher injection currents Ch. 2 [34]. However, due to the numerous parameters required by the multi-population rate equation model we rely on the ABC recombination approach for the modeling of carrier evolution, Eq. (4.23).

Additionally the spectral analysis of time evolved laser output and small-signal analysis can enable further insight into characteristics of specific laser design, through side-mode suppression ratio, spectral linewidth, amplitude modulation (AM) and frequency modulation (FM) responses as well as the characteristics of noise spectra. The most common approach to determine the AM and FM responses relies on linearization of hyperbolic partial differential equations that describe the advection of the electric field envelope. This is well documented in series of publication regarding the CLADISS simulation software [46], as well as the matrix based estimation of the spectral linewidth, applicable to both broad and narrow spectral linewidth. Another possibility for estimation of the spectral linewidth and the RIN and FM-Noise spectra that is actually implemented in the simulator discussed in this thesis, is a small-signal model based on Green's function solution [38]. The main advantage of this model is efficiency, as it is not necessary to evolve the laser problem in time with linearized equations just for the modulation responses. The model solves instead a system of 4 equations derived from small-signal analysis, directly from the carrier density and electrical field profiles retrieved from the traveling wave model.

4.2.3 Formation of the Carrier Grating Pattern

In the case of narrow-bandwith counterpropagating waves, the formation of standing wave pattern that occurs as a superposition of the forward and reverse propagating components of the resonating field, can lead to the formation of the carrier grating pattern along the laser cavity. As we are concerned mostly with single-mode lasers, it is appropriate to consider its effects on the linewidth and mode stability. The mechanism that is most relevant for spectral linewidth, is the effect of such half-wavelength carrier density fluctuation on modal gain profile, leading to modal selectivity through gain variation at the same

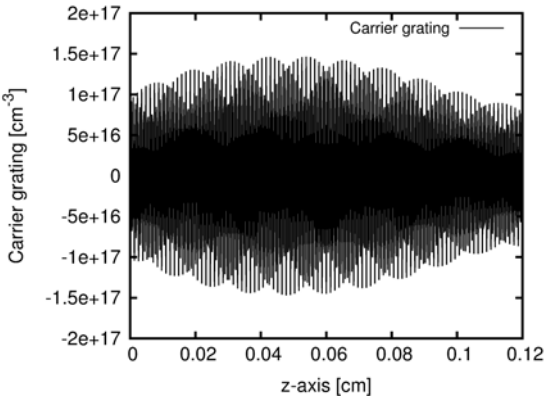

Figure 4.6: Calculated carrier grating component of a 2QD-layer single-mode DFB laser.

spatial frequency. The resulting gain saturation occurs predominantly at anti-nodes of the resulting field intensity pattern, and is correlated with the main lasing mode. As a consequence, such a scenario can only further decrease the stability of the lasing mode at higher output powers, where the effects of self-heating and overall carrier depletion are also prominent.

$$\begin{aligned} \frac{dN_{2F}}{dt} &= -(R_{sp}{}'(N_0) + 4D_{ap}{\beta_0}^2)N_{2F} - is(P_F\,R^* - F\,{P_R}^*) \\ \frac{dN_{2R}}{dt} &= -(R_{sp}{}'(N_0) + 4D_{ap}{\beta_0}^2)N_{2R} - is(P_R\,F^* - R\,{P_F}^*) \end{aligned} \tag{4.25}$$

To model such an effect numerically we resort to approach implemented in the *FreeTWM* software [47]. The effect can be optionally included in the laser simulation, in which case two additional rate equations have to be integrated in time, Eqs. (4.25), resulting in spatial profiles of forward, N_{2F}, and reverse, N_{2R}, components forming the carrier grating pattern. The total carrier density, $N(z,t)$, is then also modified accordingly, comprising in this case both the carrier density calculated initially, $N_0(z,t)$, using the Eq. (4.23), as well as the carrier grating pattern:

$$N(z,t) = N_0(z,t) + \mathbb{R}\left[N_{2F}(z,t)\, e^{i2\beta_0 z} + N_{2R}(z,t)\, e^{-i2\beta_0 z}\right] \qquad (4.26)$$

The additional parameters that we introduce this way are: derivative of spontaneous emission rate, $R_{sp}{}'(N_0) = dR_{sp}/dN_0$, ambipolar diffusion coefficient, D_{ap}, wave vector at reference wavelength, β_0, scaling factor, s, and polarization components $P_{F,R}$. The polarization components are scaled, where relations, $-\mathbb{I}\left[P_F/F\right]$ and $\mathbb{R}\left[P_F/F\right]$, yield modal gain and detuning factors. The same relations can be also written for counterpropagating wave, R.

As we are generally interested in the single-mode laser operation, it is not necessary to consider the broadband polarization components, $P_{F,R}$. For simplicity we therefore adopt the linear approximation for polarization, having an amplitude determined by the spatially varying gain value at the lasing frequency. An example of the calculated carrier grating component of the carrier density profile, Fig. (4.6), shows a relatively low contribution to overall carrier density, i.e. one to two orders of magnitude lower than a typical mean carrier density. The spatial frequency of such a carrier grating pattern is determined by the wave vector, β_0, at the reference wavelength of the SVEA approximation.

4.3 Modeling of Photon and Carrier Noise

The photon and carrier noise sources in traveling wave equations are included to model the microscopic degrees of freedom which are neglected under the continuum approach of material properties description. This way it is possible to combine the benefits of both the continuum model and statistical nature of noise sources that predominantly determines the spectral linewidth that we are interested in. Here we briefly summarize the the theory behind the noise models and numerical implementation of the algorithms used to include the noise in traveling wave laser model.

4.3.1 Langevin dynamics

The differential equations describing the traveling wave model, Eqs. (4.20,4.21,4.22), are essentially stochastic differential equations based

on the Langevin dynamics with driving terms denoted as: F_S and F_N, corresponding to spontaneous emission noise and carrier noise sources respectively. By assuming the particle nature for both the photons and electrons, the noise in both cases can be described as shot noise. As a consequence, the spectral densities can be shown to be constant and proportional to the average rate of particle flow through the photon or carrier populations:

$$\begin{aligned} \langle F_i F_i \rangle &= \sum R_i^+ + \sum R_i^-, \\ \langle F_i F_j \rangle &= -\Big[\sum R_{ij} + \sum R_{ji} \Big], \end{aligned} \tag{4.27}$$

where R_i^+ and R_i^- represent the rates of flow in and out of the population i, and R_{ij} the rate between the population i and j. By considering all the sinks and sources for the photon and carrier populations, one can derive the correlation strengths for the noise [7]:

$$\begin{aligned} \langle F_P F_P \rangle &= 2\Gamma R'_{sp} N_p, \\ \langle F_N F_N \rangle &= 2R'_{sp} N_p/\Gamma - v_g g N_p/V_c + \eta_i (I_{inj} + I_{th})/q{V_c}^2, \\ \langle F_P F_N \rangle &= -2R'_{sp} N_p + v_g g N_p/V_p. \end{aligned} \tag{4.28}$$

The Langevin noise being defined in this sense, is a stationary process where the correlation strengths, following from the Wiener-Khinchin theorem, correspond to noise spectral density. The carrier noise can be then directly plugged into the carrier rate equation, Eq. (4.22). In the case of photon noise however, the photon noise correlation strength has to be related to the traveling wave Eqs. (4.20,4.21), representing the resonating laser field. This problem is also somewhat simplified by assuming that the resonating field is confined within the fundamental TE_{10} mode. The transmitted power, P_T, and total energy density per unit length, W', of a TE_{10} mode are calculated as:

$$P_T = \frac{1}{4\eta_{TE}} |E_0|^2 ab, \tag{4.29}$$

$$W' = {W_e}' + {W_m}' = \frac{1}{4}\epsilon |E_0|^2 ab. \tag{4.30}$$

The η_{TE} and ϵ, represent the wave impedance and permittivity, $W_e^{'}$ and $W_m^{'}$, the energy densities of electric and magnetic field per unit length, and a and b, the effective width and height of the waveguide. The energy density can be now directly related to photon correlation strength and used with traveling wave equations, Eqs. (4.20, 4.21). To numerically generate the complex vector of the spontaneous emission noise, F_s, and real-valued carrier noise, F_N, we use the Box-Muller transform which transforms the uniformly distributed random number to a pair of independent normally distributed random number [48]. This approach is particularly convenient as the spontaneous emission noise is described in complex vector space, and concerning the realization as a C++ algorithm, it also does not require any proprietary library. As an output of the traveling wave simulation we get the electric field strength, E_0, as profiles along the axis of the photonic device. However, to characterize a laser device the Light-Current (LI) curve is often used as a figure of merit, often measured in mW output power, here the Eq. (4.29), can be also useful to make more practical sense of the traveling wave model results.

4.3.2 Inclusion of Colored Carrier Noise

The colored noise occurs naturally in many physical and biological systems and semiconductor lasers are no exception. In semiconductor lasers the colored noise component of the carrier noise is often described as $1/f$ noise, also known as pink noise. On the other hand, the reality can be often more complex where the contribution of other colored noise types can be noticed in the measurements of the frequency noise spectra as well [49, 50]. The occurrence of colored noise in semiconductors is not only determined by the device design but also by the power source as well, which is not very surprising, as it essentially acts as an interface of the laser diode system and introduces the fluctuations in carrier population originating outside of the isolated laser diode system.

In modern optical communication systems we are often interested in high bit rates, where the contribution of the technical $1/f$ noise to phase error variance is not dominant [49]. Therefore, the experimental results often focus on the intrinsic linewidth generated by the Gaussian noise sources. The two experimental approaches commonly used in

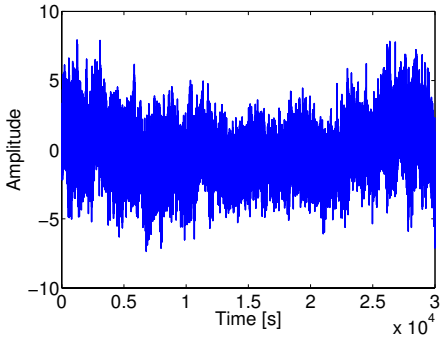

Figure 4.7: Time sample of generated $1/f$ noise with time step of 1 s.

practice to extract the spectral linewidth, either from beat note signal or from frequency noise spectra, usually try to neglect the effect of colored noise. Due to the presence of various noise sources with different spectral characteristics on the other hand, makes the isolation of the Gaussian noise contribution less than a straightforward task [49, 50].

The reason for including the colored noise sources in the laser model, Fig. (4.7), is mainly for studying its effect on the mode stability and potential deterioration of the intrinsic spectral linewidth through degraded mode stability or emergence of longitudinal side modes. There are both experimental and theoretical studies related to colored noise and mode instability in laser diodes [33, 51]. The experimental results show that the origin of linewidth floor may well lie in the presence of technical colored noise, while the theoretical study in [51], shows that the axial photon fluctuations can lead to linewidth rebroadening that is also commonly observed in experimental measurements of the linewidth.

Given the nature of the $1/f$ noise, i.e. the correlation of the noise samples along the laser diode, we can study its impact on mode stability through correlated change in the refractive index or direct coupling of the correlated carrier noise to resonant field and investigate whether the colored technical noise can result in the axial photon fluctuation and mode instability that have been studied previously in theory [51].

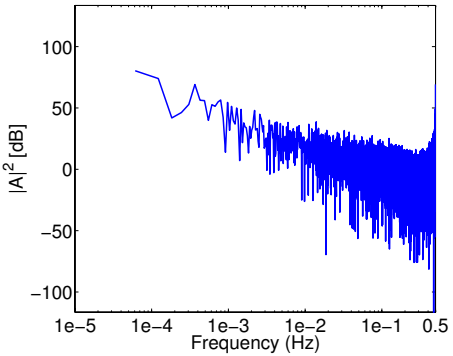

Figure 4.8: Power spectrum of generated $1/f$ noise with time step of 1 s.

$$\frac{dN}{dt} = \frac{\eta_i\, I_{inj}}{q\, V_{act}} - (A \cdot N + B \cdot N^2 + C \cdot N^3) - \frac{v_g\, g_{mat}\, P}{1 + \epsilon\, P} + (1 - \xi) \cdot F_N(z,t) + \xi \cdot F_{CN}(z,t), \tag{4.31}$$

The colored carrier noise can be optionally included as an addition to Gaussian noise by defining the factor ξ, in the carrier rate equation Eq. (4.31). The colored noise relies on the frequency domain, multiplication method (FIR technique), the code used to generate the colored noise is given in [52], that is not strictly limited to $1/f$ pink noise, Fig. (4.8) . It is generally able to simulate any noise with spectral characteristic of the form $1/f^{\alpha}$. By default, the carrier noise is assumed as Gaussian in the carrier noise while the colored noise is calculated only optionally as the colored noise generation at each spatial discretization can be time-consuming even though it is coded in C++. Colored noise is generated before the actual laser simulation, in a spatio-temporal matrix, covering complete spatial and temporal samples. To reduce the simulation time in case of the sweeping current simulations, the colored noise matrix is simply reused for all the injection current variations for which the sweeping simulation is executed.

4.4 Spatiotemporal Discretization

To adapt the traveling wave model to numerical computation the discretization of the computation domain is necessary. As we are dealing with time-domain model described by hyperbolic differential equations, Eqs. (4.20,4.21), to ensure the stability of the numerical algorithm we resort to Courant−Friedrichs−Lewy (CFL) condition, $v_g = \Delta z/\Delta t$, relating the spatial, Δz, and time step, Δt, over the group velocity, v_g. For convenience we initially define the time step, Δt, as the sampling theorem limits the spectral sample that we can cover with a given time step. For a time step, Δt, the spectral sample of laser output would be limited by the Nyquist frequency:

$$-f_N < f < f_N, \tag{4.32}$$

where the Nyquist frequency, f_N, is directly related to the time step, $f_N = \frac{1}{2\cdot\Delta t}$. As a consequence of the predetermined time step, the spatial step subsequently follows from the CFL condition. One easing fact is that in the case of Bragg grating sections the coupling coefficient is considered uniform for a considered device section, which makes it unnecessary to discretize the device on the scale of Bragg grating geometry.

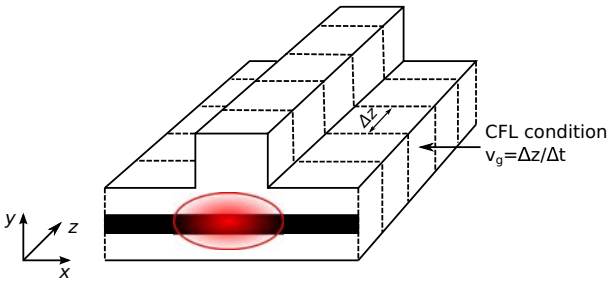

Figure 4.9: Illustration of spatial discretization of a laser diode with Courant-Friedrichs-Lewy (CFL) condition which determines the step size along along z and t axes.

For this reason the CFL condition is the sole governing factor when it comes to discretization, Fig.(4.9), while precaution should be taken

only in the case of multi-section devices with varying effective refractive index. The varying effective index consequently leads to varying spatial step size from section to section in order to maintain the CFL criterion.

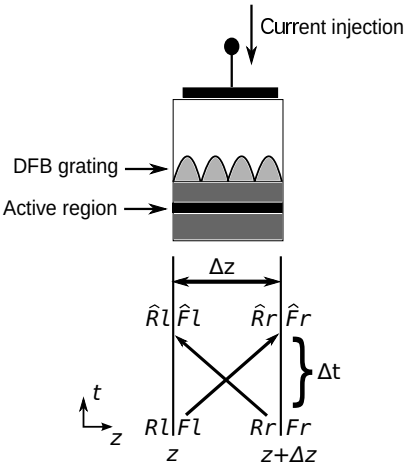

Figure 4.10: Discretization element of a laser section with illustrated evolution of the forward, F, and reverse, R, propagating electric field over a single time step along z and t axes.

As a consequence of such discretization, each section of the simulated photonic integrated circuit (PIC) is divided into elements of uniform length, Fig. (4.10). Numerically these elements are realized as structured data elements, each containing the forward and reverse traveling wave at its left and right end as well as the carrier density that is considered uniform across an individual element. Aside from the time-dependent variables each element also contains all the relevant parameters necessary to evolve all the time-dependent variables in time, which includes the geometry, material related parameters and injection current. This way it is quite easy to vary all the parameters from section to section, like current injection or modulation, coupling coefficient or parameters of the material gain model.

Numerically, a single pass from first to last discretization element, i.e. update of the time dependent variables over a single time step,

Δt, corresponds to one round trip of the internal electrical field of the simulated PIC device. The forward and reverse propagating field envelopes, $F_{l,r}$ and $R_{l,r}$, are propagated across an element by being passed through a digital filter whose parameters are set to emulate the gain characteristics of the active region.

4.5 Numerical Material Gain Models

The traveling wave laser model in it's basic form, Eqs. (4.20,4.21), does not offer the possibility of modal gain dispersion. In other words, all the cavity modes are treated with uniform gain dispersion function in frequency domain. To complement the classical advection equations we resort to the theory of infinite impulse response (IIR) digital filters to emulate the gain and refractive index dispersion of the active region of the simulated photonic device. The *QD-wave* simulation model includes two options to realize this, single pseudo-Lorentzian gain model that is classically employed [14,35], and a multi-Lorentzian gain model which seeks to fit the precalculated gain dispersions, Ch. 2, on a finite wavelength range by using a set of superimposed pseudo-Lorentzian filters. The gain filters are implemented in time domain in the form of linear constant-coefficient difference equation, which essentially represents the Fourier transform of the desired gain filter transfer function in frequency domain, $H(\omega)$.

4.5.1 Single-Lorentzian Gain Model

When we think of semiconductor material gain, the Lorentzian gain dispersion is certainly not the first option that comes to mind. For description of gain dispersion of bulk or quantum well or dot based devices, the Gaussian gain dispersion often offers a better fit. However, considering that our time-domain PIC device simulation model is CPU intensive, among our top priorities is also a simplicity of implementation of gain dispersion in time domain. The pseudo-Lorentzian gain dispersion implemented as digital IIR filter leads to a fairly simple time-stepping equations, Eqs.(4.33,4.34), for forward, $F(z+\Delta z,t)$, and reverse, $R(z,t)$, propagating filed, where we use the notation from Fig. (4.10), for the reference:

$$\begin{aligned} F(z+\Delta z,t) = {} & m_{11}(m_a F(z,t-\Delta t) + m_b F(z,t-2\Delta t)) \\ & + m_{12}(m_a R(z,t-\Delta t) + m_b R(z,t-2\Delta t)) \\ & - m_c F(z+\Delta z,t-\Delta t), \end{aligned} \tag{4.33}$$

$$\begin{aligned} R(z,t) = {} & m_{21}(m_a F(z+\Delta z,t-\Delta t) + m_b F(z+\Delta z,t-2\Delta t)) \\ & + m_{22}(m_a R(z+\Delta z,t-\Delta t) + m_b R(z+\Delta z,t-2\Delta t)) \\ & - m_c R(z,t-\Delta t). \end{aligned} \tag{4.34}$$

This simple model requires only a memory of two last time steps for the whole mesh, which reduces the memory requirements. The gain filter in this case is described fully with its three coefficients:

$$\begin{aligned} m_a &= (1+K+0.5\cdot g_{pk}\cdot\Delta z)/(1+K-0.5\cdot g_{pk}\cdot\Delta z), \\ m_b &= e^{i\theta}(1-K+0.5\cdot g_{pk}\cdot\Delta z)/(1+K-0.5\cdot g_{pk}\cdot\Delta z), \\ m_c &= e^{i\theta}(1-K-0.5\cdot g_{pk}\cdot\Delta z)/(1+K-0.5\cdot g_{pk}\cdot\Delta z). \end{aligned} \tag{4.35}$$

The coefficients K, g_{pk} and θ respectively define the FWHM of the gain curve, peak gain depending on the carrier density and detuning of the gain peak from the reference frequency of the traveling wave model. In the case of devices with distributed feedback, like DFB or DBR lasers we also need to define the $m_{i,j}$ matrix coefficients defining the distributed feedback grating:

$$M_c = \begin{bmatrix} m_{11} & m_{12} \\ m_{21} & m_{22} \end{bmatrix}, \tag{4.36}$$

related to the coupling coefficients κ_{FR} and κ_{FR} as:

$$\begin{aligned} m_{11} &= \sqrt{1-|m_{12}|^2}, \\ m_{12} &= i\kappa_{RF}\Delta z, \\ m_{21} &= i\kappa_{FR}\Delta z, \\ m_{22} &= \sqrt{1-|m_{21}|^2}. \end{aligned} \tag{4.37}$$

The gain peak g_{pk}, depending on carrier density N, which varies both spatially and temporally for given spatial element, Fig. (4.10), is simply defined as:

$$g_{pk} = \frac{dg/dN(N - N_{tr})}{1 + \epsilon P}, \tag{4.38}$$

where N_{tr} and P are transparency carrier density and photon density, respectively. The denominator is acting as a model for gain suppression, where ϵ is a nonlinear gain saturation coefficient. The main advantage of the single-Lorentzian gain model is its simplicity, which allows for great reduction of simulation time as the gain parameters are updated not only at each time step but also for each discretization element. The cost of simplicity is paid mainly in terms of inaccurate gain dispersion and gain peak calculation, Eq. (4.38), which does not include the saturation of the differential gain, dg/dN, at higher carrier densities which naturally occurs for all active materials. Nevertheless, this simple gain model can be used with any device supported by the simulator: Fabry-Pérot laser, DFB/DBR laser, SOA or integrated devices. The best results can be expected for applications where the accurate description of gain dispersion is not critical, like in the case of DFB or DBR lasers where the lasing mode is often near the gain peak.

Within the single-Lorentzian gain model, we also add an optional inclusion of the Lorentzian or frequency invariant absorption for modeling the interaction of the resonating field with external absorption sources. Such a model could be used to describe the presence of liquid or gases with absorption lines near the lasing frequency, acting on the internal resonating field of the device [53]. The absorption in such a modified gain model is implemented as carrier density invariant, i.e. acting with a fixed preset absorption peak as a substitute for the Eq. (4.38).

4.5.2 Multi-Lorentzian Gain Model

To essentially make use of the precalculated gain and refractive index dispersions Ch. 3, a more complex digital filter is necessary to replicate the quantum dot material properties using the traveling wave model.

To model only the saturation of the differential gain at higher carrier densities, it is enough to use the single-Lorentzian filter centered around quantum dot ground state, while replacing the equation for gain peak, Eq. (4.38), with extracted gain model data.

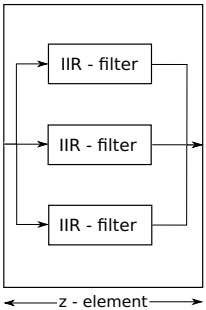

Figure 4.11: Illustration of multi-Lorentzian gain filter on a single discretization element with parallel arrangement of digital IIR filters.

However, to implement accurately the dispersions of both gain and refractive index on a broader frequency range, we implement a multi-Lorentzian gain filter as an additional gain modeling option. The Lorentzian IIR filters are superimposed to fit the calculated dispersions on a broader wavelength range [31, 45], where the full width at half maximum (FWHM) of individual Lorentzian filters is naturally significantly smaller than for the case of single-Lorentzian gain model where it fits the whole considered wavelength span of the gain spectrum.

The gain dispersion calculation described in Ch. 3, includes the gain contribution of the ground state and two elevated carrier transitions. However, it is not always necessary for the gain model to replicate the whole calculated gain dispersion. This particularly holds for the narrow-band designs investigated in this thesis, where the side-modes are suppressed by the DFB/DBR gratings. In this case the gain properties around the Bragg wavelength are the most relevant. Before the actual time-domain simulation the calculation of the gain and refractive index dispersion is performed for multitude of injection currents in the software module solving the quantum dot heterostructure problem, producing eventually the gain dispersion curves for different

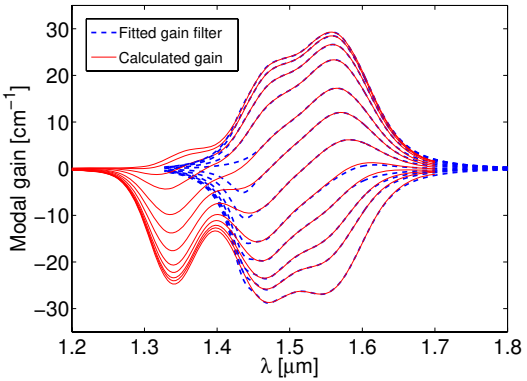

Figure 4.12: Calculated gain dispersion of a 2QD-layer epitaxy and multi-Lorentzian gain model comprising 29 parallel Lorentzian filters fitted for various injection rates.

carrier densities ranging from sub-transparency to maximal gain values. From the calculated gain dispersion Fig. (4.12), it can be seen that the ground state and the first elevated state transitions contribute the most to lasing. The 29 parallel Lorentzian are shown to be sufficient to adequately replicate the dispersion of the first two transitions, Fig. (4.12).

During the simulation, with each time step and for each discretization element the carrier density is updated according to carrier rate equation, Eq. (4.23). At each of these instances, using the interpolation of dispersion curves, the material gain is updated accordingly. Naturally, due to the dispersion of individual Lorentzian gain filters, Fig. (4.11), that build up the multi-Lorentzian gain model all have different parameters for the gain and detuning factor. However, to obtain a satisfactory fit of the material gain filter, when determining the parameters of the individual filters we need to factor in the contribution of the neighbouring filters, as the final numerical dispersion is obtained by their superposition. The filter parameters are determined through an iterative algorithm for each of the considered injection rates, as the contribution of the neighbouring filters varies depending on the

change in the dispersion with injection rate. The numerical equations of individual Lorentzian filters are essentially the same as for single-Lorentzian gain model, Eqs. (4.33,4.34), with individual filters being now placed uniformly on the wavelength span of gain dispersion that we want to fit.

4.6 Treatment of Interfaces

In a case of multi-section device it is possible that the individual sections are either processed differently or are grown in sequential deposition steps, resulting in discontinuities of the effective refractive index along the device. To adequately model these differences, we need to take into account the field reflections that occur at interfaces between the sections.

$$\begin{aligned} F_B(t) &= t_A \cdot F_A(t) + r_B \cdot R_B(t) + Y_A(t), \\ R_A(t) &= r_A \cdot F_A(t) + t_B \cdot R_B(t) + Y_B(t) \end{aligned} \tag{4.39}$$

Following the simplified fundamental mode description of resonance in transversal plane, consequently the interfaces between the section are also treated in a simplified manner, considering only the reflection and transmission coefficients for the fundamental TE_{10} mode.

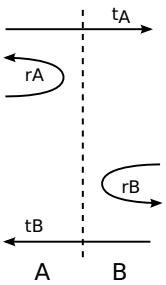

Figure 4.13: Illustration of reflection and transmission at the interface between sections A and B with corresponding field coefficients.

Using the Fresnel field equations describing a simple dielectric interface one can derive the equations for forward and reverse propagating

field envelopes, Eqs. (4.39). The $r_{A/B}$ and $t_{A/B}$ are field reflection and transmission coefficients, respectively, looking from A or B side of the interface, Fig. (4.13). The possibility of field injection is also included in the model through factors Y_A and Y_B, for the simulation of devices with external field input, such as semiconductor optical amplifiers (SOA). The field injection is generally considered to be zero between the sections, while it can be optionally defined only at the facets of the device. The inclusion of phase shifts along the cavity is treated in a similar manner, the phase shift can be added to facets to emulate the irregularly cleaved DFB gratings while it is neglected at the interfaces between the sections. The phase shifts along the DFB sections which can be found in many commercial designs, can be also added to further control the output spectrum.

4.7 Small-Signal Analysis

The traveling wave model itself allows us already to extract many of the critical properties of laser performance like: LI-curve, side-mode suppression ratio and even the spectral linewidth. However, we will show that the direct extraction of the spectral linewidth from the simulated time trace of the field at the device facets also has its limitation. Consequently, we will give here a more detailed motivation for the small-signal laser model implemented in the *QD-wave* simulator. Moreover, the model equations will be discussed as well, together with the approach to numerical implementation.

4.7.1 Small-Signal Model Motivation

Even though the direct extraction of linewidth from the traveling wave simulation is possible with the help of fast Fourier transform (FFT), in order to extract the spectral linewidth necessary for modern optical signal modulations [4], of below 1 MHz the simulation time would be simply impractical. To demonstrate this we can start from the simulation time step of $\Delta t = 1.5 \cdot 10^{-14}$ s, which is necessary in order to cover the ground state and the first elevated state of the quantum dot gain dispersion as in Fig. (4.12), by the fitted numerical gain

model. This equates to the sampling frequency of $f_s = 66.66$THz, and in order to extract the linewidth of 100 kHz we would require at least:

$$N_{bins} = \frac{f_s}{2 \cdot 100 \text{ kHz}} = 333.3 \cdot 10^6, \tag{4.40}$$

frequency bins of the Fourier transform to reach the sufficient frequency resolution. Meaning that we would need at least:

$$N_{sample} = 2 \cdot N_{bins} = 666.6 \cdot 10^6, \tag{4.41}$$

time samples/steps to extract the linewidth of 100 kHz, which would result in days of simulation time, just to calculate the linewidth for a single injection current. Instead of this we resort to an alternative approach for the calculation of spectral linewidth, which only requires the traveling wave simulation to reach a steady state. The model that we implement relies on the spatially resolved small-signal theory [37], developed initially to address the narrow spectral linewidth lasers as well the complex effects arising from the spatial variation of model parameters, which is a clear advantage compared to classical Schawlow-Townes linewidth equation.

4.7.2 Small-Signal Equations and Numerical Modeling Approach

The small-signal model is directly dependent on the output results of the traveling wave simulation, where the longitudinal profiles of the model variables and parameters are taken as input. In short, the derivation of small-signal equations is based on separation of the traveling wave field envelopes, F and R, as in Eqs. (4.20, 4.21), into their amplitude and phase components:

$$F = |F| \cdot e^{j\phi_F}, \tag{4.42}$$

$$R = |R| \cdot e^{j\phi_R}. \tag{4.43}$$

This allows one to derive small-signal equations by substituting the small-signal deviations of the field amplitude, phase and carrier density into the equations describing the traveling wave model Eqs. (4.20, 4.21,

4.23). If we denote the traveling wave envelopes, Eqs. (4.42,4.43), as $u^{\pm} = a^{\pm} \cdot e^{j\phi^{\pm}}$ and by assuming a purely real coupling coefficient κ, the small-signal equations can be expressed as:

$$\frac{1}{v_g}\frac{\partial}{\partial t}\left(\frac{\delta a^{\pm}}{a_s{}^{\pm}} + j\delta\phi^{\pm}\right) = -j\delta k \mp \frac{\partial}{\partial z}\left(\frac{\delta a^{\pm}}{a_s{}^{\pm}} + j\delta\phi^{\pm}\right) + j\kappa v^{\pm}\left(\frac{\delta a^{\pm}}{a_s{}^{\pm}} - \frac{\delta a^{\mp}}{a_s{}^{\mp}} + j(\delta\phi^{\pm} - \delta\phi^{\mp})\right) + \frac{F_{sp}{}^{\pm}}{u_s{}^{\pm}} \tag{4.44}$$

$$\frac{\partial}{\partial t}\delta N = \delta J - \frac{\delta N}{\tau_R} - 2\frac{\partial R_{st}}{\partial P}\left(P_s{}^{+}\frac{\delta a^{+}}{a_s{}^{+}} + P_s{}^{-}\frac{\delta a^{-}}{a_s{}^{-}}\right) + F_N \tag{4.45}$$

where $v^{\pm} = e^{\mp j\phi_g} \cdot (u^{\mp}/u_s{}^{\pm})$, $P_s = P_s{}^{+} + P_s{}^{-}$ the steady-state photon density, $u_s{}^{\pm} = a_s{}^{\pm} \cdot e^{j\phi_s{}^{\pm}}$ the steady state envelope solution, ϕ_g the phase shift of the grating, and k the complex wavenumber including the internal losses and detuning factor. Upon Laplace transform of the small-signal equations, the problem can be reduced to a simple matrix expression, cf. [37, 38]:

$$\left(\boldsymbol{M}_0 + \boldsymbol{M}_1\frac{\delta}{\delta z}\right)\boldsymbol{x} = \delta J \cdot \boldsymbol{h}_N + \boldsymbol{f}_{sp}, \tag{4.46}$$

where $\boldsymbol{M}_0(s, z)$ and $\boldsymbol{M}_1(z)$ are 4 x 4 matrices, $\boldsymbol{h}_N(s, z)$ and $\boldsymbol{f}_{sp}$ are 4-dimensional vector functions, and δJ is a scalar. The $\boldsymbol{h}_N(s, z)$ vector describes variation of gain and refractive index with carrier density and vector $\boldsymbol{f}_{sp}$ the Langevin noise terms. The relative amplitude and phase fluctuations are contained in vector $\boldsymbol{x} = [\delta a^{+}/a_s{}^{+}, \delta\phi^{+}, \delta a^{-}/a_s{}^{-}, \delta\phi^{-}]^T$, while δJ is the local change in carrier injection rate. The problem variables in Eq. (4.46), in general depend on $s = i\omega$, where ω is the baseband frequency. Adhering to boundary conditions at facets the Eq. (4.46), can be solved using the Green's function method but for simplicity we follow the methodology in [38], and rely on the Green's function solutions, $\boldsymbol{\zeta}_i(s, z', z)$, $i = 1, ..., 4$, of the operator that is adjoint operator over vector $\boldsymbol{x}$, Eq. (4.46). The problem is thus reduced to solution of:

$$\left(\boldsymbol{M}_0{}^{\dagger}(s,z') - \boldsymbol{M}_1{}^{\dagger}(z')\frac{\delta}{\delta z}\right)\boldsymbol{\zeta}_i(s,z',z) = \boldsymbol{e}_i\delta(z'-z), \tag{4.47}$$

where $(\boldsymbol{x}(s,z))_i$ can be expressed in terms of $\boldsymbol{\zeta}_i(s,z)$ as:

$$(\boldsymbol{x}(s,z))_i = \int_0^L \boldsymbol{\zeta}_i{}^{\dagger}(s,z',z)\{\delta J(s,z')\boldsymbol{h}_N(s,z') + \boldsymbol{f}_{sp}(s,z')\}dz', \tag{4.48}$$

where L is the length of the laser cavity. The small-signal problem given in matrix form Eq. (4.47), is essentially a system of four ordinary differential equations (ODEs) that can be solved numerically using some of the standard ODE solver libraries. The small-signal module was initially developed in MATLAB, as it allows for great flexibility in terms of the available numerical ODE solvers. However, to seamlessly integrate the small-signal postprocessing with the traveling wave module Sec. 4.2, it was subsequently also realized in C++, where the matrix operations and numerical solving of ODEs are performed with the help of readily available libraries [54, 55].

The main physical properties that we are interested in: spectral linewidth, RIN and FM-noise spectra, can be directly extracted from the solutions of ODE system, $\boldsymbol{\zeta}_i(s,z)$. The spectral linewidth is determined in low-frequency limit of the FM-noise spectra, $FM_{spect.}$:

$$\Delta\nu = \frac{1}{2\pi}\lim_{s\to 0} FM_{spect.}(s) = \frac{1}{2\pi}\frac{\int_0^L \boldsymbol{\zeta}_0{}^T(z)\,2\boldsymbol{D}\,\boldsymbol{\zeta}_0(z)dz}{\left(\int_0^L \boldsymbol{\zeta}_0{}^T(z)\,\boldsymbol{x}_0 dz\right)^2}, \tag{4.49}$$

where the main difference in our approach is inclusion of the injection rate dependent linewidth enhancement factor [34], which is expected to have a noticeable effect on spectral linewidth at higher injection currents. Other physical effects related to spectral linewidth that we additionally consider in this work, formation of carrier grating and colored carrier noise [47, 52], can be optionally factored in spectral linewidth through solutions of the traveling wave simulation. It should be noted that the noise sources, F_{sp} and F_N, are treated as classical Langevin

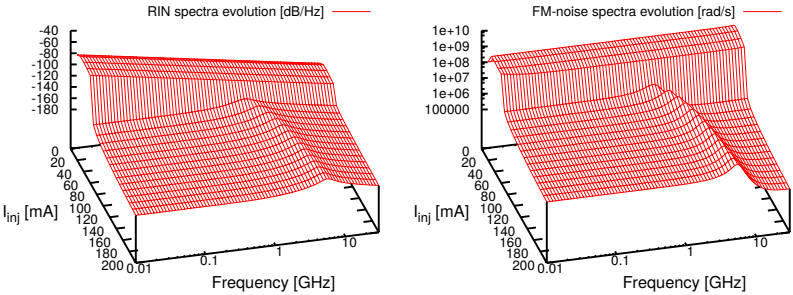

Figure 4.14: An example of calculated evolution of the RIN and FM-noise spectra with injection current for a 3-QW DFB laser with $\lambda/4$ phase shift.

functions in noise analysis module, meaning that the main contribution of colored noise to calculated spectral linewidth or noise spectra are the spatially correlated fluctuations of traveling wave variables.

$$RIN_{spect.}(s) = 4|(\boldsymbol{x}(s,0))_1|^2{}_{av} = 4\int_0^L \boldsymbol{\zeta}_1{}^{\dagger}(s,z)\, 2\boldsymbol{D}\, \boldsymbol{\zeta}_1(s,z)dz \quad (4.50)$$

$$FM_{spect.}(s) = |s|^2|(\boldsymbol{x}(s,0))_2|^2{}_{av} = |s|^2\int_0^L \boldsymbol{\zeta}_2{}^{\dagger}(s,z)\, 2\boldsymbol{D}\, \boldsymbol{\zeta}_2(s,z)dz \quad (4.51)$$

Aside from calculation of spectral linewidth, the other properties resulting from small-signal laser model that are also important for the laser diode characterization, are relative intensity noise (RIN) spectra and FM-noise spectra, Fig.(4.14). The noise properties can be similarly expressed as functions of vectors $\boldsymbol{\zeta}_i(s,z)$, $\boldsymbol{\zeta}_1(s,z)$ in the case of RIN spectra, Eq. (4.50), and $\boldsymbol{\zeta}_2(s,z)$ in the case of FM noise spectra, Eq. (4.51). Even though the main focus of practical simulation examples in Ch. 5 is on the problems of spectral linewidth in quantum dot lasers, the model can be readily used to simulate directly modulated laser diodes or other problems where the RIN or FM-spectra are relevant.

Chapter 5

Simulation Examples and Benchmarks

As a practical part of this thesis, this chapter is completely focused on commercially interesting photonic devices. The main interest of the presented study, revolves around single mode laser operation and a narrow spectral linewidth for which the designs are optimized. We begin with a study of basic optical communication elements, a DFB based laser diodes, which we further investigate within a more complex integrated device comprising a laser array. The results for the DFB lasers and the laser array are compared to performance of realized devices, while we conclude the simulation examples with a study of quantum dot lasers based on the high quality factor cavity design [50].

5.1 Quantum Dot Distributed Feedback Laser

Historically, the distributed feedback (DFB) lasers predate the distributed Bragg reflector (DBR) lasers and even today play an important role in modern optical communication systems. The simplicity of production is the key property that enables DFB lasers a vast presence in commercial communication solutions. In their simplest form it is even possible to fabricate them in a single epitaxial growth. Intrinsically, the DFB laser is a dual-mode device with resonant modes around the Bragg frequency, while the Bragg frequency itself is antiresonant.

Nevertheless, the single-mode operation that is of most interest in optical communications can be easily achieved by adding a phase shift somewhere along the laser cavity.

5.1.1 Design Principles

The approach to design of DFB lasers essentially depends on their particular application. With focus of our study being the externally modulated single-mode lasers, the key characteristics that we seek to optimize are narrow spectral linewidth and tunability of the lasing signal. When it comes to the choice of number of active quantum dot layers, it is essential to remember that this directly relates to peak modal gain. As a result of high peak gain, the laser will reach threshold for lower carrier densities which reduces the spontaneous emission noise, and will have a higher operating differential gain. Another benefit of the high modal gain is the fact that the threshold is reached for the lower saturation of the quantum dot ground state, resulting in more symmetric gain dispersion around the lasing frequency and thus lower linewidth enhancement factor which contributes quadratically to spectral linewidth. The laser model studied here does not support the effects of self-heating but nevertheless the effect of varying maximal modal gain can be thoroughly examined. To this end we will compare the DFB laser based on 2QD- and 5QD-layer epitaxy, and summarize the pros and cons of both designs.

A special attention should be also paid to the choice and design of the distributed feedback grating. The lateral surface grating design, [43], featured in all the laser designs that we will use to benchmark the simulation models, does offer great simplicity in terms of production but their placement on the side of the ridge waveguide where field intensity is weaker inevitably leads to reduced coupling coefficient. In the following examples it is shown however, that the simplicity of grating realization can be clearly utilized despite the minor drawbacks of the surface grating design.

5.1.2 Lateral Grating Design

Whether in DFB or DBR laser diodes, to tailor the laser output spectra in many commercial applications the Bragg grating is realized in buried grating technology. This approach can be justified by better

control of the grating properties and high yield of produced devices. However, the buried grating design inevitably entails a two-step epitaxial growth which increases the cost and production time. As an alternative approach, in most of the simulation examples considered here, we study the practicality of the lateral grating design. The main advantage of the lateral grating approach is the simplified production procedure, allowing one to essentially produce a functional DFB laser within one epitaxial growth step.

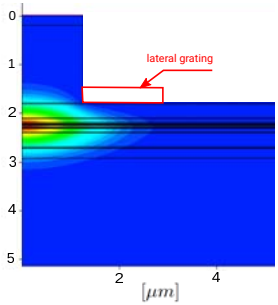

Figure 5.1: Fundamental TE mode with marked location of the lateral distributed feedback (DFB) grating.

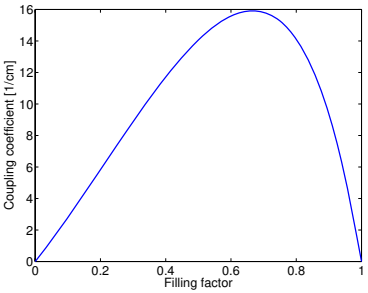

Figure 5.2: Calculated coupling coefficient of a lateral DFB grating vs. filling factor of the lateral grating.

The refractive indices of materials used in the lateral grating design are often quite different compared to the modal effective refractive index. This originates from the unique processing of the lateral grating, where after the initial etching of the ridge waveguide, the sides of the ridge are selectively etched to define the lateral grating. To accomplish this a grating layer needs to be added on top of the otherwise Fabry-Pérot epitaxy, Fig. (5.1), as for the epitaxy depicted in Fig. (4.5). The periodic voids that result from the etching are then either simply filled with air or in case of device planarization, with planarizing materials that often have significantly lower refractive index than the semiconductor materials used in the epitaxial growth. In either case, the effective index of the lateral grating is often much lower than the modal effective index, n_{eff}, which in our case makes originally derived equation for the coupling coefficient, Eq.(4.15), more appropriate.

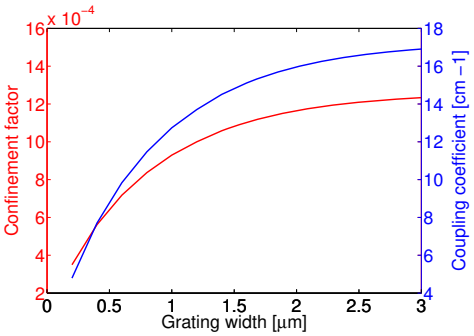

Figure 5.3: Calculated confinement factor and the maximum coupling coefficient for a 5QD-layer epitaxy with varying width of the lateral grating.

Naturally, some concerns can be raised regarding the remote location of the lateral grating with respect to the transversal mode profile. This can be a disadvantage of course, Fig. (5.1), as the confinement factor of the grating plays a major role in determining the practicality of the grating design. Fortunately, the great difference between the refractive indices of the materials comprising the grating is able to compensate for the intrinsically low confinement factor. The estimated coupling coefficient of the 2 µm wide lateral grating design on each side of the ridge, Fig. (5.2), is shown to be comparable to that of standard buried gratings. Aside from the materials used, there are also a few more possibilities to further increase the coupling coefficient of the lateral grating.

Ridge width [µm]	**Conf. factor**	**Effective index**	**Coupling coeff.** [cm^{-1}]
1.75	$1.572 \cdot 10^{-3}$	3.22465	21.50
2.00	$1.265 \cdot 10^{-3}$	3.22543	17.30
2.50	$0.975 \cdot 10^{-3}$	3.22647	13.33

Table 5.1: Dependence of the lateral grating properties on the ridge width of a 2 µm wide grating on each side of the ridge.

In case of the fixed ridge width of 2 µm, it is possible to increase the width of the grating design in order to increase the confinement

factor. However, this approach is limited by the mode profile and as shown in Fig. (5.3), the confinement factor saturates at ~ 2 μm and further increase of the grating width does not lead to a significant increase of the coupling coefficient. Another possibility is to place the lateral grating closer to the peak of transversal mode intensity by reducing the ridge width. This is demonstrated in Table (5.1), where the reduction of ridge width from 2.5 μm to 1.75 μm is shown to lead to increase of the coupling coefficient by 61%. In case that higher coupling coefficient is necessary, further improvement is also possible by careful engineering of the transversal mode profile or by increasing the thickness of the grating layer, which would also result in higher confinement factor.

5.1.3 Performance of the 2QD- and 5QD-layer DFB Laser Design

To compare the performance of 2QD- and 5QD-layer designs, the design of the cavity is also kept simple just as for the DFB grating design. We use a 1200 μm long cavity with a uniform surface DFB grating, for which the record spectral linewidth of 110 kHz was measured for a device with only two active QD layers [56]. The ridge width of 1.75 μm is chosen to ensure sufficient coupling coefficient as the confinement factor of the grating is significantly affected by the ridge width, Table (5.1).

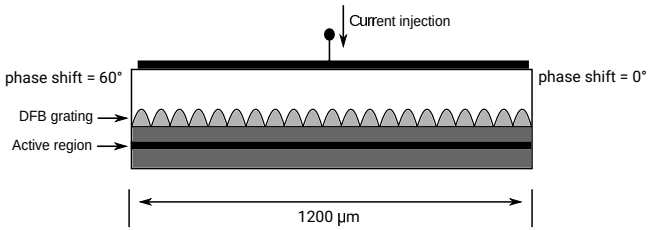

Figure 5.4: Illustration of a laser cavity design used for the numerical modeling of a QD-DFB laser.

To calibrate the simulation parameters we rely on the measurement of the LI-curve as a basic figure of merit, Fig. (5.5), which is available for the 2QD-layer design, while the parameter set for the 5QD-layer

Parameter	Value
Quantum dot density, N_{dot}	$3.25 \cdot 10^{10}$ cm^{-2}
Effective active layer thickness, Zl_{eff}	1 nm
Electron effective mass (InAs), m_e	$0.023 \cdot m_0$
Heavy-hole effective mass (InAs), m_{hh}	$0.3 \cdot m_0$
Homogeneous broadening (electrons and holes)	15 meV
Inhomogeneous broadening	10 meV
Nonlinear gain saturation coefficient	$3.4 \cdot 10^{-16}$ cm^3
Injection efficiency, η_i	0.55
Shockley-Read-Hall recombination coefficient, A	$5.5 \cdot 10^7$ s^{-1}
Radiative recombination coefficient, B	$1.35 \cdot 10^{-10}$ cm^3/s
Auger recombination coefficient, C	$0.7 \cdot 10^{-28}$ cm^6/s
Effective refractive index, n_{eff}	3.23
Confinement factor, Γ	0.009 (2QD)/0.0225 (5QD)
Coupling coefficient	9 cm^{-1}
Internal losses	12 cm^{-1}

Table 5.2: Parameters for the dynamic simulation of QD-DFB lasers.

design is extrapolated by adapting the confinement factor which is obtained from the FEM simulation of the fundamental transversal mode. From Fig. (5.5), it can be seen that the parameter set, Table (5.2),

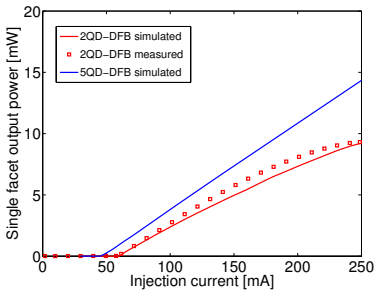

Figure 5.5: LI-curve of the 2QD- and 5QD-DFB laser designs.

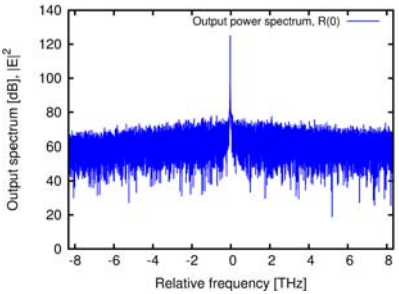

Figure 5.6: Simulated spectrum at the left facet of 2QD-DFB laser design.

provides a good fit in terms of the LI-curve of 2QD-layer DFB design. The correct simulation of the threshold condition confirms the choice of recombination parameters which were adopted from [57], as well as the choice of internal losses and coupling coefficient. Moreover, the simulated output spectrum at 210 mA, Fig. (5.6), of the 2QD-DFB device confirms particularly the choice of the radiative recombination coefficient, as the side mode suppression ratio (SMSR) is also in accordance with the measurements. The internal losses are chosen slightly higher than the value of 10 cm^{-1}, that was obtained in the measurements [28]. The coupling coefficient of 9 cm^{-1}, is on the other hand significantly lower compared to the values obtained numerically, Table (5.1). The potential reasons for this can be the processing procedure of the surface DFB grating and the photon scattering from the grating. Namely, the geometry in the calculation of coupling coefficient is considered perfect while in reality the etching and planarization procedure can introduce roughness of grating edges and nonuniform confinement factor along the grating. Regarding the nonlinear gain saturation coefficient, the value used in simulation, $3.4 \cdot 10^{-16}$ cm^3, can be considered

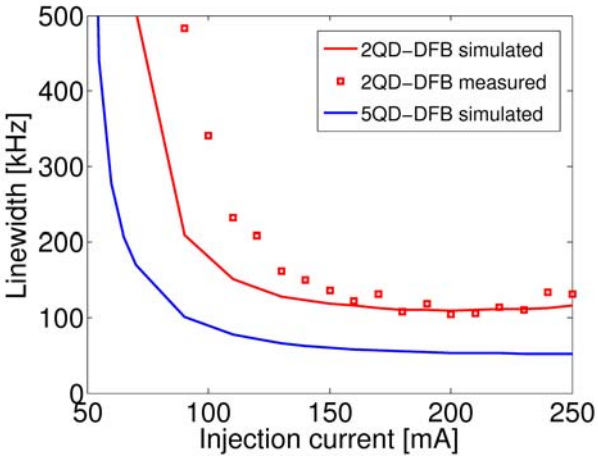

Figure 5.7: Simulation and measurement of the spectral linewidth for 2QD- and 5QD-DFB laser designs.

typical for the quantum dot active material [58]. The chosen saturation coefficient is significantly higher than for the bulk and quantum well lasers but it can be considered an overestimation for the considered quantum dot epitaxy, as the numerical model does not include the self-heating effects which are essentially factored in the saturation coefficient in order to match the LI characteristic.

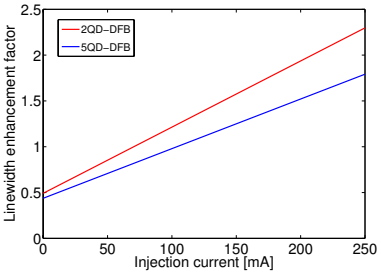

Figure 5.8: Injection dependent LEF factor of the QD-DFB designs.

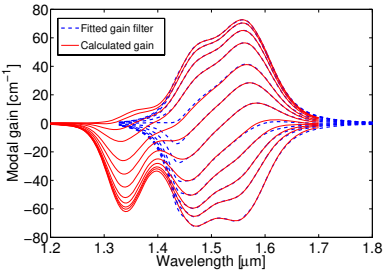

Figure 5.9: Gain filter and calculated gain dispersion of the 5QD-DFB design.

Since the simulation is able to produce a realistic LI-curve, when comparing the linewidth vs. the injection current of the 2QD-DFB design the results are also satisfactory, Fig. (5.7). The linewidth minimum of 110 kHz is obtained in the simulation results as well, while the rebroadening at higher injection currents is reproduced by the inclusion of the injection dependent linewidth enhancement factor [34]. Even though the performance of 2QD-DFB laser can be considered as high-end if not a record for the class of DFB lasers, on the LI-curve and linewidth, Figs. (5.5,5.7), we also give the extrapolated performance of the 5QD-DFB design for the same laser geometry, which indicates a superior performance. The improvements can be noticed on all major aspects, the threshold is reduced by $\approx$ 15 mA, the output power is significantly higher, and most importantly the spectral linewidth is reduced by a factor 2, reaching a minimum linewidth of 53 kHz.

As the geometry of 2QD- and 5QD-DFB design is taken the same, the explanation for the superior performance mainly lies in the properties of the active region. Even though the quantum dot epitaxy is the same in both cases, by simply increasing the number of active

layers significant improvements can be made. The slope efficiency is improved as a consequence of the higher differential gain. The maximal modal gain is increased by more than double, Fig. (5.9), which in turn allows for lower transparency and threshold carrier density, leading to lower contribution of the spontaneous emission noise and thus lower spectral linewidth. Moreover, the behavior of linewidth enhancement factor above threshold should not be overlooked here as it contributes quadratically to spectral linewidth. From Fig. (5.8) we can see that the injection rate dependent linewidth enhancement factor is lower for the 5QD-DFB case, as the saturation of the active material is significantly lower for the same threshold gain, thus making it more immune to negative contribution of the wetting layer at higher injection currents, Ch. 3.

5.1.4 Effect of Colored Noise and Carrier Grating on Linewidth

When considering the effects of carrier grating and correlated/colored noise on the spectral linewidth we have to bear in mind the constraints of the framework of traveling wave model. For the implemented formation of carrier grating, Ch. 4, the most relevant characteristic of the model is the slowly varying envelope approximation.

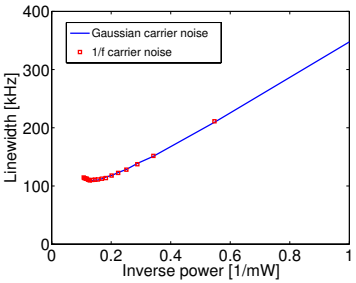

Figure 5.10: Linewidth vs. inverse output power of 2QD-DFB design, $1/f$ carrier noise effect.

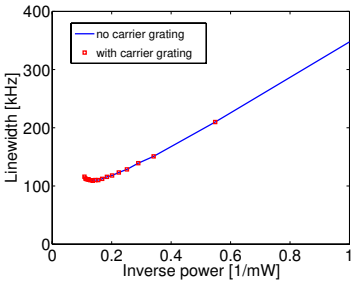

Figure 5.11: Linewidth vs. inverse output power of 2QD-DFB design, carrier grating effect.

In that sense the interaction of the fast varying component of the resonating field and the carrier grating component is omitted, but the carrier grating still adds to the spatial whole burning which intrinsically can lead to mode hopping and deteriorate the spectral linewidth. In a similar manner the inclusion of the colored $1/f$ noise is also partially limited by the model, i.e. by the postprocessing module which extracts the linewidth. Namely, in the postprocessing step the noise sources are still considered Gaussian, meaning that the effect of colored noise is also limited to the problem of mode stability as it introduces longitudinal fluctuation to the carrier density through correlated noise sources along the laser cavity.

The effect of colored noise and carrier grating is examined for the 2QD-DFB design, Figs. (5.11,5.10). The carrier grating pattern, Eq. (4.25), is characterized by the ambipolar diffusion coefficient [47], $D_{ap} = 12$ cm^{-2}s^{-1}, while for the $1/f$ carrier noise we consider the extreme case, where the carrier noise generation is completely substituted with the correlated noise process of the same strength, i.e. $\xi = 1$ in Eq. (4.31). The calculated amplitude of the carrier grating pattern is two orders of magnitude lower than the threshold carrier density, and from the Fig. (5.11) it can be seen that there is no significant contribution to the linewidth while the lasing mode remains stable even at higher output powers. For the case of $1/f$ noise, the conclusion is the same, the lasing mode remains stable with no additional linewidth broadening, Fig. (5.10). At this point we can conclude that for the given parameters of the 2QD-DFB model, Table (5.2), the injection rate dependent linewidth enhancement factor plays a more dominant role in the phenomena of linewidth saturation and linewidth rebroadening.

5.2 Integrated Laser Array

So far we have considered only isolated quantum dot semiconductor lasers and their performance, while on the other hand many of the practical photonic devices comprise multiple integrated photonic elements. To enable flexibility and reconfigurability, the design of modern wavelength demultiplexing (WDM) optical communication networks often imposes additional functionality on photonic integrated circuits which act as wavelength switches, such as reconfigurable add-drop multiplex-

ers (ROADM) and optical cross-connect (OXC) systems. For these applications as well as for backup sources in point-to-point (WDM) optical connections, tunable integrated laser arrays can be an indispensable solution.

5.2.1 Design Principles

By integrating a DFB laser, as in Sec. 5.1, with additional photonic devices such as laser couplers and SOAs, it is necessary to reevaluate the performance of laser diodes. Being a part of a photonic integrated circuit the laser diodes are often affected by the coupled elements through back-reflections or the additional heating in case of active devices like SOAs. Worth mentioning here are the few earlier works on the topic of back-reflection [59, 60], showing that both the relative intensity noise and spectral linewidth can be significantly degraded by coupling the laser directly to a SOA amplifier through amplified spontaneous emission. This holds however for all types of additional components that provide either amplified or attenuated feedback, which can affect dramatically the linewidth and noise levels [7]. This effect can be both positive or negative, depending on the nature of the feedback.

The main characterization points of the integrated laser array are the power and spectral linewidth of the output signal and the tuning range of the laser array over which the emitted signal carrier is stable. To ensure a wide tuning range the laser coupler needs to be able to accommodate sufficient number of wavelength-shifted DFB lasers to cover the desired wavelength range. An example of a practical laser array in [61], uses 12 DFB lasers to cover the full C-band wavelength range ($\approx$ 38 nm). Meaning that the tuning range for an individual laser is only 3.17 nm, on average. The thermal tuning gradient of the laser diodes is typically in the range of 0.3 nm/K, while the desired thermal operating range is around the room temperature. Such a broad operating spectrum in turn puts a constraint on the laser coupler whose transmission characteristic should ideally be wavelength invariant over the considered range. After passing the signal through the coupler the signal is commonly amplified by the integrated SOA amplifier to adjust the output power for long range optical transmission.

As in the case of DFB laser examples, Sec. 5.1, the example of laser array considered here is also limited to a single-step epitaxial growth

which additionally needs to accommodate the laser coupler and potentially a SOA. Even though this introduces significant constraints on the design, a positive side is also present. Namely, as the coupler is operated as a passive component and based on the same active QD layers, through absorption it can serve as an isolation for the back-reflection or amplified spontaneous emission in case that the photonic circuit comprises a SOA amplifier or other additional components. This can reduce the negative effect of concatenating components and preserve the signal properties such as spectral linewidth and RIN spectra.

5.2.2 Design of the Laser Coupler

The design of the laser coupler is investigated using the commercial software FIMMPROP, based on the eigenmode expansion method (EME) [62]. The two coupler designs that we consider are multi-mode interference (MMI) coupler [63], and a classical Y-junction coupler. Both coupler designs rely on fundamentally different principles to couple the optical signal into a single output branch. The Y-coupler couples the input signals by physically merging the two input branches via a Y-junction, while the MMI coupler relies on the self-imaging principle intrinsic to multi-mode waveguides.

Figure 5.12: Simulation of the MMI coupler accommodating 12 laser ports, excitation from the left-hand side.

The interfaces between the photonic devices are known to be problematic. The transitions from multi-mode to single-mode devices often

require tapered sections to minimize the losses at the interface. Even for the case of single-mode to single-mode device coupling the mismatching waveguide geometry and transition to different epitaxy can introduce both reflection and diffraction losses. Due to the technological reasons, we are limited to device processing based on a single-step epitaxial growth. As a consequence, the laser array solution considered here is based on a uniform epitaxy, while the individual sections can be operated as active or passive. For this reason we can expect that the effective indices at the interface between lasers and the laser coupler in our case will be fairly similar, thus minimizing the reflections at the interface.

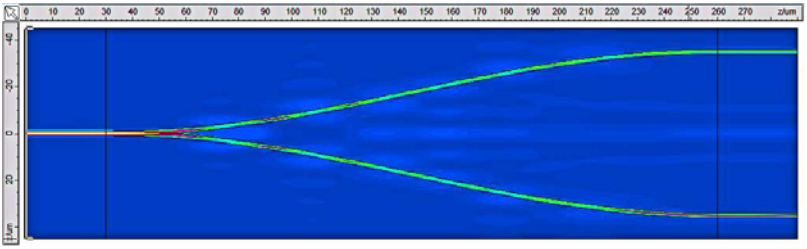

Figure 5.13: Simulation of the Y-coupler design, excitation from the left-hand side.

Etching depth [μm]	**Guided modes with effective indices**
1.9	$TE_{10}(3.2288)$ $TM_{10}(3.2255)$
2.07	$TE_{10}(3.2246)$ $TM_{10}(3.2216)$
2.12	$TE_{10}(3.2231)$ $TM_{10}(3.2205)$
2.22	$TE_{10}(3.2203)$ $TM_{10}(3.2185)$, $TE_{20}(3.1873)$ $TM_{20}(3.1808)$
2.3	$TE_{10}(3.2184)$ $TM_{10}(3.2171)$, $TE_{20}(3.1774)$ $TM_{20}(3.1738)$
2.415	$TE_{10}(3.2163)$ $TM_{10}(3.2157)$, $TE_{20}(3.1666)$ $TM_{20}(3.1661)$

Table 5.3: Guided modes of the Y-coupler for different etching depths of the 5QD-layer epitaxy, starting from the grating level - 1.9 μm.

If we are comparing the MMI coupler, Fig. (5.12), to a Y-coupler, Fig. (5.13), the advantages of the MMI coupler can seem difficult to surpass. The MMI coupler can be particularly useful if the tuning ranges of the individual lasers are more modest, as it can couple a large

number of lasers with a total coupler length ~ 1000 μm, which is in the range of the length of DFB laser diodes, Fig. (5.12). For this reason it can be found in many practical solutions [61], with a fairly broad transmission characteristic. However, as the quantum dot absorption in the coupler is polarization dependent and in general atypical for the MMI coupler design, we have preferred the Y-coupler for the realization of the laser array. Even though traditionally it supports only two laser ports, larger arrays can be realized by simply cascading the Y-coupler, Fig. (5.13).

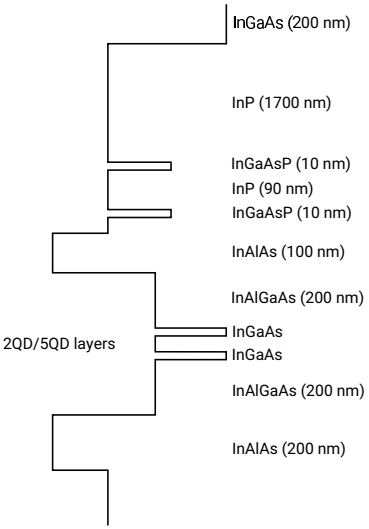

Figure 5.14: Sketch of the quantum dot laser epitaxy, relative conduction band edge and thicknesses of the layers.

What might not have been obvious so far is that the etching depth, beneficial for the weakly guiding ridge waveguide of the laser, Sec. 4.2, is in contradiction with the design principles of both coupler types. In the case of MMI coupler a stronger field confinement is necessary to excite the higher order modes and for the Y-coupler to minimize the losses which occur through bending of the coupler branches over the finite coupler length. As a result, both functioning coupler mod-

els depicted in Figs. (5.12,5.13), were obtained by additional selective etching of the coupler section below the level of the surface grating which was used for the DFB lasers. To put the significance of this modification into perspective, it is enough to compare the transmission of Y-coupler with etching depth at the grating level as for the DFB lasers, 1.9 μm, and the modified Y-coupler with further etching down to 2.12 μm, Fig. (5.13), which additionally removes the grating and the top cladding layer, Fig. (5.14). When excited from the left hand side this translates to an improvement in transmission from mere 0.7% up to 42.1% per branch. Further etching of the otherwise adiabatic coupler at this point could increase the transmission, however, from the Table (5.3), we can see that this would inevitably introduce higher order modes that would transmit a fraction of the total power. This in turn can cause problems if we want to couple the signal from the coupler to a single-mode SOA or an optical fiber. Another drawback that we should not neglect is the introduction of the diffraction losses through additional etching at the laser-coupler interface which are already present at the etching level of 2.12 μm.

5.2.3 Spectral Linewidth of the Coupled Lasers

In order to adapt the integrated coupled lasers for the traveling wave simulation we rely on the simulation results of the Y-coupler, Fig. (5.13), obtained by the FIMMPROP software [62]. Aside from the determined transition per branch of 42.1%, we also need to account for the losses at the laser-coupler interface. As we have mentioned earlier the losses at the coupler interface are caused mainly by the difference in the etching depth of the laser ridge and the coupler section. More precisely, at the interface we step down from 1.9 μm etching depth down to 2.12 μm etching depth. The interface losses were shown to be mostly in the form of diffraction losses as the variation of effective refractive index along the device is minor.

For the active laser section we use essentially the same parameters as for the QD-DFB laser example, Table (5.2), with the slightly altered values for the internal absorption and the coupling coefficient of the grating. The internal absorption is set to 11 cm^{-1} and the coupling coefficient to 14 cm^{-1}, Table (5.4), where the change in the coupling coefficient is somewhat larger but still in the range of the calculated values

Parameter	Value
Quantum dot density, N_{dot}	$3.25 \cdot 10^{10}$ cm^{-2}
Effective active layer thickness, Zl_{eff}	1 nm
Electron effective mass (InAs), m_e	$0.023 \cdot m_0$
Heavy-hole effective mass (InAs), m_{hh}	$0.3 \cdot m_0$
Homogeneous broadening (electrons and holes)	15 meV
Inhomogeneous broadening	10 meV
Nonlinear gain saturation coefficient	$3.4 \cdot 10^{-16}$ cm^3
Injection efficiency, η_i	0.55
Shockley-Read-Hall recombination coefficient, A	$5.5 \cdot 10^7$ s^{-1}
Radiative recombination coefficient, B	$1.35 \cdot 10^{-10}$ cm^3/s
Auger recombination coefficient, C	$0.7 \cdot 10^{-28}$ cm^6/s
Effective refractive index, n_{eff}	3.23
Confinement factor, Γ	0.009 (2QD)
Coupling coefficient	14 cm^{-1}
Internal losses	11 cm^{-1}

Table 5.4: Parameters for the dynamic simulation of the 2QD-DFB lasers coupled via Y-coupler.

for the surface grating design, Fig. (5.3). The aforementioned parameter changes were performed mainly in order to match the threshold of the measured LI-curve for the PIC with two coupled QD-DFB lasers. The simulation is performed only for the design based on 2QD-layer epitaxy as the gain parameters were adjusted based on the performance of the realized 2QD-DFB laser that was available, Fig. (5.5). The coupler section is modeled as passive, having maximum total absorption of 34.5 cm^{-1} at the Bragg wavelength, the calculated losses at the laser-coupler interface are also included while the total transmission losses of the Y-coupler determined using the eigenmode expansion method, Fig. (5.13), are included as lumped at the Y-junction. The model features can be easily discerned from the longitudinal profiles of the forward and reverse propagating field envelopes of the traveling wave model, Fig. (5.15). The phase shift at the left facet is kept the same as for the DFB model at 60°, Fig. (5.4), as well as the reflectivity of both facets which are modeled as cleaved.

The performance of the laser integrated to a Y-coupler based on

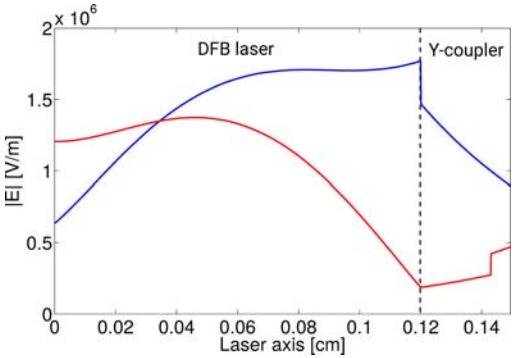

Figure 5.15: Forward and reverse propagating envelopes of the simulated 2QD-DFB+Y-coupler integrated optical circuit.

the 2QD-layer epitaxy is particularly interesting to compare to the performance of the DFB laser design, Figs. (5.5,5.7), as the epitaxy of the DFB lasers in both cases is the same as well as their length of 1200 μm. By comparing the simulated and measured LI-curve at the left facet of the coupled laser design based on the 2QD-layer epitaxy, Fig. (5.16), we can see that the simulation corresponds fairly well to the measurements with some divergence at the higher injection currents. The output power is lower than for the DFB design,

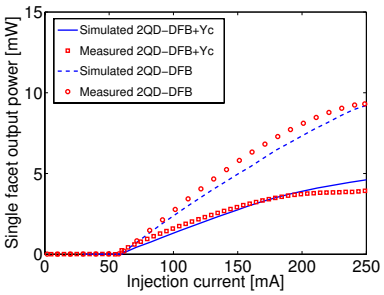

Figure 5.16: Simulated and measured LI-curve of the coupled laser.

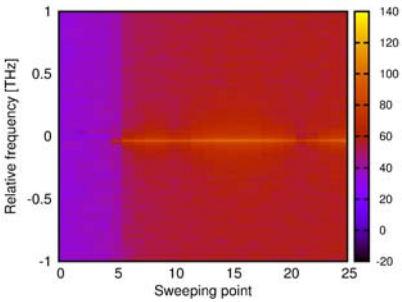

Figure 5.17: Calculated spectrum at the left facet of coupled laser design.

while from the calculated output spectrum for the sweeping current Fig. (5.17), we can see that the lasing mode remains stable over the observed current range without significant deterioration of the side mode suppression ratio. The spectral linewidth on the other hand is significantly higher than for the DFB laser, Fig. (5.18), with measured linewidth reaching a minimum of 1 MHz, compared to 110 kHz for the DFB design, Fig. (5.7).

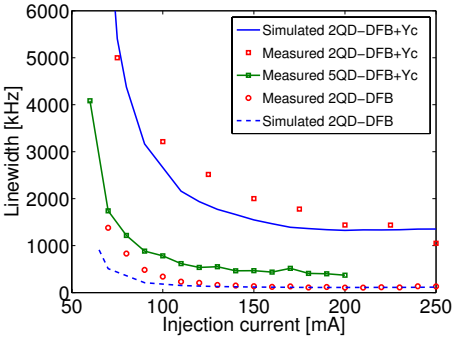

Figure 5.18: Calculated and measured spectral linewidth of the coupled laser design for 2QD-layer epitaxy and measured linewidth for the design based on 5QD-layer epitaxy, with included 2QD-layer DFB laser linewidth for comparison.

To understand the mechanism behind the linewidth increase it is worth considering the effect of the absorbing coupler section on the active material of the laser. Compared to the DFB design the biggest change that we make is the concatenation of the absorbing Y-coupler. By introducing the additional losses we need more gain to reach the threshold condition, this leads to higher saturation of the quantum dot state and thus a higher linewidth enhancement factor. Aside from the negative impact on the linewidth enhancement factor the photon density in the laser section is also reduced as the resonating field is not confined only to the laser any more, from the basic Schawlow-Townes linewidth equation, Eq. (1.2), we can see that this has an additional negative impact on the linewidth. The extracted mean modal gain along the laser section at threshold is 20.53 cm^{-1}, which corresponds to ground state population of $\rho = 0.843$, meaning that the laser is

operating close to full inversion. As a result of this it was necessary to set the linewidth enhancement factor at threshold to $\alpha = 3$, in order to match the measurement results, Fig. (5.18), which suggests a negative impact of the wetting layer on linewidth enhancement factor even at lower injection currents. To further support this conclusion we can also compare the measurements for the 5QD-layer epitaxy, Fig. (5.18), based on the same design and a DFB section length of 1145 μm. For the 5QD-layer design the linewidth reaches a minimum of 370 kHz, and at a significantly lower saturation of the ground state simply by having a higher maximum modal gain through increased number of active layers. For this reason one could also expect an improved performance of the 2QD-layer epitaxy if the gain saturation is taken into account as an optimization point, in order to reduce the increase of the linewidth enhancement factor at higher injection currents.

5.3 High Quality Factor Cavity Design

The distributed feedback laser design, presented in Sec. 5.1, is based more or less on a traditional design approach used in the previous decades from bulk to modern quantum well and quantum dot lasers. Even though the simulation and empirical results of the quantum dot DFB lasers show significant potential for their application in future optical communication networks, it is worth considering what can be done in terms of resonant cavity optimization. To this end we seek to employ the design features of a novel approach, which has been already empirically tested on quantum well lasers [50], in order to further reduce the spectral linewidth of quantum dot lasers. On the examples presented here, we will demonstrate that with the combination of high-performance active material such as quantum dots and an innovative cavity design we can further reduce the spectral linewidth to below 10 kHz, while investigating the resulting operating conditions.

5.3.1 Design Principles

Traditionally, major concerns regarding the design of edge emitting lasers include: the stable single mode emission, broad tuning range and narrow spectral linewidth. With the inclusion of phase shifts in

the DFB grating, the DFB lasers can easily produce a single-mode emission and due to the reliable processing steps they have played an important role in the development of optical communication networks. The evolution of the active material from bulk to quantized structures such as quantum wells and quantum dots has provided further significant advances in their performance, mainly in terms of the threshold, efficiency and the modulation rate. The approach to the design of resonant cavity on the other hand has not changed significantly. However, the encouraging results in [50], clearly show that the cavity design is worth reconsidering if we want to produce a laser with high spectral purity of the emitted signal.

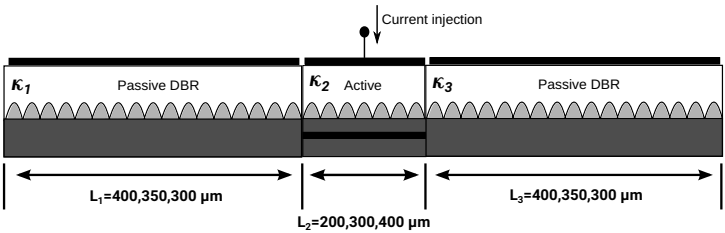

Figure 5.19: Illustration of a laser cavity based on the high quality factor design.

The central idea of the work presented in [50], is the reduction of the spectral linewidth through increased quality factor of the resonant cavity. The possible approaches to achieve this, include the reduction of the internal cavity losses and the increase of reflectivity of the grating and the facets. The reduction of internal losses can be achieved either through engineering of the transversal mode to low loss materials or by the introduction of passive laser sections comprising the low loss materials. The increase of the reflectivities can be also desirable, however, in extreme cases it can also result in mode hopping. As we are studying the design based on the high quality factor cavity only numerically, Fig. (5.19), for the active section we will keep the same parameters as for the DFB laser case, Sec. 5.1, to provide a better insight into the resulting performance improvement. The passive side sections we will consider longer and completely lossless, while keeping the total device length at 1000 μm. The coupling coefficients $\kappa_{1,2,3}$, will be set higher compared to the DFB design as: $\kappa_1 = 15$ cm^{-1},

$\kappa_2 = 50$ cm^{-1} and $\kappa_3 = 15$ cm^{-1}, in order to increase the quality factor and thus reduce the threshold modal gain and carrier density. To ensure the low saturation of the quantum dots, aside from the high coupling coefficients we will also assume the 5QD-layer epitaxy, which should result in a favorable linewidth enhancement factor. Such a design approach should result not only in better threshold condition of the active central section, Fig. (5.19), but also in reduced spontaneous emission noise in the cavity as the side sections are operated as passive.

5.3.2 Operating Conditions and Linewidth of the High Quality Factor Design

In order to obtain the single mode operation, we introduce a $\lambda/4$ phase shift at the center of the cavity while setting the power reflectivities of the facets to 2%. The phase shift and the high coupling coefficient of the active section shift the majority of the resonating photons into the active region, while the facet reflectivity is reduced in order to maintain a stable single mode operation at higher injection currents.

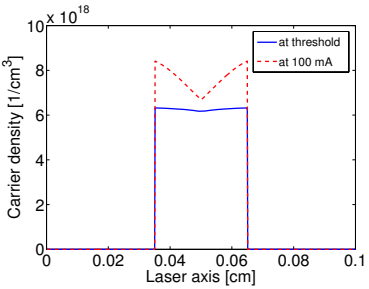

Figure 5.20: Calculated carrier density profile of the high Q-factor design, with a 300 µm long active section.

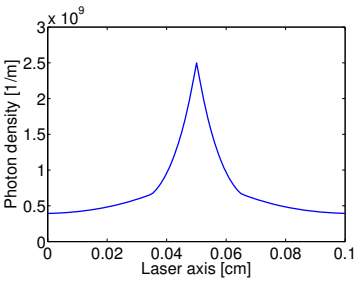

Figure 5.21: Calculated photon density profile of the high Q-factor design, with a 300 µm long active section.

From the photon and carrier density profiles depicted in Figs. (5.20,5.21), we can see more clearly how the choice of parameters governs the device operation. The accumulation of the photons in the center of the

cavity Fig. (5.21), is beneficial for obtaining a lower threshold current, as the effective material gain in the cavity is significantly reduced through passive side sections. On the other hand, we can also see that the calculated photon density profile at moderate injection of 100 mA, already has a strong impact on the spatial hole burning of the carrier population, which becomes apparent if we compare it to the calculated carrier density profile at threshold, Fig. (5.20). The negative effect of the spatial hole burning is not only in the common problem of mode stability arising from the consequent spatial variation of the modal gain and refractive index, but also in the increase of spontaneous emission noise as higher carrier densities are necessary to achieve the same modal gain under a strong gain suppression.

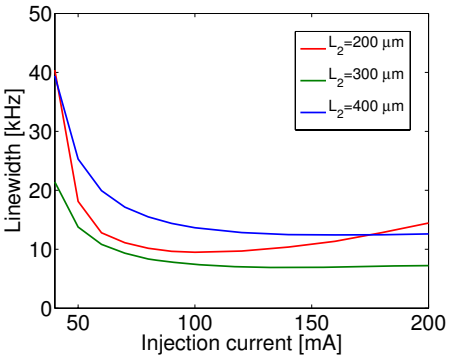

Figure 5.22: Calculated spectral linewidth of the high Q-factor cavity design, for varying length of the central active section.

The linewidth calculations, Fig. (5.22), are performed on three design variations, each with a total device length of 1000 µm, and the lengths of individual sections as given in Fig. (5.19). The first striking feature that we can notice is the significantly lower linewidth compared to the classical DFB case based on the same epitaxy, where the strongest linewidth reduction is observed for the central section length of 300 µm, yielding a linewidth reduction by a factor of 7.57 at the minimum of 7 kHz. The calculated average spontaneous emission rate at threshold of the high Q-factor design with 300 µm long active section is $R_{sp} = 2.5346 \cdot 10^8 s^{-1}$, also represents a significant improvement

Active section length, L_2	Ground state population, ρ_{th}
200 µm	0.82
300 µm	0.71
400 µm	0.66

Table 5.5: Calculated population of the quantum dot ground state for different active section lengths of the high Q-factor design.

compared to the value of $R_{sp} = 6.721 \cdot 10^8 s^{-1}$, calculated for the 5QD-layer DFB laser, Sec. 5.1. To get a better overview of how different effects affect the spectral linewidth, it is useful to recall the modified Schawlow-Townes linewidth equation, Eq. (1.4). As the spectral linewidth is directly proportional to the spontaneous emission rate, we can see that the lower spontaneous emission alone contributes already to the linewidth reduction by a factor of 2.652. The other strong contribution to linewidth reduction is the high photon density in the cavity obtained by the high coupling coefficients, Fig. (5.21), which on the other hand is inversely proportional to the spectral linewidth. In general we can see that even if the internal losses of the active central section are left the same as for the DFB case, at 12 cm^{-1}, we can still obtain a strong linewidth reduction through lossless side sections and increased coupling coefficients of the grating.

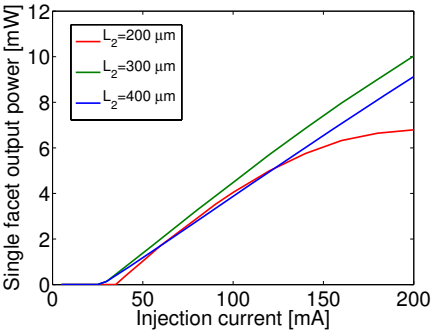

Figure 5.23: Calculated output power at the left facet of the high Q-factor cavity design, for varying length of the central active section.

As we can see from the Fig. (5.22), some care should be taken when it comes to selection of the length of the active central section. All three considered designs with varying length of the central section behave quite differently. This can be better understood if we calculate the population of the quantum dot ground state, Table (5.5), which is estimated by comparing the threshold modal gain to calculated maximal modal gain of the 5QD-layer epitaxy. The case with the shorter length of 200 μm is most critical as it operates close to full inversion, in which case the linewidth enhancement factor degrades more strongly at higher injection currents. This can be clearly seen in Fig. (5.22), as the linewidth consequently broadens as we increase the injection current. Moreover, the degradation of performance of the shorter active section can be seen from the calculated LI-curve in reduced output power as well, Fig. (5.23), as the high gain suppression at higher photon densities pushes the modal gain to its limits while reducing the differential gain. The negative effect of the gain suppression can be also further increased if the coupling coefficient is set too high [64]. This problem can be alleviated with longer active section length, however, we can also see that for the higher length of 400 μm, the linewidth is again degraded but this time by minimizing the positive contribution of the passive side sections as they get shorter and more spontaneous emission noise is introduced. For the considered setup, Fig. (5.19), this leaves the active section length of 300 μm as a compromise between

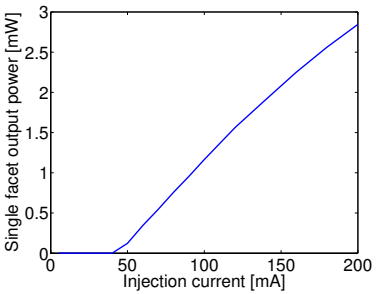

Figure 5.24: Calculated LI-curve of the high Q-factor design, with reduced losses in a 300 μm long active section.

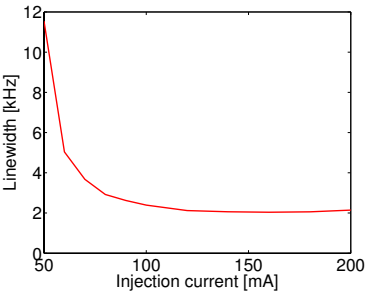

Figure 5.25: Calculated linewidth of the high Q-factor design, with reduced losses in a 300 μm long active section.

the two aforementioned effects, Fig. (5.22).

In order to obtain even lower linewidths, we follow further design guidelines given in [50], regarding the reduction of the internal losses in the active central section by engineering the transversal mode profile toward the low-loss materials of the ridge waveguide. To that end, we assume that the internal losses are directly proportional to the confinement factor, and reduce the both values by a factor of three. By this we effectively reduce the internal losses from 12 cm^{-1} to 4 cm^{-1}, and the maximal modal gain from roughly 75 cm^{-1} down to 25 cm^{-1}. The geometry is kept the same as for the case with 300 μm long central section, while the coupling coefficients are set to: $\kappa_1 = 25$ cm^{-1}, $\kappa_2 = 50$ cm^{-1} and $\kappa_3 = 25$ cm^{-1}, in order to obtain similar threshold current as in Fig. (5.23). The simulation results of the resulting modifications are given in Figs. (5.24,5.25), showing further reduction in linewidth from 7 kHz down to 2 kHz, but at the expense of the maximal output power. Compared to the minimum linewidth of the 5QD-layer DFB design of 53 kHz in Sec. 5.1, the modified high Q-factor cavity design with reduced internal losses yields an impressive linewidth reduction by a factor of 26.4.

One could also consider some other possible design variations of the high Q-factor cavity design. In case that the coupling coefficients considered here are difficult to achieve in practice, one could essentially try to compensate the lower coupling coefficients by a longer cavity length. This case is also considered in [64], with somewhat different parameters, showing favorable results despite the lower coupling coefficients of the sections. Moreover, the linewidth obtained in Fig. (5.25), is not necessarily the lowest [65]. One could consider here a further reduction of the linewidth, through reduction of the internal losses or by shorter length of the active section, but as shown in Fig. (5.24), at the cost of the output power.

Chapter 6

Conclusions and Outlook

6.1 Major Results

To summarize the achievements presented in this thesis, it is worth recalling the motivation for narrow-linewidth lasers and challenges that accompany their design. The evergrowing need for higher bit rates in modern optical communication networks imposes the use of higher-order modulation schemes to satisfy the requirements within the existing optical network infrastructure. The spectral purity of the modulated signal comes as a basic requirement for the realization of such high bit rate systems. To this end we have used high-end quantum dot epitaxy and optimization of the laser cavity to reach record linewidth values.

To aid the design process and investigate the interplay of different factors governing the linewidth of the laser diodes, the *QD-wave* laser simulator was developed from scratch. Compared to other laser simulators based on the traveling wave model [47, 66], we have included some additional features as the injection dependent linewidth enhancement factor, colored carrier noise and formation of the carrier grating pattern. This has allowed us to reach new conclusions and in cooperation with experimental partners to demonstrate that when it comes to linewidth the quantum dot based lasers are capable of outperforming the bulk and quantum well based laser designs.

The experimental results in Ch. 5, show the obtained linewidth of only 110 kHz for the DFB laser design with 2QD-layer epitaxy. It is important to stress that this is achieved in a single-step epitaxial growth by relying on the surface Bragg gratings, which enables a production of high performance laser diodes through a relatively simple production process and thus at a reduced cost. The laser model suggests even lower linewidth for the 5QD-layer DFB design, through the reduction of spontaneous emission noise and linewidth enhancement factor. To show that the single-step epitaxial growth can be extended to integrated devices, we have included a design of a two-laser array in the same technology based on the Y-coupler, which is also supported by the measurements. The integrated device is shown to be susceptible to broadening of the linewidth, which can be nevertheless compensated by careful design of the active section and reduction of the back-reflections and amplified spontaneous emission. The lowest linewidth in this case is observed for the laser array based on the 5QD-layer epitaxy, reaching the minimum linewidth of 370 kHz.

Finally, to investigate the possibility of cavity optimization as a contributing factor to linewidth reduction, we have applied the laser model to a novel cavity design [50]. The applied approach to cavity optimization has already been experimentally tested on quantum well laser with impressive results, and unsurprisingly by combining the high-performance quantum dots with the cavity optimization the laser model has predicted the linewidths of even below 10 kHz. In general we have shown that the quantum dots can be considered as a viable active material for future optical communication networks, and that the laser diodes based on quantum dots do not necessarily require complex processing to achieve high performance in terms of the spectral purity of the output signal.

6.2 Outlook

Even though significant milestones were accomplished, regarding the implementation of the *QD-wave* laser model some improvements could still be made. In the case of quantum dot gain model Ch. 3, one could assume a more realistic geometry for the quantum dots but still the variation of the dot shape and size intrinsically present in their pro-

cessing has to be taken into account [22, 23]. The same could be said for the implementation of the material strain which is currently biaxial, as the strain together with geometry ultimately determines the eigenstates of the quantum dots. This way it might not have to be necessary to correct the results of the eigenstate problem, by relying on the available gain measurements. Concerning the linewidth enhancement factor, the model currently included does take into account injection dependence [34], but it would be more accurate to include it through change of the gain dispersion at higher energy transitions as a result of the Pauli-blocking effect. However, this would require the calculation of the gain dispersion at each current sweeping step if not also in time, which would inevitably increase the simulation time. Other gain related effects that are worth considering are many-body effects and the self-heating effects that can also have a profound effect on the gain characteristic of the quantum dots [14].

Regarding the realization of the traveling wave model Ch. 4, for the possible improvements we can refer to the commercial software PICwave [66]. For a more accurate simulation of lasers as well as the SOA components the inclusion of the variation of carrier density and therefore the material gain over the transversal plane can be a significant improvement. This especially holds for the simulation of a SOA amplifier where the gain suppression can vary significantly not only along the longitudinal axis but transversally as well. In that sense it would be interesting to investigate the integrated devices coupled to a SOA, in terms of the linewidth, noise spectra or other properties and compare them to measurements.

Appendix A

Kramers-Kronig Relation

As the interdependence of the material gain/loss and the refractive index is important for better understanding the problem of spectral linewidth, we discuss here the Kramers-Kronig relation in more detail [67]. In general, the Kramers-Kronig relations can be derived by calculating the integral of the form:

$$I = \mathcal{P} \int_{-\infty}^{\infty} \frac{f(x)}{x - a} dx, \tag{A.1}$$

which applies for the function $f(x)$, that is analytic in the upper complex half-plane and vanishes as $|\omega| \to \infty$. To obtain the Kramers-Kronig relations for the complex refractive index we can apply the Eq. (A.1), to the electric susceptibility, χ, of the active material:

$$I = \mathcal{P} \int_{-\infty}^{\infty} \frac{\chi(\omega')}{\omega' - \omega} d\omega', \tag{A.2}$$

where the electric susceptibility, χ, governs the polarization of the material:

$$\boldsymbol{P}(t) = \epsilon_0 \int_{-\infty}^{t} \chi(t - \tau) \boldsymbol{E}(\tau) d\tau, \tag{A.3}$$

and the causality of $\chi(\tau)$, imposes the Kramers-Kronig constraints

on $\chi(\omega)$. If we assume the Lorentz model for the susceptibility the integral, Eq. (A.2), can be shown to be equal to:

$$I = \mathcal{P}\int_{-\infty}^{\infty} \frac{\chi(\omega')}{\omega' - \omega} d\omega' = i\pi\chi(\omega). \tag{A.4}$$

Using the relations, $\chi = \chi' + i\chi''$ and $\epsilon = \epsilon_0(1+\chi)$, we can decompose the Eq. (A.4), and express it through real and imaginary components of the permittivity, ϵ' and ϵ'':

$$\begin{aligned} I &= \left[\mathcal{P}\int_{-\infty}^{\infty} \frac{\epsilon'(\omega') - \epsilon_0}{\omega' - \omega} d\omega'\right] + i\left[\mathcal{P}\int_{-\infty}^{\infty} \frac{\epsilon''(\omega')}{\omega' - \omega} d\omega'\right] \\ &= -\pi\epsilon''(\omega) + i\left[\pi(\epsilon'(\omega) - \epsilon_0)\right]. \end{aligned} \tag{A.5}$$

By separating the Eq. (A.5), into its real and imaginary components, we get the Kramers-Kronig relations for the permittivity:

$$\epsilon'(\omega) - \epsilon_0 = \frac{2}{\pi}\mathcal{P}\int_0^{\infty} \frac{\omega'\epsilon''(\omega')}{\omega'^2 - \omega^2} d\omega', \tag{A.6}$$

$$\epsilon''(\omega) = -\frac{2\omega}{\pi}\mathcal{P}\int_0^{\infty} \frac{\epsilon'(\omega) - \epsilon_0}{\omega'^2 - \omega^2} d\omega'. \tag{A.7}$$

The complex refractive index can be related to the complex permittivity of the material as:

$$\epsilon = \epsilon' + i\epsilon'' = (n' + in'')^2, \tag{A.8}$$

which allows us to write out the Kramers-Kronig relations for the refractive index as well:

$$n'(\omega) - 1 = \frac{2}{\pi}\mathcal{P}\int_0^{\infty} \frac{\omega' n''(\omega')}{\omega'^2 - \omega^2} d\omega', \tag{A.9}$$

$$n''(\omega) = -\frac{2\omega}{\pi}\mathcal{P}\int_0^{\infty} \frac{n'(\omega) - 1}{\omega'^2 - \omega^2} d\omega'. \tag{A.10}$$

The imaginary part of the refractive index, $n''(\omega)$, can be related to the gain/loss, $\alpha(\omega)$, of the material using the relation:

$$n''(\omega) = \frac{c\alpha(\omega)}{2\omega}, \tag{A.11}$$

which after substituting into Eq.(A.9), gives the Kramers-Kronig relation between the real part of the refractive index and the material gain/loss:

$$n'(\omega) - 1 = \frac{c}{\pi}\mathcal{P}\int_0^\infty \frac{\alpha(\omega')}{\omega'^2 - \omega^2} d\omega'. \tag{A.12}$$

Finally, if we want to relate the change of the refractive index to the corresponding change of the gain/loss, α, through varying carrier density for example, we can write:

$$\Delta n'(\omega) = \frac{c}{\pi}\mathcal{P}\int_0^\infty \frac{\Delta\alpha(\omega')}{\omega'^2 - \omega^2} d\omega'. \tag{A.13}$$

List of Publications

1. M. Bjelica, V. Sichkovskyi, A. Rippien, B. Witzigmann, J.P. Reithmaier, "Design of Widely Tunable Narrow Linewidth Quantum-Dot DFB Laser Array", Center for Interdisciplinary Nanostructure Science and Technology (CINSaT) - *Herbstkolloquium 2013*, Kassel, Germany, Oct. 2013 (Poster)

2. M. Bjelica, B. Witzigmann, "Simulation Aspects of Narrow-Linewidth Quantum Dot Lasers for High-Speed Optical Networks", Center for Interdisciplinary Nanostructure Science and Technology (CINSaT) - *Herbstkolloquium 2014*, Kassel, Germany, Oct. 2014 (Poster)

3. A. Becker, V. Sichkovskyi, A. Rippien, F. Schnabel, J.P. Reithmaier, M. Bjelica, B. Witzigmann, "InP-based tunable quantum dot distributed feedback lasers with 1.55 μm wavelength", Center for Interdisciplinary Nanostructure Science and Technology (CINSaT) - *Herbstkolloquium 2014*, Kassel, Germany, Oct. 2014 (Poster)

4. J.P. Reithmaier, V. Sichkovskyi, A. Becker, B. Bjelica, B. Witzigmann, D. Gready, G. Eisenstein, "InP based high-gain QD material for high-speed and narrow linewidth applications", *Conf. on Physics of Quantum Electronics (PQE)*, Snowbird, Utah, USA, Jan. 2015 (Invited talk)

5. A. Becker, M. Bjelica, V. Sichkovskyi, A. Rippien, F. Schnabel, P. Baum, B. Witzigmann, J.P. Reithmaier, "InP-based narrow-linewidth widely tunable QD-DFB lasers", *VDE-ITG meeting*, Leipzig, Germany, May 2015

6. A. Becker, V. Sichkovskyi, M. Bjelica, O. Eyal, P. Baum, A. Rippien, F. Schnabel, B. Witzigmann, G. Eisenstein, J.P. Reithmaier,

"InP-based narrow-linewidth tunable quantum dot distributed feedback laser for coherent optical communication", *Compoung semiconductor week (CSW)*, S. Barbara, USA, June 2015

7. M. Bjelica, B. Witzigmann, "Simulation and Analysis of 1.55 μm quantum dot lasers designed for ultra-narrow linewidth", *IEEE NUSOD Conference*, Taipei, Taiwan, Sept. 2015

8. M. Bjelica, B. Witzigmann, "Reduction of Spectral Linewidth in Edge-emitting Quantum Dot Lasers Using High-Coherence Cavity Design", Center for Interdisciplinary Nanostructure Science and Technology (CINSaT) - *Herbstkolloquium 2015*, Kassel, Germany, Oct. 2015 (Poster)

9. J.P. Reithmaier, S. Banyoudeh, A. Abdollahinia, A. Becker, V. Sichkovskyi, O. Eyal. G. Eisenstein, M. Bjelica, B. Witzigmann, G. Moille, S. Combrie, A. DeRossi, "InP-Based Nanostructured Semiconductors for Telecom Applications", *German - French - Korean Workshop*, Würzburg, Germany, Dec. 2015 (Invited talk)

10. J.P. Reithmaier, S. Banyoudeh, A. Abdollahinia, V. Sichkovskyi, A. Becker, A. Rippien, F. Schnabel, B. Bjelica, B. Witzigmann, O. Eyal, G. Eisenstein, "The impact of low-dimensional gain material on emission linewidth and modulation speed in semiconductor lasers", *Conf. on Physics of Quantum Electronics (PQE)*, Snowbird, Utah, USA, Jan. 2016 (Invited talk)

11. M. Bjelica, B. Witzigmann, "Optimization of 1.55 μm quantum dot edge-emitting lasers for narrow spectral linewidth", *Optical and Quantum Electronics (OQE)*, vol. 48, Feb. 2016

12. A. Becker, V. Sichkovskyi, M. Bjelica, O. Eyal, P. Baum, A. Rippien, F. Schnabel, B. Witzigmann, G. Eisenstein and J.P. Reithmaier, "Narrow-linewidth 1.5 μm quantum dot distributed feedback lasers", *Photonics West Conf., Proc. SPIE 9767*, San Francisco, CA, USA, Mar. 2016

Bibliography

[1] A. Einstein, "Strahlungs-emission und -absorption nach der quantentheorie," *Verhandlungen der Deutschen Physikalischen Gesellschaft*, 1916.

[2] J. Gordon, H. Zeiger and C. Townes, "The maser - new type of microwave amplifier, frequency standard, and spectrometer," *Physical Review 99*, 1955.

[3] H. Krömer, "A proposed class of heterojunction injection lasers," *Proc. IEEE*, 1963.

[4] M. Seimetz, "Laser linewidth limitations for optical systems with high-order modulation employing feed forward digital carrier phase estimation," *Proc. OFC 2008*, 2008.

[5] M. Kitamura, H. Yamazaki, T. Sasaki, N. Kida, H. Hasumi, and I. Mito, "250kHz Spectral Linewidth Operation of 1.5 μm Multiple Quantum Well DFB-LD's," *IEEE Photonics Tech. Lett.*, 1990.

[6] H. Ishii, K. Kasaya, and H. Oohashi, "Narrow Spectral Linewidth (160kHz) Operation in Widely Tunable Distributed Feedback Laser Array," *Electron. Lett.*, 2010.

[7] L.A. Coldren, S.W. Corzine and M.L. Mašanović, *Diode Lasers and Photonic Integrated Circuits*. Wiley, 2012.

[8] C.H. Henry, "Theory of the Linewidth of Semiconductor Lasers," *IEEE J. Quantum Electron.*, 1982.

[9] A. L. Schawlow and C. H. Townes, "Infrared and optical masers," *Phys. Rev.*, vol. 112, pp. 1940–1949, Dec 1958.

[10] F. A. Hopf, P. Meystre, M. O. Scully, and W. H. Louisell, "Classical theory of a free-electron laser," *Phys. Rev. Lett.*, vol. 37, pp. 1215–1218, Nov 1976.

[11] W. E. Lamb, "Theory of an optical maser," *Phys. Rev.*, vol. 134, pp. A1429–A1450, Jun 1964.

[12] H. Dreicer, "Kinetic theory of an electronphoton gas," *Physics of Fluids*, vol. 7, no. 5, pp. 735–753, 1964.

[13] J. M. J. Madey, "Stimulated emission of bremsstrahlung in a periodic magnetic field," *Journal of Applied Physics*, vol. 42, no. 5, pp. 1906–1913, 1971.

[14] J. Piprek, *Optoelectronic Devices - Advanced Simulation and Analysis*. Springer, 2004.

[15] S. L. Chuang, *Physics of Photonics Devices*. John Wiley & Sons, Inc., 2009.

[16] J. Kim and S.L. Chuang, "Theoretical and Experimental Study of Optical Gain, Refractive Index Change, and Linewidth Enhancement Factor of p-Doped Quantum-Dot Lasers," *IEEE J. Quantum Electron.*, 2006.

[17] J. Kim, M. Laemmlin, C. Meuer, D. Bimberg and G. Eisenstein, "Static Gain Saturation Model of Quantum-Dot Semiconductor Optical Amplifiers," *IEEE J. Quantum Electron.*, 2008.

[18] J. Bai, Q. Wang, and T. Wang, "Characterization of InGaN-based nanorod light emitting diodes with different indium compositions," *Journal of Applied Physics*, vol. 111, no. 11, 2012.

[19] J. Wallentin, N. Anttu, D. Asoli, M. Huffman, I. Åberg, M. H. Magnusson, G. Siefer, P. Fuss-Kailuweit, F. Dimroth, B. Witzigmann, *et al.*, "InP nanowire array solar cells achieving 13.8% efficiency by exceeding the ray optics limit," *Science*, vol. 339, no. 6123, pp. 1057–1060, 2013.

[20] D. Bimberg et al., "Quantum dot lasers: breakthrough in optoelectronics," *Thin Film Solids*, 2000.

[21] K. Takada et al., "10.3-Gb/s Operation Over a Wide Temperature Range in 1.3-μm Quantum-dot DFB Lasers With High Modal Gain," *Proc. OFC 2010*, 2010.

[22] O. Stier, M. Grundmann, and D. Bimberg, "Electronic and optical properties of strained quantum dots modeled by 8-band k·p theory," *Phys. Rev. B*, vol. 59, pp. 5688–5701, Feb 1999.

[23] M. Grundmann, O. Stier, and D. Bimberg, "InAs/GaAs pyramidal quantum dots: Strain distribution, optical phonons, and electronic structure," *Phys. Rev. B*, vol. 52, pp. 11969–11981, Oct 1995.

[24] S. Ghosh, B. Kochman, J. Singh, and P. Bhattacharya, "Conduction band offset in InAs/GaAs self-organized quantum dots measured by deep level transient spectroscopy," *Applied Physics Letters*, vol. 76, no. 18, pp. 2571–2573, 2000.

[25] R. Veprek, *Computational Modeling of Semiconductor Nanostructures for Optoelectronics*. PhD thesis, Swiss Federal Institute of Technology Zurich, 2009.

[26] G. E. Forsythe, M. A. Malcolm and C. B. Moler, *Computer Methods for Mathematical Computations*. Prentice-Hall, 1976.

[27] A. Maryński et al., "Electronic structure, morphology and emission polarization of enhanced symmetry InAs quantum-dot-like structures grown on InP substrates by molecular beam epitaxy," *J. Appl. Phys.*, 2013.

[28] V.I. Sichkovskyi et al., "High-gain wavelength-stabilized 1.55 μm InAs/InP(100) based lasers with reduced number of quantum dot active layers," *Appl. Phys. Lett.*, 2013.

[29] D.-Y. Cong et al., "Optimization of α-factor for quantum dot InAs/GaAs Fabry-Pérot lasers emitting at 1.3 μm," *Electron. Lett.*, 2007.

[30] J. J. Sakurai and J. J. Napolitano, *Modern Quantum Mechanics*. Pearson Education Limited, 2014.

[31] M. Gioannini and M. Rossetti, "Time-Domain Traveling Wave Model of Quantum Dot DFB Lasers," *IEEE J. Sel. Top. Quant. Electron.*, 2011.

[32] H. C. Schneider and W. W. Chow, "Annomalous carrier-induced dispersion in quantom-dot active media," *Phys. Rev.*, 2002.

[33] K. Kikuchi, "Origin of Residual Semiconductor-Laser Linewidth in High-Power Limit," *Electronics Letters*, 1988.

[34] S. Melnik, G. Huyet and A. V. Uskov, "The linewidth enhancement factor α of quantum dot semiconductor lasers," *Optics Express*, 2006.

[35] J.E. Carroll, J. Whiteaway and D. Plumb, *Distributed Feedback Semiconductor Lasers*. Redwood Books, 1998.

[36] L. Dagum and R. Menon, "OpenMP: an industry standard API for shared-memory programming," *IEEE computational science and engineering*, vol. 5, no. 1, pp. 46–55, 1998.

[37] B. Tromborg, H. Lassen, H. Olesen, and X. Pan, "Traveling Wave Method for Calculation of Linewidth, Frequency Tuning, and Stability of Semiconductor Lasers," *IEEE Photonics Tech. Lett.*, 1992.

[38] B. Tromborg, H. Lassen, and H. Olesen, "Traveling Wave Analysis of Semiconductor Lasers: Modulation Responses, Mode Stability and Quantum Mechanical Treatment of Noise Spectra," *IEEE J. Quantum Electron.*, 1994.

[39] D. E. Aspnes and A. A. Studna, "Dielectric functions and optical parameters of Si, Ge, GaP, GaAs, GaSb, InP, InAs, and InSb from 1.5 to 6.0 eV," *Phys. Rev. B*, vol. 27, pp. 985–1009, Jan 1983.

[40] S. Adachi, "GaAs, AlAs, and AlxGa1xAs: Material parameters for use in research and device applications," *Journal of Applied Physics*, vol. 58, no. 3, pp. R1–R29, 1985.

[41] H.W. Dinges,H. Burkhard,R. Lsch,H. Nickel and W. Schlapp, "Refractive indices of InAlAs and InGaAs/InP from 250 to 1900 nm determined by spectroscopic ellipsometry," *Applied Surface Science*, 1992.

[42] M. Bass, C. DeCusatis, J. Enoch, V. Lakshminarayanan, G. Li, C. MacDonald, V. Mahajan, and E. Van Stryland, *Handbook of Optics, Volume IV: Optical Properties of Materials*, vol. 4. 2009.

[43] M. Dumitrescu, J. Telkkl, J. Karinen, J. Viheril, A. Laakso, S. Afzal, J.-P. Reithmaier, M. Kamp, P. Melanen, P. Uusimaa, P. Bardella, M. Vallone, I. Montrosset, O. Parillaud, M. Krakowski, D. Gready, G. Eisenstein, and G. Sek, "Development of high-speed directly modulated dfb and dbr lasers with surface gratings," *Proc. SPIE*, vol. 7953, pp. 79530D–79530D–12, 2011.

[44] George A.P. Thé, "How to simulate a semiconductor quantum dot laser: general description," *Revista Brasileira de Ensino de Física*, 2009.

[45] M. Rossetti, P. Bardella, and I. Montrosset, "Time-domain travelling-wave model for quantum dot passively mode-locked lasers," *IEEE Journal of Quantum Electronics*, vol. 47, no. 2, pp. 139–150, 2011.

[46] P. Vankwikelberge, G. Morthier, and R. Baets, "CLADISS - A Longitudinal Multimode Model for the Analysis of the Static, Dynamic, and Stochastic Behavior of Diode Lasers with Distributed Feedback," *IEEE J. Quantum Electron.*, 1990.

[47] J. Javaloyes and S. Balle, "Freetwm: a simulation tool for multisection semiconductor lasers," *[Online]*, 2012.

[48] G. E. P. Box and M. E. Muller, "A note on the generation of random normal deviates," *Ann. Math. Statist.*, vol. 29, pp. 610–611, 06 1958.

[49] S. Spießberger, *Compact Semiconductor-Based Laser Sources with Narrow Linewidth and High Output Power*. PhD thesis, Technische Universität Berlin, 2012.

[50] C. T. Santis, S. T. Steger, Y. Vilenchik, A. Vasilyev, and A. Yariv, "High-coherence semiconductor lasers based on integral high-Q resonators in hybrid Si/III-V platforms," *Proceedings of the National Academy of Sciences*, vol. 111, no. 8, pp. 2879–2884, 2014.

[51] H. Olesen, B. Tromborg, H. Lassen, and X. Pan, "Mode Instability and Linewidth Rebroadening in DFB Lasers," *Electronics Letters*, 1992.

[52] N. Kasdin, "Discrete Simulation of Colored Noise and Stochastic Processes and 1/f Power Law Noise Generation," *Proceedings of the IEEE*, 1995.

[53] J. C. Shrestha, S. Blom, B. Witzigmann, and H. H. Hillmer, "Investigation of relative intensity noise in asymmetric external cavity semiconductor laser sensors: Influence of dual-line spectral separation and linewidth enhancement factor," *IEEE Sensors Journal*, vol. 15, pp. 6619–6624, Nov 2015.

[54] B. Dawes, D. Abrahams, R. Rivera, *et al.*, "Boost C++ libraries," 2009.

[55] Intel MKL, "Intel math kernel library," 2007.

[56] A. Becker, V. Sichkovskyi, M. Bjelica, O. Eyal, P. Baum, A. Rippien, F. Schnabel, B. Witzigmann, G. Eisenstein, and J. P. Reithmaier, "Narrow-linewidth 1.5 μm quantum dot distributed feedback lasers," *Proc. SPIE*, vol. 9767, pp. 97670Q–97670Q–8, 2016.

[57] D. Gready and G. Eisenstein, "Carrier dynamics and modulation capabilities of 1.55-μm quantum-dot lasers," *IEEE Journal of Selected Topics in Quantum Electronics*, vol. 19, no. 4, pp. 1900307–1900307, 2013.

[58] D. Bimberg, N. Kirstaedter, N. N. Ledentsov, Z. I. Alferov, P. S. Kop'ev, and V. M. Ustinov, "InGaAs-GaAs quantum-dot lasers," *IEEE Journal of Selected Topics in Quantum Electronics*, vol. 3, pp. 196–205, Apr 1997.

[59] G. Morthier and B. Moeyersoon, "Intensity noise and linewidth of laser diodes with integrated semiconductor optical amplifier,"

Photonics Technology Letters, IEEE, vol. 14, no. 12, pp. 1644–1646, 2002.

[60] A. Champagne, J. Camel, R. Maciejko, K. Kasunic, D. Adams, and B. Tromborg, "Linewidth broadening in a distributed feedback laser integrated with a semiconductor optical amplifier," *Quantum Electronics, IEEE Journal of*, vol. 38, no. 11, pp. 1493–1502, 2002.

[61] H. Ishii, K. Kasaya, H. Oohashi, Y. Shibata, H. Yasaka, and K. Okamoto, "Widely wavelength-tunable dfb laser array integrated with funnel combiner," *IEEE Journal of Selected Topics in Quantum Electronics*, vol. 13, pp. 1089–1094, Sept 2007.

[62] D. F. G. Gallagher and T. P. Felici, "Eigenmode expansion methods for simulation of optical propagation in photonics: pros and cons," vol. 4987, pp. 69–82, 2003.

[63] L. B. Soldano and E. C. M. Pennings, "Optical multi-mode interference devices based on self-imaging: principles and applications," *Journal of Lightwave Technology*, vol. 13, pp. 615–627, Apr 1995.

[64] M. Bjelica and B. Witzigmann, "Optimization of 1.55 μm quantum dot edge-emitting lasers for narrow spectral linewidth," *Optical and Quantum Electronics*, vol. 48, no. 2, pp. 1–7, 2016.

[65] N. Satyan, G. Rakuljic, Y. Vilenchik, and A. Yariv, "A hybrid silicon/III-V semiconductor laser with sub-kHz quantum linewidth," in *2015 IEEE Summer Topicals Meeting Series (SUM)*, pp. 154–155, July 2015.

[66] D. F. Gallagher, "Designing active photonic integrated circuits using TDTW," in *Integrated Photonics and Nanophotonics Research and Applications*, p. ITuE2, Optical Society of America, 2008.

[67] H. Fujiwara, *Spectroscopic Ellipsometry*. John Wiley & Sons, Ltd, 2007.

The quantization of the active laser medium has enabled numerous advances in fiber-optic communications, e.g., higher efficiency of laser diodes, higher modulation bandwidth, lower spectral linewidth of the emitted signal. In recent years the quantum dot lasers have demonstrated a strong potential to continue this trend, therefore, by progressing from standard quantum well to quantum dot designs, it can be expected that the quantum dot lasers will play an increasingly important role in future fiber-optic communications.

The research work presented in this dissertation seeks to further develop the quantum dot laser designs and improve the understanding of complex operating conditions affecting the laser linewidth. This is achieved by developing a comprehensive laser simulator, that was applied to design and simulation of edge-emitting lasers and laser arrays. As a result, the optimized laser diodes have demonstrated a significantly lower linewidth compared to equivalent quantum well designs. Due to their narrow linewidth, the realized photonic devices can be a viable solution for high bit rate fiber-optic networks.

ISBN 978-3-7376-0284-6